

University of Nebraska - Lincoln

DigitalCommons@University of Nebraska - Lincoln

Theses, Dissertations, and Student Research:
Department of Physics and Astronomy

Physics and Astronomy, Department of

August 2006

STUDY OF MAGNETIC LAYERS IN MAGNETIC SENSORS

Lu Yuan

Physics Department, University of Nebraska, lyuan2@bigred.unl.edu

Follow this and additional works at: <https://digitalcommons.unl.edu/physicsdiss>



Part of the [Physics Commons](#)

Yuan, Lu, "STUDY OF MAGNETIC LAYERS IN MAGNETIC SENSORS" (2006). *Theses, Dissertations, and Student Research: Department of Physics and Astronomy*. 1.
<https://digitalcommons.unl.edu/physicsdiss/1>

This Article is brought to you for free and open access by the Physics and Astronomy, Department of at DigitalCommons@University of Nebraska - Lincoln. It has been accepted for inclusion in Theses, Dissertations, and Student Research: Department of Physics and Astronomy by an authorized administrator of DigitalCommons@University of Nebraska - Lincoln.

STUDY OF MAGNETIC LAYERS IN MAGNETIC SENSORS

By

Lu Yuan

A DISSERTATION

Presented to the Faculty of

The Graduate College at the University of Nebraska

In Partial Fulfillment of Requirements

For the Degree of Doctor of Philosophy

Major: Physics and Astronomy

Under the Supervision of Professor Sy-Hwang Liou

Lincoln, Nebraska

August, 2006

Study of Magnetic Layers in Magnetic Sensors

Lu Yuan, Ph. D.

University of Nebraska, 2006

Advisor: Sy-Hwang Liou

Interest in highly sensitive magnetic sensors has been great due to their wide applications ranging from data storage to geomagnetic exploration. To achieve better performance, magnetic sensors are usually fabricated with micrometer-sized or sub-micrometer-sized multilayer structures. The thickness of each layer can be as thin as a few angstroms. The magnetic properties of these small and thin layers are quite different from those of the bulk. As the size of the magnetic devices shrinks and the thickness of the ferromagnetic films decreases, the chance of having defects becomes higher. Those defects may be formed during thin film deposition, annealing and the lithography process *etc.* To have a better understanding the origin of those nanometer sized defects is important for improving sensitivity and signal-to-noise ratio of those magnetic sensors.

In this thesis, a magnetic sensitivity mapping (MSM) system is developed to locate the inhomogeneous regions in the ferromagnetic layer of magnetic sensors. An ultra-sensitive microcantilever torque magnetometer (MTM) system is developed to characterize the submicrometer-sized magnetic films and arrays. The detailed magnetic microstructures of both the free layer and the pinned layer in magnetic tunneling junctions are studied by the analysis of the temperature and voltage dependence of the tunneling magnetoresistance data.

We have correlated the microstructures to the sources of magnetic noise using the developed MSM system. In this study, a scanning nanometer-sized magnetic tip was used to generate a localized magnetic field and excite the free-layer magnetic moment at the air-bearing surface (ABS). By mapping out the magnetic noise as a function of position, the inhomogeneous regions in the ferromagnetic layer of the magnetic sensors that relate to magnetic instabilities inside the recording heads are identified.

We studied the voltage and temperature dependence of resistance and magnetoresistance of two types of magnetic tunneling junctions (MTJs). These two types of MTJ samples have different free layer structures but the same pinned structures and the same material for free and reference layers. The tunneling magnetoresistance ratio (TMR), defined as $(R_{AP}-R_P)/R_P$, is 26% and 70% for type 1 and type 2, respectively. From the analysis of our results, we conclude that: (1) There are more magnetic inhomogeneous regions in the free magnetic layer of type 1 MTJ samples than in those of type 2 MTJ samples; (2) There are possible additional spin-glass-like states that occur at the interface between the magnetic layer and the insulating layer in the type 1 MTJ sample at low temperature. These results clearly indicate that the micro-magnetization orientation in the free layer and its interfaces plays an important role in determining the TMR ratio in these two types of MTJ samples.

An ultra-sensitive MTM system is developed to characterize the magnetic nanostructures. The MTM system can be operated in temperature from 10 K to 300 K and under vacuum of 5×10^{-8} torr. We have also developed a new method to deposit magnetic patterns on cantilevers that allows us to have more flexibility in magnetic studies using MTM in the future.

ACKNOWLEDGEMENTS

I would like to express my appreciation to my advisor Professor Sy Hwang Liou for his invaluable guidance, advice and perspectives.

I thank Professor Roger D. Kirby, Professor Evgeny Tsymbal, Professor David Sellmyer, and Professor Yungfeng Lu for serving on my Supervisory Committee. I am grateful to them for their support of my research, and careful and critical reading of my thesis.

I would like to thank Professor Renat Sabirianov for many insightful discussions and help with understanding the theoretical implications of my work.

I am indebted to work with Professor Benard Doudin, Professor Peter Dowben, Professor Shireen Adenwalla, Professor Herman Batelaan, Professor Minglang Yan, Professor Andrei Sokolov, Professor Ralph Skomski, Professor Yingfan Xu, and Dr. Lanping Yue, who have provided me with assistance and helpful discussions.

I would wish to thank my friends in Professor Liou's group, Dr. Yakeshi Yokota, Dr. Kijoon H. P. Kim, Mr. Rui Zhang, and Mr. Yushun Lin. It is a pleasure to work with them. I appreciate the continuous and kind help from Dr. Lan Gao. Additional thanks goes to Ms. LeighAnn Nicholl for the proofreading this thesis and many of my publications.

Special thanks to all my collaborators from other institutions, Dr. John M. Moreland and Dr. Dong Hoon Min from NIST boulder laboratory, for patient instruction and help on my research; Dr. Dexin Wang, Dr. Jian Shen and Dr. Bharat B. Pant from Seagate

Technology in Bloomington, for helpful discussion on magnetic sensors and recording heads.

I also thank all the friends in the Department of Physics, Dr. Ruihua Cheng, Dr. Jian Zhou, Ms. Danqin Feng, Ms. Chun Juan Zhang, Mr. Zhiguang Sun, Dr. Jun Zhang, Professor Wei Liu, Dr. Zhongyuan Liu, and Dr. Mengjun Bai for various assistance.

Prompt assistance from the staff in the Department of Physics is greatly appreciated. I would thank Patty Christen, Theresa Sis, and Kay Haley for support and management; Dr. John Bob Kely for help in instrumentation; Michael J. Jensen, Robert L. Rhynalds, Troy O. Miller, Patrick J. Pribil, and Les Marquart, for help with the fabrication of instruments; and all the faculty, staff and friends of the Physics Department and the Nebraska Center for Materials and Nanoscience.

I would like to thank my family for their love and unwavering support. My parents, Rongxian Yang, Fengjiang Yuan always encouraged and supported me in pursue of my PhD degree. I especially thank them for helping me take care of my little baby while me preparation of this dissertation. Also I would like to thank my husband Zhijie Yang for providing help, inspiration and love. Finally I would like thank my little daughter Juliana. Her smile can always cheer me up. This work is dedicated to them.

Research was supported by the National Science Foundation (NSF) under MRSEC Awards Grant No. DMR-0213808, Army Research Office (ARO) Grant No. DAAD 19-03-1-0298, and Nebraska Research Initiative (NRI) at the University of Nebraska.

Contents

Chapter 1. Introduction	1
References.....	5
Chapter 2. Experiment.....	9
2.1. Magnetic sensitivity mapping (MSM)	9
2.1.1 MSM system setup.....	9
2.1.2 Magnetic tip.....	11
2.1.3 Methodology.....	12
2.2. Microcantilever torque magnetometry (MTM)	14
2.2.1 MTM system setup	14
2.2.2 Optic interferometer.....	18
2.2.3 Microcantilever	23
References.....	26
Chapter 3. Locating magnetic noise sources in magnetic sensors.....	28
3.1 Giant magnetoresistance (GMR) junction.....	28
3.2 Magnetic tunneling junction (MTJ)	30
3.3 Magnetic noise	32
3.4 MSM mapping	35
3.4.1 MSM mapping GMR sensor.....	35
3.4.2 MSM mapping for MTJ sensor.....	36
3.5 Summary.....	41
References.....	42

Chapter 4. Magnetic microstructures of free and pinned layer magnetic tunneling	
junctions-----	46
4.1 Effect of magnetic state in free layer-----	48
4.1.1 Temperature dependence of magnetoresistance-----	48
4.1.2. Voltage dependence of conductance-----	51
4.1.3 Temperature dependence of resistance-----	54
4.1.4 Temperature dependence of bias voltage dependence of magnetoresistance -----	59
4.1.5 Discussion -----	60
4.2 Effect of magnetic state in pinned layer-----	65
4.2.1 Major loop change with reversal field -----	65
4.2.2 Minor loop change with reversal field -----	68
4.2.3 Discussion-----	72
4.3 Summary-----	73
References -----	75
Chapter 5 Variable temperature and ultra-high vacuum microcantilever torque	
magnetometry (MTM) for studying magnetic nanostructures-----	78
5.1 Microcantilever torque magnetometry (MTM) -----	78
5.2 Fabrication of the magnetic patterned films on cantilevers-----	82
5.3 Single and paired bar measured at ambient conditions-----	86
5.4 The magnetization reversal behavior of two bars with magnetostatic interactions-----	92
5.5 The magnetization reversal behavior of two bars at various temperatures-----	94

5.6 Summary-----	96
References-----	97
Chapter 6 Conclusions and the future-----	100
Publication list-----	103

List of Figures

- Fig. 1.1 Layer structure of one magnetoresistance tunneling junction (MTJ)
- Fig. 2.1 Schematic diagram of the dynamic magnetic sensitivity mapping (MSM) system
- Fig. 2.2 Picture of the MSM system.
- Fig. 2.3 (a) SEM image of the magnetic force microscopy (MFM) cantilever; (b) SEM picture of the very end of the tip coated with CoPt particles; and (c) the hologram of the same tip [1].
- Fig. 2.4 Schematic drawing of the principle of the dynamic magnetic sensitivity mapping (MSM) system. The ABS plane is defined as the x - y plane. The magnetic moment of the free layer is defined as positive x direction. The magnetic moment of the reference layer is perpendicular to the free layer magnetic moment direction and aligned in the positive z direction. During measurement, the cantilever oscillates at its resonance frequency. The spacer layer is nonmagnetic material for GMR and is insulating material for MTJ.
- Fig. 2.5: Trace A: the noise spectra data of a GMR head when the tip scans over the stable part of the head or far away from the head; Trace B: the noise spectra data when the tip scans over the unstable part of the same GMR recording head.
- Fig. 2.6 Schematic diagram of the variable temperature and vacuum microcantilever torque magnetometer (MTM).
- Fig. 2.7 Pictures of (a) the variable temperature and vacuum MTM system, (b) sample probe and (c) enlarged sample holder.
- Fig. 2.8 Calibration of torque field versus coil current.

Fig. 2.9 Schematic diagram of the interferometer.

Fig. 2.10 Typical responsivity of the model 2034 photodiode

Fig. 2.11 the dc output with changing laser wavelength at a fixed fiber-to-cantilever distance at (a) high sensitivity range and (b) medium sensitivity range of the photoreceiver.

Fig. 2.12 The voltage of the photodetector output and ac voltage from lock-in amplifier as a function of wavelength of the laser source

Fig. 2.13 Schematic diagram of the fabrication process of cantilevers.

Fig. 2.14 (a) Photograph of the wafer and (b) (c) (d) cantilevers with different dimensions and shapes.

Fig. 3.1 (a) Layer structure of a GMR sensor and (b) Magnetoresistance for one GMR with layer structure as Si/NiFe/Cu/NiFe/FeMn/Ag as a function of H in the film plane at room temperature. The field is applied parallel to the exchange anisotropy field created by FeMn (EA). The current is perpendicular to this direction [5].

Fig. 3.2 (a) Layer structure of a MTJ sensor and (b) Magnetoresistance for one MTJ with layer structure of CoFe/Al₂O₃/Co plotted as a function of H in the film plane at 295 K [7].

Fig. 3.3 MSM images (a) under a positive and (b) under a negative magnetic field for a magnetically unstable GMR read head.

Fig. 3.4 (a) Time domain measurement of the noise amplitude under an external magnetic field for a stable MTJ head (Head 1) and an unstable MTJ head (Head 2); (b) MR loop for MTJ head 1 and (c) MR loop for MTJ head 2.

Fig. 3.5 MSM images for the MTJ head 1 (stable) (a) under a positive magnetic field and (b) under a negative field; and for magnetic MTJ head 2 (unstable) (c) under a positive magnetic field and (d) under a negative field.

Fig. 4.1 The layer structures of (a) type 1 and (b) type 2 MTJ samples

Fig. 4.2 Magnetoresistance transverse loops for (a) type 1 and (b) type 2 MTJs.

Fig. 4.3 The squareness (S) and hysteresis field (H_c) of type 1 and type 2 MTJs.

Fig. 4.4 Conductance versus bias voltage at 13 K for type 1 in the (a) P state and (b) AP state and for type 2 in the (c) P state and (d) AP state.

Fig. 4.5 Temperature dependence of the resistance-area product (RAP) in the P and AP states for (a) type 1 and (b) type 2 MTJs.

Fig. 4.6 Temperature dependence of TMR for (a) type 1 and (b) type 2 MTJs.

Fig. 4.7 Voltage dependence of TMR at different temperatures for (a) type 1 and (b) type 2 samples and voltage dependence of V_{out} (defined as $V \cdot TMR$) for (c) type 1 and (d) type 2 samples. The direction of bias voltage is defined with respect to upper electrode.

Fig. 4.8 The magnetoresistance (MR) loops for (a) type 1 and (b) type 2 MTJ samples.

The insets of Fig. 4.8 (a) show the layer structures and magnetization of each layer of the MTJ at various fields.

Fig. 4.9 Minor magnetoresistance loops for (a) type 1 and (b) type 2 MTJs for different applied reversal fields.

Fig. 4.10 R_{AP} and R_P of the minor loops for (a) type 1 and (b) type 2 MTJs for different applied reversal fields.

Fig. 4.11 TMR of the minor loops for (a) type 1 and (b) type 2 MTJs for different

applied reversal fields.

Fig. 4.12 H_E of the minor loops for (a) type 1 and (b) type 2 MTJs for different applied reversal fields.

Fig. 4.13 H_c of the minor loops for (a) type 1 and (b) type 2 MTJs for different applied reversal fields.

Fig. 5.1 The resonance frequency measurement of the same cantilever under (a) ambient conditions, (b) 136 K and 1×10^{-6} torr and (c) 300K and 5×10^{-7} torr.

Fig. 5.2 Schematic diagram of the fabrication process of sample on the microcantilever.

Fig.5.3 SEM image of the cantilever (a) with 100 50nm-thick $Ni_{80}Fe_{20}$ dots array; (b) enlarged patterned dots with a diameter of 500 nm and center-to-center distance of 2 μm ; and (c) enlarged patterned dots with a diameter of 1 μm and the center-to-center distance is 4 μm .

Fig. 5.4 The hysteresis loops for 100 50nm-thick $Ni_{80}Fe_{20}$ dots array with (a) with a diameter of 1 μm and the center-to-center distance is 4 μm ; and (b) a diameter of 500 nm and center-to-center distance of 2 μm .

Fig. 5.5 (a) Microcantilever with a $7 \mu m \times 7 \mu m \times 30$ nm $Ni_{80}Fe_{20}$ film deposited on the top left corner. (b) Magnified $7 \mu m \times 7 \mu m \times 30$ nm $Ni_{80}Fe_{20}$ film. (c) Double $7 \mu m \times 3.5 \mu m \times 30$ nm bars patterned with focused ion beam on the $7 \mu m \times 7 \mu m \times 30$ nm $Ni_{80}Fe_{20}$ film with gap of 50 nm between adjacent bars. (d) A single $7 \mu m \times 3.5 \mu m \times 30$ nm bar after removing the top bar with focused ion beam.

Fig. 5.6 Magnetic hysteresis loops of the single $7 \mu m \times 3.5 \mu m \times 30$ nm $Ni_{80}Fe_{20}$ bar (solid squares) and same size double bars (open dots) with a gap of 60 nm obtained with a microcantilever torque magnetometer (MTM).

Fig. 5.7 Micromagnetic simulations were performed on the paired $\text{Ni}_{80}\text{Fe}_{20}$ bars ($7\ \mu\text{m} \times 3.5\ \mu\text{m} \times 30\ \text{nm}$) with a gap of 50 nm. The sample was saturated along the long axis of the bars and then decreases to (a) $-4.77\ \text{kA/m}$; (b) $-20.69\ \text{kA/m}$; (c) $-26.26\ \text{kA/m}$; (d) $-31.83\ \text{kA/m}$.

Fig. 5.8 Magnetic interaction in a single paired bars and its magnetic switching behavior shows a reduced thermal magnetic switching distribution when the first bar reverses its magnetization. (The six hysteresis curves are obtained by continuous measurement of the single paired bars using ultra-sensitive microcantilever torque magnetometer.) The inset shows the SEM picture of a microcantilever with single paired bars.

Fig. 5.9 The hysteresis loop of single paired bar with dimension of $30\ \mu\text{m} \times 10\ \mu\text{m} \times 30\ \text{nm}$ and the gap is 60 nm [inset of (a)] measured at (a) 300 K and 5×10^{-7} torr and (b) 136 K and 1×10^{-6} torr by MTM.

List of Tables

Table 4.1 The fitting barrier parameters of type 1 and type 2 MTJ samples.

Table 4.2. The fitting transport mechanisms and junction quality parameters.

Chapter 1

Introduction

Magnetic field sensors have had a significant impact over the past fifty years in many different technological areas. The most important areas include homeland security, health care, information technology, geomagnetic exploration, and nanotechnology. Magnetic field sensing technology has been driven by the need for improved sensitivity, small size, low power, low cost and compatibility with electronic systems. To achieve those requirements, magnetic sensors are usually fabricated with micrometer-sized or sub-micrometer sized multilayer structures. The thickness of each layer can be as thin as a few angstroms.

For example, the basic structure of a magnetic tunneling junction (MTJ) is a sandwiched structure consisting of two ferromagnetic layers (FM) separated by a thin insulating layer. One of the ferromagnetic layers is called the “pinned layer” and is magnetically oriented in a fixed direction. The other ferromagnetic layer is called the “free” layer in which the magnetization rotates in response to an external magnetic field. The resistance of the junction depends on the relative orientation of magnetizations in the two ferromagnetic layers. Also from Julliere model, the magnetoresistance (MR) ratio, defined as $(R_{AP}-R_P)/R_P$, is higher for the material with higher spin polarization [1]. The first reported MTJ with large MR ratio (13.4%) at room temperature has layer structures as CoFe (80 Å)/Al₂O₃(16~18 Å)/Co (100~300Å) [2]. In these studies, with field higher than the coercivity of the both FM films, the magnetization of the two FM films is saturated and aligned with the applied field. To be used as sensor or memory, only the

free layer of the MTJ responds to the field, and the pinned layer is required to keep the magnetization unchanged during operation. Then the coercivity of the pinned layer should be higher than that of free layer. And the sensing field has to be restricted to being lower than a maximum value so the pinned layer would not be disturbed. Also it is possible that small domains in the pinned layer can be reversed by repeated low field and can not return to their original states [3].

An improved pinning field is achieved by adding an adjacent antiferromagnetic (AFM) layer to the pinned layer through exchange coupling. A desirable candidate for the AFM layer should have high exchange coupling strength, high blocking temperature, good corrosion resistance, low cost, and avoid high temperature treatment to establish the AFM phase to destroy the TMR effect due to the intermixing at the interface. So far, various AFM materials, such as FeMn, NiO, IrMn, PdPtMn, TbCo, and CrPt *etc.*, have been exploited as pinning layers [4-10]. By using the synthetic antiferromagnet (SAF) structure in addition to the antiferromagnet layer, the fringing field to the free layer caused by the pinned layer can be reduced due to the flux closure of the two ferromagnetic layers in the SAF [11-14].

For the free layer, a small coercivity field is preferred to get higher sensitivity. Progressively thinner free layers continue to be required. However, the thickness on the order of the spin-up and spin-down conduction electron mean free paths (as an example, for $\text{Ni}_{80}\text{Fe}_{20}$ is about 50 Å and 6 Å at room temperature for spin-up and spin-down, respectively) causes a rapid reduction in magnetoresistance in giant magnetoresistance (GMR) sensors [15]. To obtain large magnetoresistance with high sensitivity of free layers, synthetic ferrimagnet (SF) free layers have been proposed by decreasing the

effective free layer thickness while maintaining the large physical free layer thickness [16-17].

Fig. 1.1 shows typical layer structures of a magnetic tunneling junction sensor, 80Ru-8CoFeB-15Al₂O₃-50CoFeB-9Ru-54FeCo-350CrMnPt (in Å). The antiferromagnetic (AFM) material CrMnPt is at the top. The blocking temperature of 250 Å CrMnPt films is 320 °C after 230 °C 2 hr thermal anneal [18]. The FeCo/Ru/CoFeB forms SAF structure [14]. The 8 Å CoFeB is the free layer.

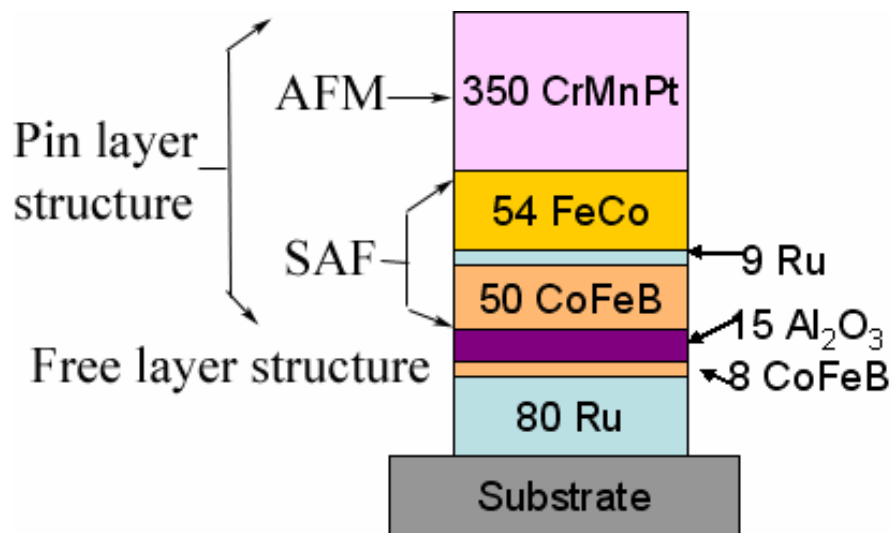


Fig. 1.1 Layer structure of one magnetoresistance tunneling junction (MTJ).

Magnetic sensors with smaller sized and thinner thickness of complicated layer structures are needed. With the recording bit aerial density proposed as high as 1 Tbit/inch², the width of each bit will be as small as 25 nm. Then the recording head with dimension on the same order is required. Also smaller magnetic elements are demanded for the higher density of information storage, such as magnetic random access memory (MRAM). With the size of the magnetic devices shrinking and the thickness of the ferromagnetic films decreasing, the chance of having defects becomes higher. These

defects may be formed during thin-film deposition, annealing and the lithography process *etc.* So the magnetic properties of these small and thin layers are quite different from that of the bulk. The sensor behavior depends strongly on the properties of these thin and small magnetic elements. To characterize and analysis nanometer sized defects is important for improving sensitivity and signal-to-noise ratio of such magnetic sensors.

Many investigations have been performed to study the magnetic properties of very thin films [19-22] and in submicron sized patterned magnetic films [23-26]. The characterization methods include x-ray diffraction, vibrating sample magnetometer (VSM), alternating gradient force magnetometer (AGM), magnetic force microscopy (MFM), atomic force microscopy (AFM), magneto-optical Kerr effect (MOKE), *etc.* However, conventional magnetometers are designed for measuring specimens in millimeter dimension. Therefore they have low signal-to-noise ratio (SNR) for small specimens. To measure small specimens, it is necessary to measure a large amount of small samples to get enough signals. Then the measurement result is the statistic average of all the samples.

In this thesis, a new magnetic sensitivity mapping (MSM) system is developed to locate the inhomogeneous regions in the ferromagnetic layer of magnetic sensors. An ultra-sensitive microcantilever torque magnetometer (MTM) system is developed to characterize the submicrometer-sized magnetic films and arrays. The detailed magnetic microstructures of free layer and pinned layer in magnetic tunneling junctions are studied by the analysis of the temperature and voltage dependence of the tunneling magnetoresistance data.

References:

1. M. Julliere, "Tunneling between ferromagnetic films", *Phys. Lett.*, **54A**, 225 (1975).
2. J. S. Moodera, Lisa R. Kinder, Terrilyn M. Wong, and R. Messervey, "Large magnetoresistance at room temperature in ferromagnetic thin film tunnel junctions", *Phys. Rev. Lett.*, **74**, 3273 (1995).
3. S. Gider, B. U. Runge, A. C. Marley, and S. S. P. Parkin, "The magnetic stability of spin-dependent tunneling devices", *Science*, **283**, 797 (1998).
4. T. Lin, C. Tsang, R. Fontana, and J. Howard, "Exchange-coupled Ni-Fe/Fe-Mn, Ni-Fe/Ni-Mn and NiO/Ni-Fe films for stabilization of magnetoresistive sensors", *IEEE Trans. Magn.*, **31**, 2585 (1995); S. Mao, S. Gangopadhyay, N. Amin, and E. Murdock, "NiMn-pinned spin valves with high pinning field made by ion beam sputtering", *Appl. Phys. Lett.*, **69**, 3593 (1996).
5. Z. Qian, J. M. Sivertsen, J. H. Judy, B. A. Everitt, S. Mao, and E. S. Murdock, "Exchange coupling of radio frequency sputtered NiMn/NiFe and NiFe/NiMn bilayers", *J. Appl. Phys.*, **85**, 6106 (1999).
6. M. Tondra and D. Wang, "High temperature pinning properties of IrMn versus FeMn in spin valves", *J. Vac. Sci. Technol.*, **17**, 2220 (1999); D. Wang, M. Tondra, J. M. Daughton, C. Nordman, and A. V. Pohm, "Spin dependent tunnel/spin-valve devices with different pinning structures made by photolithography", *J. Appl. Phys.*, **85**, 5255 (1999).

7. Y. Hamakawa, M. Komuro, K. Watanabe, H. Hishiyama, T. Okada, K. Nakamoto, Y. Suzuki, M. Fukuyama, and H. Fukui, "Spin-valve heads using CrMnPt antiferromagnetic films", *IEEE Trans. Magn.*, **35**, 677 (1999).
8. S. Mao and Z. Gao, "Improvement of giant magnetoresistance properties of CrMnPt spin valves by dc magnetron sputtering", *J. Appl. Phys.*, **87**, 6662 (2000); M. Saito, N. Hasegawa, K. Tanaka, Y. Ide, F. Koike, and T. Kuriyama, "PtMn spin valve with synthetic ferrimagnet free and pinned layers", *J. Appl. Phys.*, **87**, 6974 (2000).
9. B. Dai, J. W. Cai, W. Y. Lai, Y. Z. Liu, Z. Zhang, F. B. Meng, and Y. X. Li, "Large enhancement of exchange bias in CoFe/CrPt films through interfacial Mn addition", *J. Appl. Phys.*, **99**, 073902 (2006).
10. B. Dai, J. W. Cai, W. Y. Lai, Y. K. An, Z. H. Mai, F. Shen, Y. Z. Liu, and Z. Zhang, "Large exchange bias and high stability of CoFe/CrPt films with L1₀ CrPt as the pinning layer", *Appl. Phys. Lett.*, **87**, 092506 (2005).
11. J. G. Zhu and Y. Zheng, "Characteristics of AP bias in spin valve memory elements", *IEEE Trans. Magn.*, **34**, 1063 (1998).
12. H. Berg, W. Clemens, G. Gieres, G. Rupp, W. Schelter, and M. Vieth, *ibid.* **32**, 4624 (1996).
13. J. L. Leal and M. H. Kryder, "Spin valves exchange biased by Co/Ru/Co synthetic antiferromagnets", *J. Appl. Phys.*, **83**, 3720 (1998).
14. D. Wang, M. Tondra, J. M. Daughton, C. Nordman, and A. V. Pohm, "Spin dependent tunnel/spin-valve devices with different pinning structures made by photolithography", *J. Appl. Phys.*, **85**, 5255 (1999).

15. B. A. Gurney, V. S. Speriosu, J. P. Nozieres, H. Lefakis, D. R. Wilhoit, and O. U. Need, "Direct measurement of spin-dependent conduction-electron mean free paths in ferromagnetic metals", *Phys. Rev. Lett.*, **71**, 4023 (1993).
16. B. A. Gurney, H. Lefakis, O. U. Need, S. S. P. Parkin, V. S. Speriosu, and D. R. Wilhoit, US Patent No. 5,408,377, 18 April 1995.
17. Masamichi Saito, Naoya Hasegawa, Kenichi Tanaka, Yosuke Ide, Fumihito Koike, and Toshihiro Kuriyama, "PtMn spin valve with synthetic ferrimagnet free and pinned layers", *J. Appl. Phys.*, **87**, 6974 (2000).
18. Sining Mao and Zheng Gao, "Improvement of giant magnetoresistance properties of CrMnPt spin valves by dc magnetron sputtering", *J. Appl. Phys.*, **87**, 6662, (2000).
19. Y. Luo, M. Esseling, A. Käufler, K. Samwer, T. Dimopoulos, G. Gieres, M. Vieth, M. Rührig, J. Wecker, C. Rudolf, T. Niermann, and M. Seibt, "Co-rich magnetic amorphous films and their application in magnetoelectronics", *Phys. Rev. B.*, **72**, 014426 (2005).
20. R. Schad, H. Alouach, J. W. Harrell, M. Shamsuzzoha, D. Wang, "Superparamagnetic NiFeCo layers as free layers in magnetic tunnel junctions", *J. Appl. Phys.*, **93**, 8561 (2003).
21. C. -Y. Hund, M. Mao, S. Fundad, T. Schneider, L. Miloslavsky, M. Miller, C. Qian, and H. C. Tong, "Magnetic properties of ultrathin NiFe and CoFe films", *J. Appl. Phys.*, **87**, 6628 (2000).

22. D. Wang, J. M. Daughton, K. Bussmann, and G. A. Prinz, “Magnetic properties of very thin single and multilayer NiFeCo and CoFe films deposited by sputtering”, *J. Appl. Phys.*, **83**, 7034 (1998).
23. L. Gao, D. Q. Feng, L. Yuan, T. Yokota, R. Sabiriznov, S. H. Liou, M. D. Chabot, D. Porpora, and J. Moreland, “A study of magnetic interactions of Ni₈₀Fe₂₀ arrays using ultrasensitive microcantilever torque magnetometry”, *J. Appl. Phys.*, **95**, 7010 (2004).
24. J. I. Martín, J. Nogués, Kai Liu, J. L. Vicent, Ivan K. Schuller, “Ordered magnetic nanostructures: fabrication and properties”, *J. Magn. Mater.*, **256**, 449, (2003).
25. M. Rahm, M. Schneider, J. Biberger, R. Pulwey, J. Zweck, D. Weiss, and V. Umansky, “Vortex nucleation in submicrometer ferromagnetic disks”, *Appl. Phys. Lett.*, **82**, 4110 (2003).
26. Del Atkinson, Dan A. Allwood, Gang Xiong, Michael D. Cooke, Colm C. Faulkner and Russell P. Cowburn, “Magnetic domain-wall dynamics in a submicrometer ferromagnetic structure”, *Nature*, **2**, 85 (2003).

Chapter 2

Experiment

A magnetic sensitivity mapping (MSM) system is developed to characterize the magnetic inhomogeneity. Also an ultra-high sensitivity microcantilever torque magnetometry (MTM) is developed, which can be operated under variable temperature from 10 K to 300 K and under ultrahigh vacuum to 10^{-8} torr. In this chapter, the principle, techniques and instrumental setup are briefly described.

2. 1 Magnetic sensitivity mapping (MSM) system

2. 1. 1 MSM system setup

Fig. 2.1 is a schematic graph of the experimental setup of the MSM system. The experimental setup is based on a scanning magnetic force microscope (MFM). During the measurement, the head under test is fixed on a specially designed stage of the scanning magnetic force microscope. The stage includes a circuit that connects the electronics to the recording head. A low-noise current source is used to apply a constant dc bias current to the recording heads. The voltage output signal from the testing recording head was picked up and amplified by a low noise preamplifier with a gain of 1000. This amplified signal was connected to a spectrum analyzer to measure the noise in the frequency range of interest. The noise data is processed by a computer and then converted back to analog signal through a D/A converter. The final signal is fed back into the input channel of the MFM. This allows us to plot the noise changes with respect to the tip position to get the magnetic noise mapping for the tested recording head.

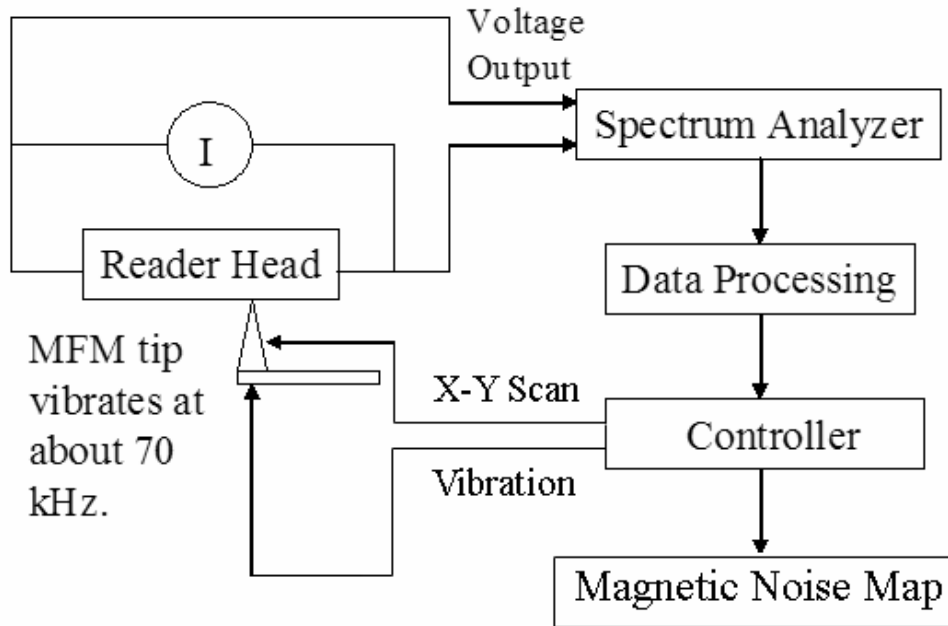


Fig. 2.1 Schematic diagram of the magnetic sensitivity mapping (MSM) system.



Fig. 2.2 Picture of the MSM system.

2. 1. 2 Magnetic tip

A magnetic tip (Fig. 2.3) is used to apply a localized magnetic field to the giant magnetoresistance (GMR) or MTJ head. The high-resolution SEM micrograph of a typical tip is shown in Fig. 2.3 (b), which shows the details of a tip coated with CoPt particles on the apex of the tip. The phase map reconstructed from the hologram of the same tip is shown in Fig. 2.3 (c) [1]. The alternatively black and white lines are the magnetic flux lines that emerge from the MFM tip. The magnetic stray field that originates from the CoPt particles on the tip can be estimated from the analysis of the hologram data. The magnetic field generated by this tip at the MR sensor surface is about 8 kA/m(100 Oe) [2].

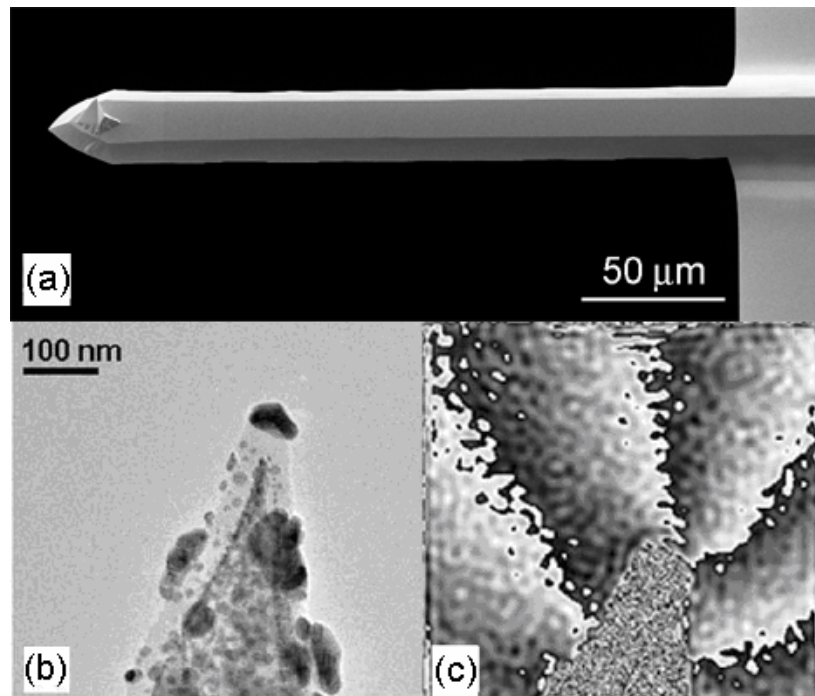


Fig. 2.3 (a) SEM image of the magnetic force microscopy (MFM) cantilever; (b) SEM picture of the very end of the tip coated with CoPt particles; and (c) the hologram of the same tip [1].

2.1.3 Methodology

The recording heads used in this investigation are standard PtMn-based bottom GMR recording heads and PtMn-based Al_2O_3 barrier MTJ recording heads provided by Seagate Technology. In either case, the magnetization direction of the reference layer is aligned perpendicular to the free layer for signal linearity (Fig. 2.4). The heads are stabilized by CoCrPt magnets on both sides of the sensor element [3]. The dc bias current is in the film plane (x axis) for GMR heads and perpendicular to the film plane (y axis) for MTJ heads. During the measurement, tapping mode with no lift height in the MFM software was selected. That means the tip end is very close to the air-bearing surface (ABS) of the MR heads. The cantilever oscillates at its resonance frequency (typically around 70 kHz).

Since most noise associated with magnetic instability is typically in the low frequency range, all the noise investigated in this chapter was chosen in the frequency range of 20 kHz – 60 kHz. When no tip was scanning over the MR heads, the noise spectrum is measured in the specified frequency range by a spectrum analyzer, as shown in (Fig. 2.5 trace “A”). That noise is the integration of the system noise plus all the noise sources of the head that are not related to the magnetic field excitation, such as electronic noise in the circuit, Johnson-Nyquist noise *etc.* We set this noise as the noise floor of the measured head. When the tip scans over the stable part of the GMR head, the noise spectrum has no obvious difference from the noise floor. However, when the magnetic tip is scanning over the unstable part of the head, noise increases (Fig. 2.5 trace “B”). The noise difference between the tip scanning over the heads and when the tip is away from the head is the noise due to the magnetic excitation.

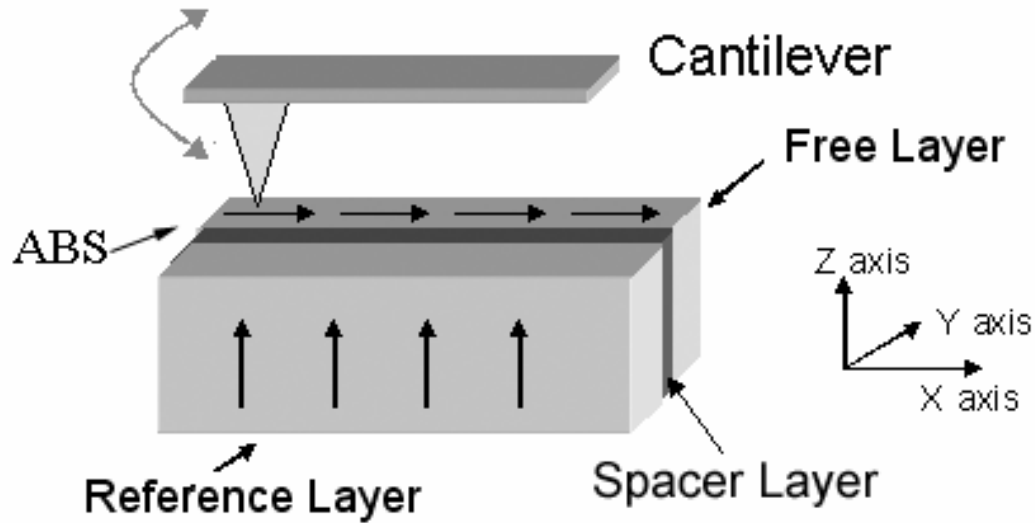


Fig. 2.4 Schematic drawing of the principle of the dynamic magnetic sensitivity mapping (MSM) system. The ABS plane is defined as the x–y plane. The direction of the magnetic moment of the free layer is defined as positive x direction. The magnetic moment of the reference layer is perpendicular to the free layer magnetic moment direction and aligned in the positive z direction. During measurement, the cantilever oscillates at its resonance frequency. The spacer layer is nonmagnetic material for GMR and insulating material for MTJ.

The cantilever's scanning rate should be selected to be slower than the spectrum analyzer's sweep rate. Unmatched scan rate with analyzer's sweep rate will cause image distortion. The spatial resolution of this noise mapping system is mainly determined by the magnetic tip dimension. The resolution of the MSM images can be comparable to the magnetic force microscope.

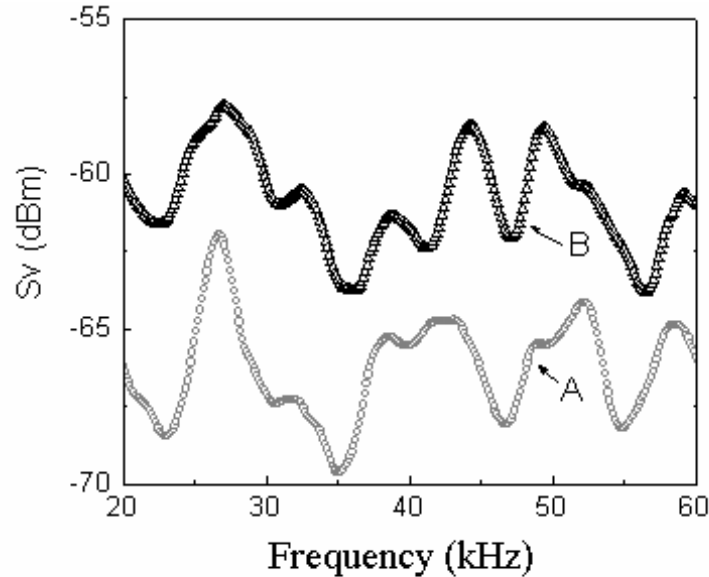


Fig. 2.5 Trace “A”: the noise spectra data of a GMR head when the tip scans over the stable part of the head or far away from the head; **Trace “B”:** the noise spectra data when the tip scans over the unstable part of the same GMR recording head.

2. 2 Microcantilever torque magnetometry (MTM)

2. 2. 1 MTM system setup

The schematic diagram of the microcantilever torque magnetometry (MTM) system is shown in Fig. 2.6. It mainly consists of one custom designed oscillator cantilever, a fiber optic interferometer, a lock-in amplifier, a solenoid coil, one function generator, temperature controller, and a magnet. The sample to be measured is put on the cantilever and the cantilever is placed between the two poles of the electromagnet. The magnetic sample is magnetized (\vec{M}) by an applied dc field in the sample plane. A small ac torque field is applied perpendicular to the sample plane (\vec{H}_t , torque field) by the solenoid coil.

(Fig. 2.8 shows the calibration between the dc current and the generated dc field.) Then a torque,

$$\tau = \vec{M} \times \vec{H}_t$$

is applied to the cantilever. If the torque field oscillates at the resonance frequency of the cantilever, the amplitude of the oscillating cantilever is at the maximum. Since the angle of oscillation is small, it is assumed that the oscillation amplitude is proportional to the torque amplitude. So with a known torque field, the magnetization of the sample is proportional to the magnetite of the oscillation.

The distance change is detected by an optical interferometer. The optical interferometer can transfer the amplitude change of the cantilever to an electrical voltage signal. And the output voltage from the optical interferometer is connected to the lock-in amplifier to measure the amplitude of the cantilever at the resonance frequency. By plotting the amplitude versus the applied magnetic field in the sample plane, the hysteresis loop can be obtained.

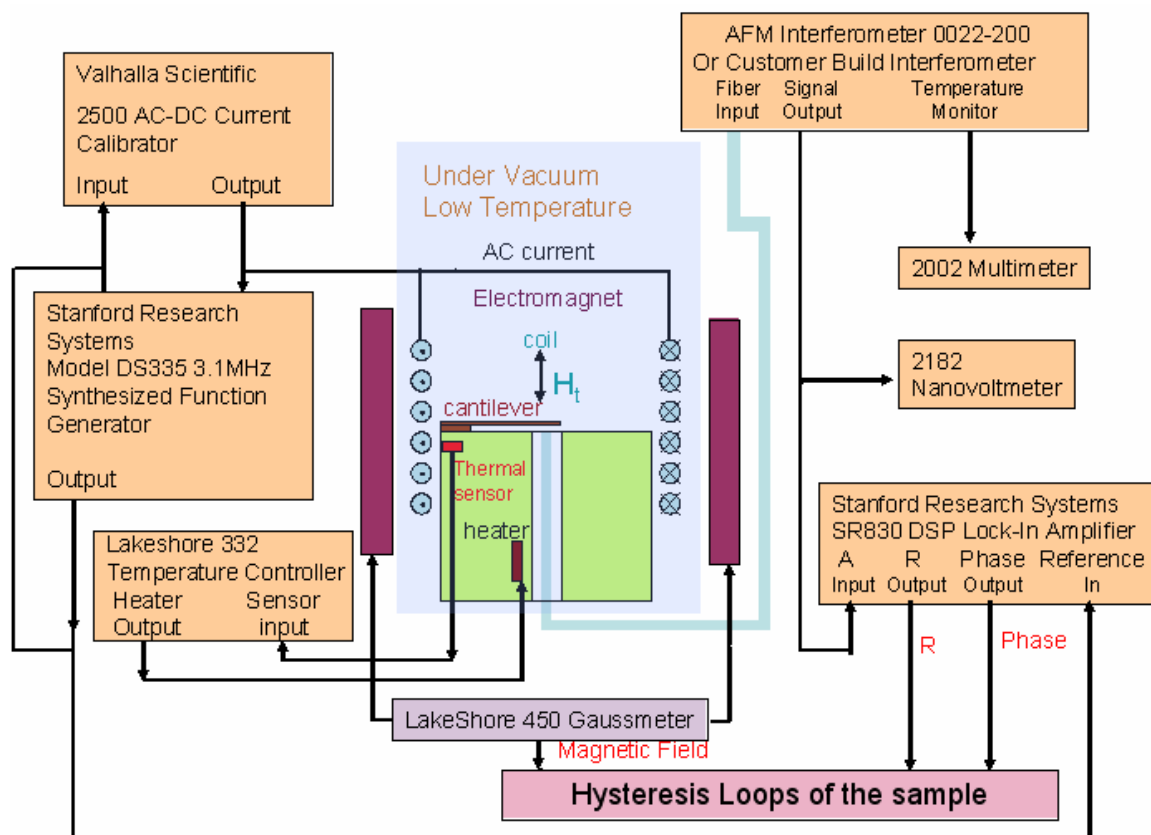


Fig. 2.6 Schematic diagram of the variable temperature and vacuum microcantilever torque magnetometer (MTM).

Fig. 2.7 shows a photo of the MTM system. The system allows MTM measurements from 10 K to 300 K under vacuum to 5×10^{-8} torr, and under a magnetic field ranging of ± 677 kA/m (± 8.5 kOe). By reading the temperature with a CY7-SD7 diode sensor, a Lakeshore332 temperature controller adjusts the power to the heater, which results in a temperature stability within ± 0.01 K in the range from 10 K to 400K. The magnetic field was measured by Lakeshore 450 gaussmeter. The gaussmeter can resolve $\pm 10^{-7}$ T (± 0.001 G) at the range of ± 0.03 T (± 300 Gauss).

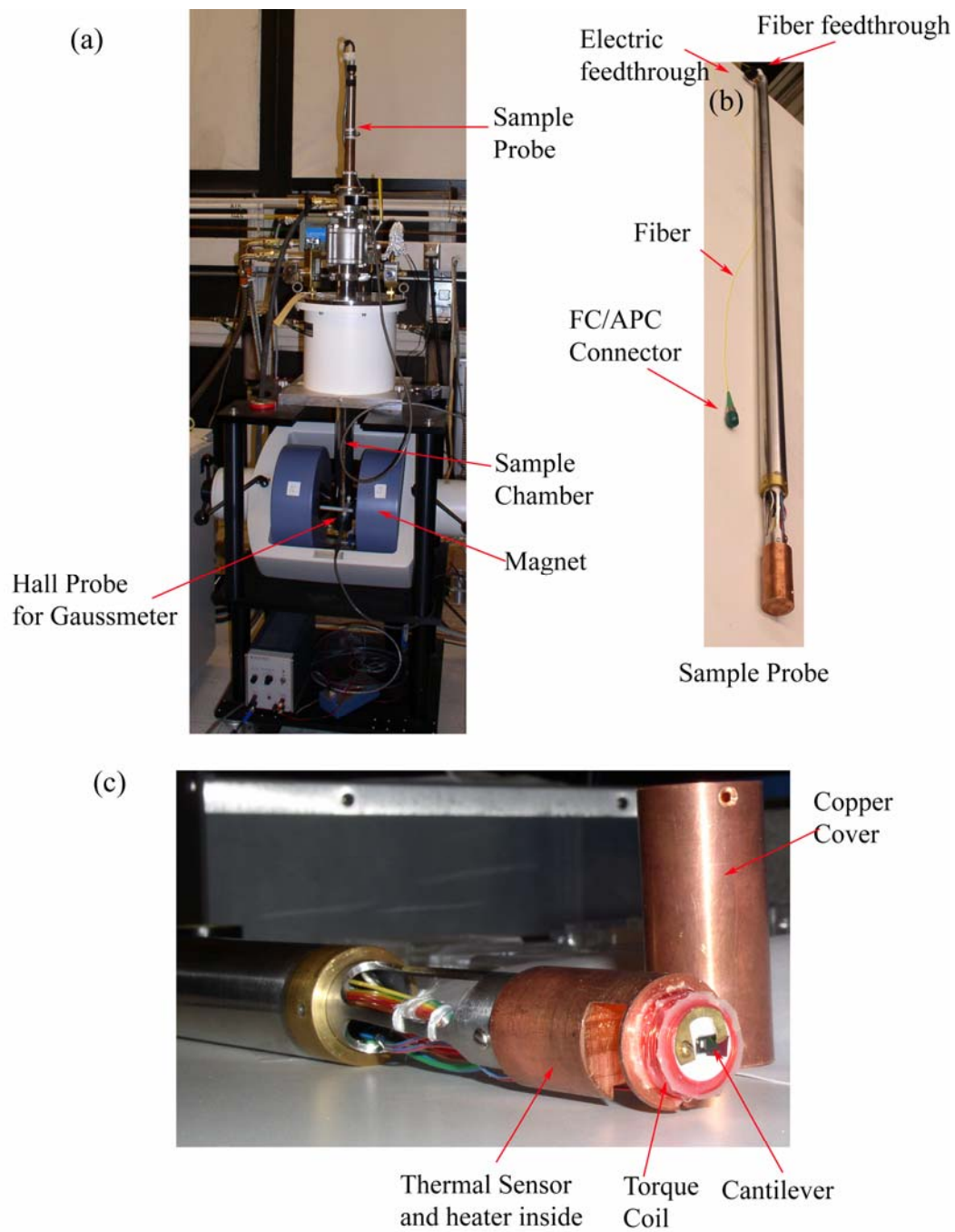


Fig. 2.7 Pictures of (a) the variable temperature and vacuum MTM system, (b) sample probe and (c) enlarged sample holder.

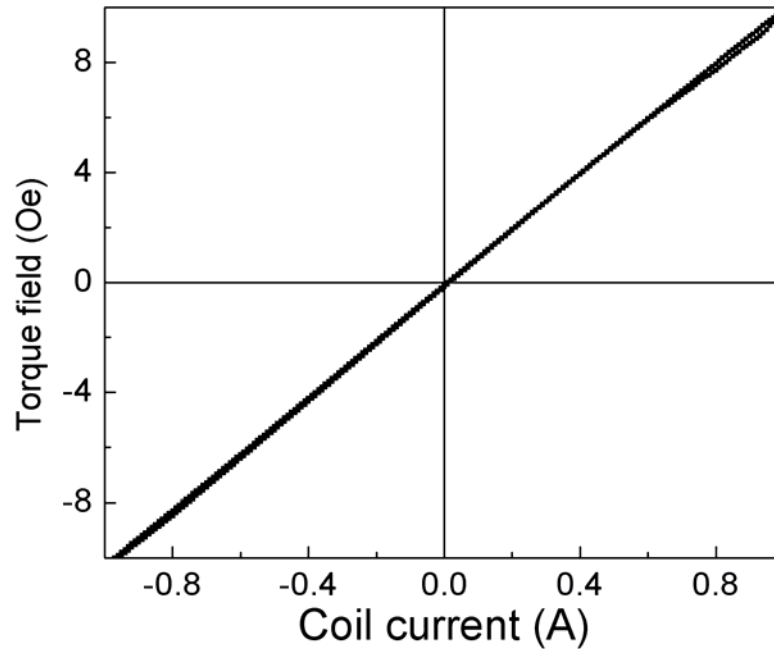


Fig. 2.8 Calibration of torque field versus coil current.

2. 2. 2 Optical interferometer

The optical interferometer is a sensitive instrument to detect a displacement change [4-6]. The schematic diagram of a fiber optic interferometer is as shown in Fig. 2.9. Two optical interferometers are used in the study. The laser source of one optical interferometer is a laser diode (AFM interferometer 0022-2000) and the other one is HP 8164 A. The wavelength of the laser source is 1543.68 nm to 1547.83 nm for laser diode [7] and 1510 nm to 1640 nm for HP 8164A lightwave measurement system [8]. An optical isolator is added, so light can only come out and cannot go back to the laser source. The output laser beam from the fiber is reflected by the surface of the sample (cantilever) and comes back into the fiber. The reflected laser beam is then detected by a photoreceiver. The photoreceiver, which translates the light signal to a voltage signal.

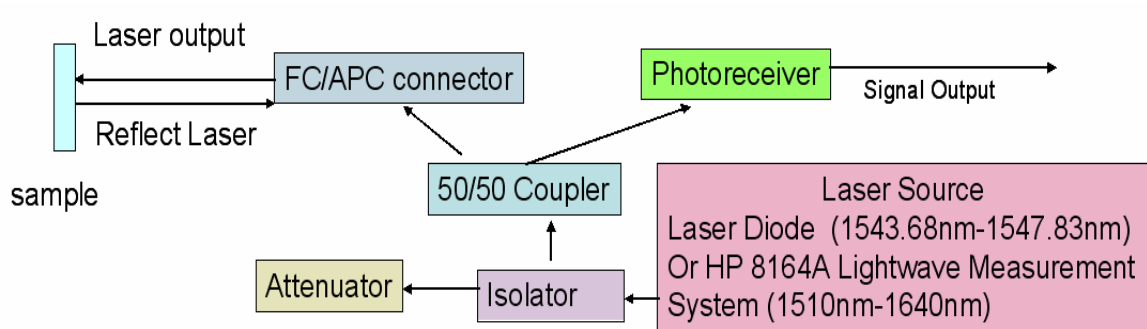


Fig. 2.9 Schematic diagram of the interferometer

The photo receiver (New focus, Model 2034) can detect light with wavelengths between 800 nm and 2200 nm. It has three ranges, low, medium, and high, which transimpedance gains 2×10^3 , 10^5 , and 2×10^6 V/A, respectively. The noise equivalent power (NEP), which is a measure of the weakest optical signal that the photoreceiver can detect, is 46 pW/ $\sqrt{\text{Hz}}$. To compute the approximate output voltage for a given input optical power, the relationship $V_{\text{out}} = P_{\text{in}} \cdot R \cdot G$ is used, where P_{in} is the input optical power in watts; R is the photo detector's responsivity in A/W (Fig. 2.10), and G is the amplifier's transimpedance gain in V/A. For example, the Model 2034 on the medium gain setting and with 10 μW of optical power at 1600 nm will have an output voltage of approximately $(10 \mu\text{W}) \cdot (1 \text{ A/W}) \cdot (10^5 \text{ V/A}) = 1 \text{ V}$. If the 3 dB bandwidth is 80 kHz, the voltage corresponding to the minimum detectable signal is $(46 \text{ pW}/\sqrt{\text{Hz}}) \cdot (80 \text{ kHz}) \cdot (1.1 \text{ A/W}) \cdot (2 \cdot 10^6) = 3.6 \cdot 10^{-7} \text{ V}$.

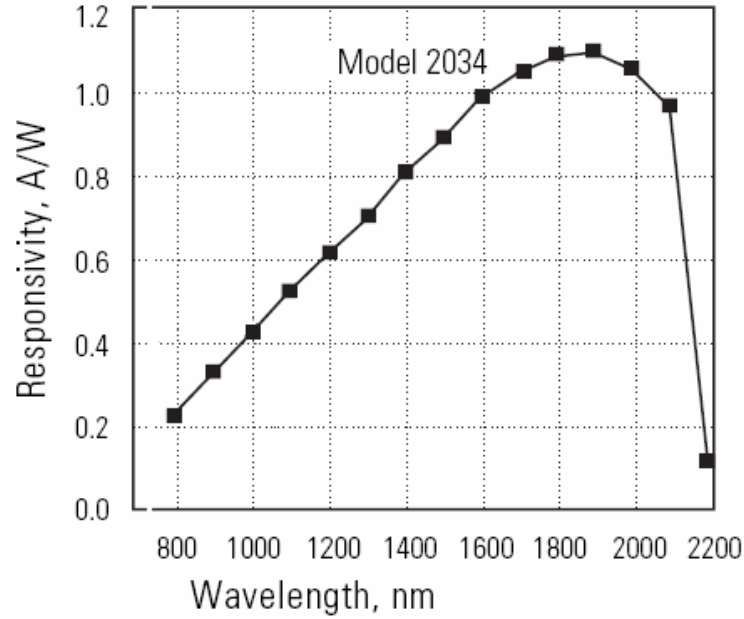


Fig. 2.10 Typical responsivity of the model 2034 photodiode

Simple two-component interference is used to model the interferometer response. The voltage from the signal photodiode is given by $v = v_0[1 - V \cos(4\pi d / \lambda)]$, where λ is the laser wavelength and the d is the fiber-to-cantilever spacing, and v_0 is the midpoint voltage [9]. The quantity V is the fringe visibility and given by $V = \frac{v_{\max} - v_{\min}}{v_{\max} + v_{\min}}$ and $v_0 = (v_{\max} + v_{\min})/2$, where v_{\max} and v_{\min} are the voltage corresponding to maximum constructive and destructive interference, respectively. Then is the laser wavelength is driven to λ_1 and gets a maximum output, then

$$\begin{aligned} \cos(4\pi d / \lambda_1) &= 1 \\ 4\pi d / \lambda_1 &= 2m\pi \\ d &= \frac{m}{2} \lambda_1 \end{aligned} \quad (2-1)$$

where m is an integer. If the next maximum peak occurs at some wavelength λ_2 , then

$$d = \left(\frac{m+1}{2}\right)\lambda_2 \quad (2-2)$$

Combine equation (2-1) and (2-2), the fiber-to-cantilever spacing can be determined by

$$d = \frac{\lambda_1 \lambda_2}{2(\lambda_1 - \lambda_2)}.$$

In Fig. 2.11, the fiber-to-cantilever spacing is the etching depth of the cantilever from the wafer, which is designed as $135 \mu\text{m}$. And from the experiment, the distance is

$$d = \frac{1566\text{nm} \times 1575\text{nm}}{2 \times (1575\text{nm} - 1566\text{nm})} = 137 \mu\text{m}.$$

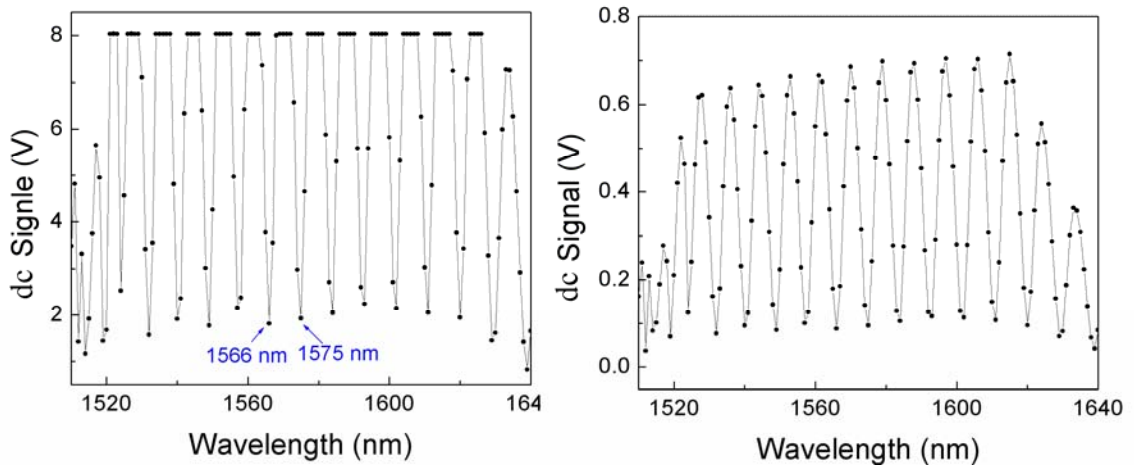


Fig. 2.11 the dc output with changing laser wavelength at a fixed fiber-to-cantilever distance at (a) high sensitivity range and (b) medium sensitivity range of the photoreceiver.

The most sensitive operating point occurs when $d = \lambda/8, 3\lambda/8, 5\lambda/8, \dots$. At quadrature, the response for small distance changes, Δd , and the small wavelength change $\Delta\lambda$, is

given by $dv = v_0 V \sin \frac{4\pi d}{\lambda} \left(\frac{4\pi \Delta d}{\lambda} - \frac{4\pi d \Delta \lambda}{\lambda^2} \right)$. At $d = (2n+1)\lambda/8$, where n is any integer,

the equation becomes as $\frac{\Delta v}{v_0} = 4\pi V \left(\frac{\Delta d}{\lambda} - \frac{d\Delta\lambda}{\lambda^2} \right)$. As shown in Fig. 2.12, the voltage from the signal photodiode (dc voltage) and ac signal from the lock-in amplifier varies with changing laser wavelength. As the wavelength decreases from 1547.83 nm, the dc and ac signals both increase. The ac signal reaches a maximum when the wavelength is 1546.3 nm. As the wavelength decreases more, the dc signal increases and the ac signal decreases. By comparing the dc and ac signals, the ac signal reaches zero when the dc signal is at a maximum or minimum voltage; and ac signal gets maximum at the dc signal is the middle point of the maximum and the minimum output voltage.

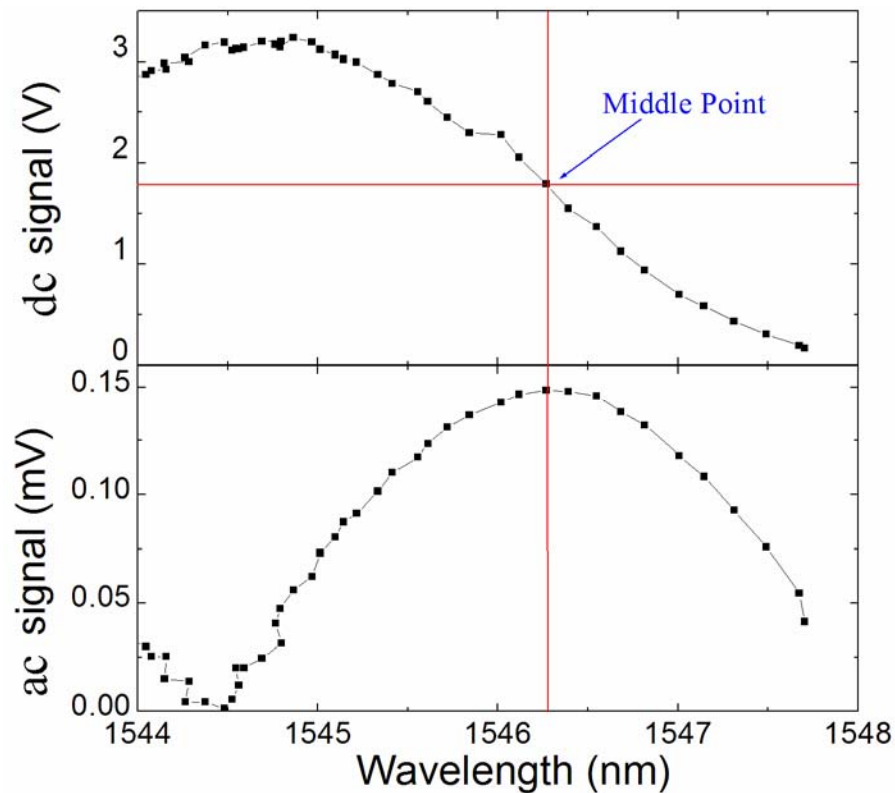


Fig. 2.12 The voltage of the photodetector output and ac voltage from lock-in amplifier as a function of wavelength of the laser source.

To get the maximum sensitivity, we can either change the fiber-cantilever spacing, or change the wavelength of the laser [10]. The wavelength of the laser can be adjusted by the temperature of the laser diode. During the measurement, the laser wavelength is adjusted until the signal photodetector voltage $v_0=(v_{max}+v_{min})/2$. Then to ensure that the interferometer can be calibrated within the maximum wavelength shift of the laser $\Delta\lambda$, the fiber-cantilever spacing d need to satisfy the condition of $d \geq (\lambda^2 + \lambda\Delta\lambda)/2\Delta\lambda$. The laser wavelength range of the laser diode in AFM interferometer 0022-2000 is from 1543.68 nm to 1547.83 nm, and for the other system (HP 8164A) is from 1510nm to 1640nm. Then the minimum fiber-cantilever spacing is 137.5 μm and 19 μm . The maximum output voltage from the detector is 5 V, and the minimum output step is 3.6×10^{-7} . Then the minimum displacement can be detected by the interferometer is

$$\Delta d = \frac{3.6 \times 10^{-7} \text{ V}}{5 \text{ V}} \times 19 \mu\text{m} = 7 \text{ fm}.$$

2.2.3 Microcantilever

The microcantilever used in the microcantilever torque magnetometry (MTM) systems is fabricated from a double-sided polished <100>-oriented, single-crystal silicon wafer 75mm in diameter and 150 μm in thickness. The fabrication process is done in National Institute of Standard and Technology (NIST) at Boulder, Colorado. The detailed fabrication process of the microcantilever is shown in Fig. 2.13. First a thin photoresist layer about 2 μm thick is coated on the wafer. The photoresist is patterned by the UV light from the top. After that, a deep RIE process is used to remove the Si substrate not covered with photoresist to a depth of about 15 μm . This process defines the cantilever. Next, 0.5 μm thick Si_3N_4 is deposited on both sides of the wafer. And the backside nitride is then patterned using both reactive ion etching (RIE) and deep RIE

(DRIE). Then the DRIE is used to remove the Si in the backside about 130 μm at the position where will be the cantilever. The cantilever release process is based on a KOH anisotropic etch (30 % by weight with 2-3% of isopropyl alcohol (IPA), and an oxygen bubbler at 75°C). Finally, the Si_3N_4 is removed by the 1% HF solution. Fig. 2.14 shows some of cantilevers that fabricated by this process.

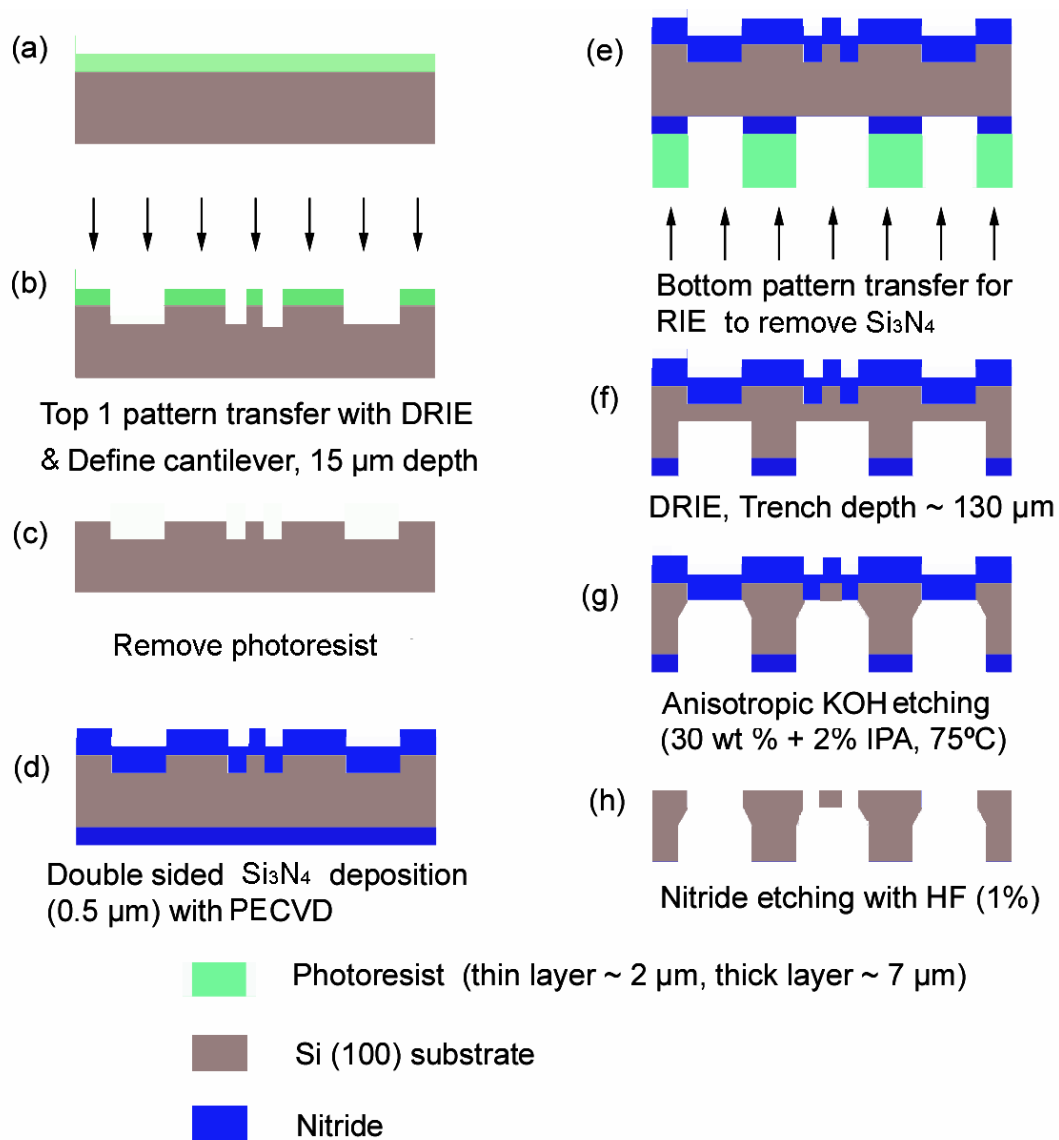


Fig. 2.13 Schematic diagram of the fabrication process of cantilevers.

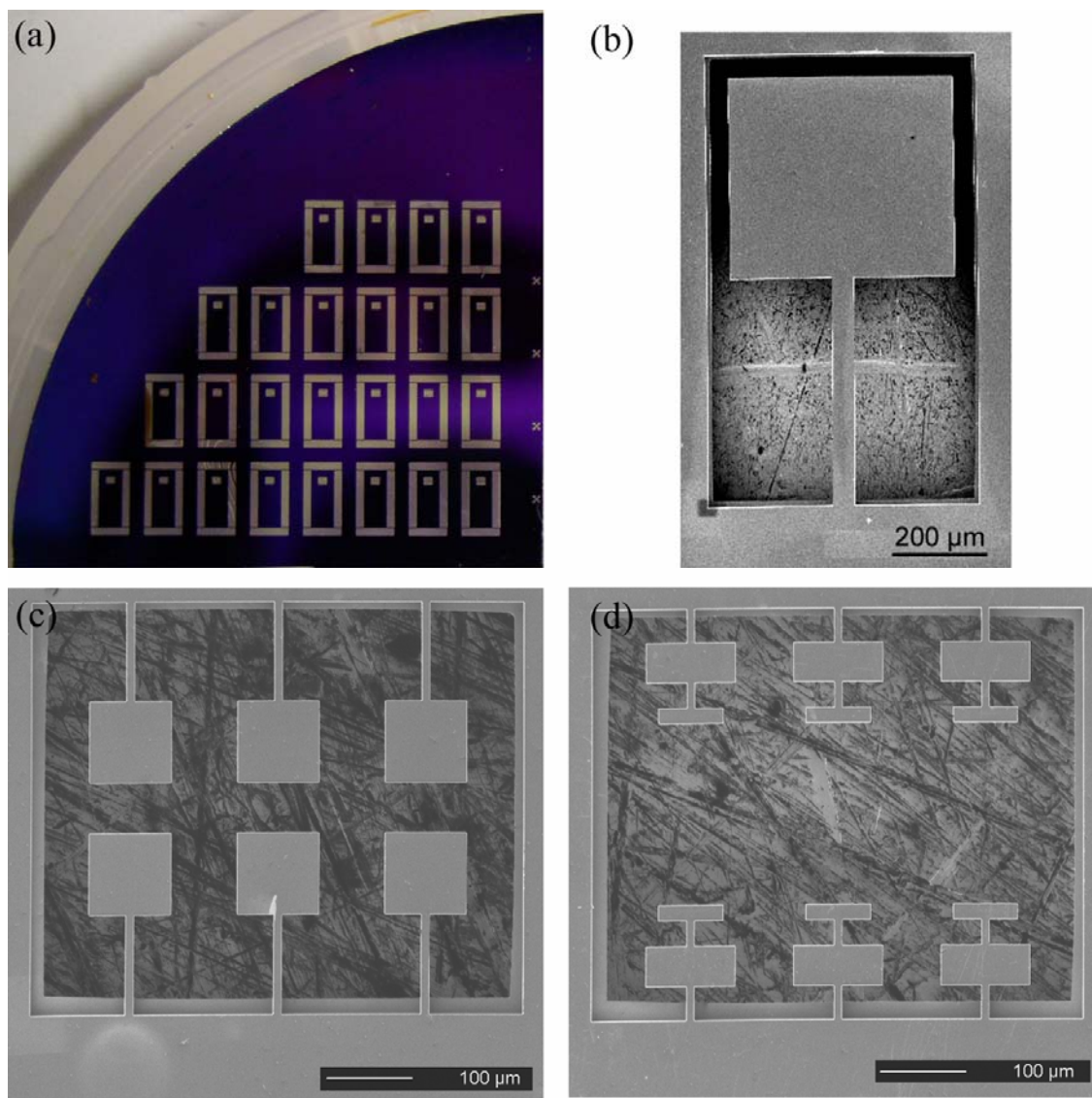


Fig. 2.14 (a) Photograph of the wafer and (b) (c) (d) cantilevers with different dimensions and shapes.

References:

1. Silvia Signoretti, Conradin Beeli, Sy-Hwang Liou, "Electron holography quantitative measurements on magnetic force microscopy probes", *J. Magn. Magn. Matt.*, **272-276**, 2167 (2004).
2. R. Wiesendanger and H. J. Güntherodt "Scanning Tunneling Microscopy", second version, Springer, p. 164-165 (1995).
3. Ching Tsang, "Magnetics of small magnetoresistive sensors", *J. Appl. Phys.* **55**, 2226 (1984).
4. Jukka Hast, Leszek Krehut, and Risto Myllylä, "Displacement sensor based on optical feedback interferometry in a GaN laser Diode", *Optical Engineering*, **44**, 080504 (2005).
5. T Fujii, M Suzuki, M Yamaguchi, R Kawaguchi, H Yamada and K Nakayama, "Three-dimensional displacement measurement of a tube scanner for a scanning tunneling microscope by optical interferometer", *Nanotechnology*, **6**, 121 (1995).
6. Peggs G. N and Yacoot A., "A review of recent work in sub-nanometre displacement measurement using optical and X-ray interferometry", *Philos. Transact. A Math. Phys. Eng. Sci.*, **360 (1794)**, 953 (2002).
7. Manual of Lamda Light Tunable DFB laser, Laser Module Characteristics.
8. Agilent 8164 A Lightwave measurement system, 81640A tunable laser to the test of critical components in both dense-WDM bands.
9. D. Rugar, H. J. Mamin, and P. Guethner, "Improved fiber-optic interferometer for atomic force microscopy", *Appl. Phys. Lett.*, **55**, 2588 (1989).

10. K. J. Bruland, J.L.F., W. M. Dougherty, S. H. Chao, S. E. Jensen, and J. A. Sides, "Thermal tuning of a fiber-optic interferometer for maximum sensitivity", *Rev. Sci. Instrum.*, **70**, 3542 (1999).

Chapter 3

Locating magnetic noise sources in magnetic sensors

In this chapter, we correlate the microstructure to the source of magnetic noise in giant magnetoresistance (GMR) and magnetic tunneling junction (MTJ) recording heads using our newly developed magnetic sensitivity mapping (MSM) system [1, 2]. A scanning nanometer-sized magnetic tip was used to generate a localized magnetic field and excite the free-layer magnetic moment at the air-bearing surface (ABS). By mapping out the magnetic noise as a function of position, the inhomogeneous regions in the ferromagnetic layer of the magnetic sensors that relate to magnetic instabilities inside the recording heads are identified. An understanding of those nanometer sized defects is important to design heads with better signal to noise ratio (SNR).

3.1 Giant magnetoresistance junction

GMR heads are current-in-plane devices composed of multilayer structures of magnetic and a very thin nonmagnetic metal layers (typically Cu) [3-4]. Currently the GMR heads have a spin-valve structure (Fig. 3.1) [5]. The magnetization of one ferromagnetic layer is pinned by exchange coupling with the adjacent antiferromagnetic layer. The magnetization direction of this ferromagnetic layer cannot be changed by a small magnetic field (this layer is called the pinned layer). While the other magnetic layer's moment direction can be easily altered by a small magnetic field (this layer is called the free layer). When the magnetization directions of the two ferromagnetic layers are parallel, the GMR has low resistance; otherwise, it has high resistance. The origin of

the GMR can be qualitatively explained by the Mott model [6]. It is proposed that the up-spin and down-spin are two independent conducting channels. Due to the asymmetry in the density of states at the Fermi level, the scattering is strong for electrons with spin antiparallel to the magnetization direction and weak for electrons with spin parallel to the magnetization direction. In the case of parallel alignment of the magnetization direction of two ferromagnetic layers, the up-spin electrons are parallel to the magnetization direction and then pass through with less scattering, while the down-spin electrons scatter strongly within the ferromagnetic layers. Since the two conduction channels are in parallel, the up-spin channel which has the low resistance, will dominate. On the contrary, when the magnetization directions of the two ferromagnetic layers are antiparallel, both the up-spin and down-spin electrons are antiparallel to the magnetization direction of one of the ferromagnetic layers and are scattered strongly within that ferromagnetic layer. That results in high resistance. Therefore, the variation of the magnetization direction in the ferromagnetic layers will affect the scattering process, change the resistance, and then cause noise. The factors can change the magnetization direction of the free layer could be thermal excitations, defects made during film deposition, interface diffusion, *etc.*

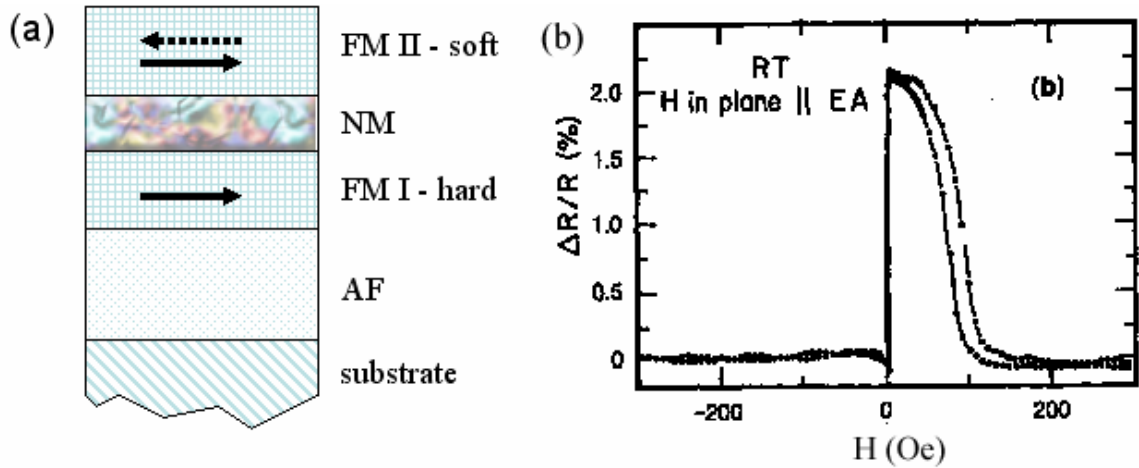


Fig. 3.1 (a) Layer structure of a GMR sensor and (b) Magnetoresistance for one GMR with layer structure as Si/NiFe/Cu/NiFe/FeMn/Ag as a function of H in the film plane at room temperature. The field is applied parallel to the exchange anisotropy field created by FeMn (EA). The current is perpendicular to this direction [5].

3.2 Magnetic tunneling junction (MTJ)

The MTJ sensor has a similar tri-layer structure as GMR (Fig. 3.2) [7]. The differences between the MTJ and GMR heads are that MTJ is a current-out-of-plane device and the nonmagnetic spacer layer is replaced by a thin oxide layer (1.0 nm or less). When the insulating barrier is very thin, electrons can tunnel through it. The number of tunneling electrons is related to the relative orientation of the magnetization of the two ferromagnetic layers. When the two ferromagnetic layers are magnetized parallel to each other, the resistance is low; when the magnetization directions of the two ferromagnetic layers are antiparallel, the resistance is high.

This phenomenon was explained by a simple model proposed by Julliere [8]. It assumed the spin of electrons is conserved in the tunneling process. When the electrons

originate from one ferromagnetic layer, they will be accepted by the unfilled states of the same spin of the second ferromagnetic layer. If the two ferromagnetic layers have magnetization directions aligned parallel to each other, the minority (majority) spins tunnel to the minority (majority) states. While if the two ferromagnetic layers are magnetized antiparallel, the majority (minority) spins of the first ferromagnetic layer will tunnel to the minority (majority) state of the second ferromagnetic layer. Julliere also assumed that the conductance for a certain spin orientation is proportional to the product of the effective density of states of the two ferromagnetic electrodes. Therefore the resistance for the parallel alignment is low and the resistance for the antiparallel alignment is high.

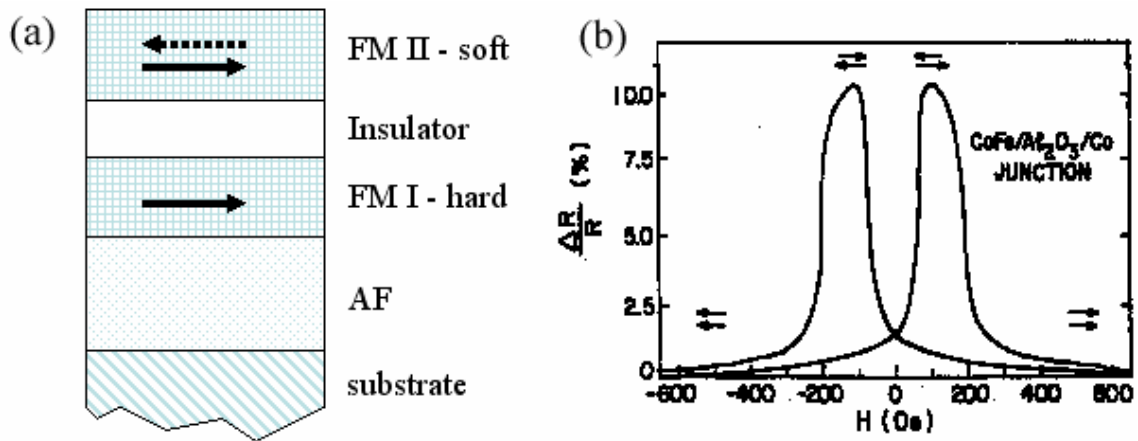


Fig. 3.2 (a) Layer structure of a MTJ sensor and (b) Magnetoresistance for one MTJ with layer structure of CoFe/Al₂O₃/Co plotted as a function of H in the film plane at 295 K [7].

With the improvement in thin film deposition and barrier oxidation, the TMR value increases. The highest reported MR ratio for MTJ is about 70% using an Al₂O₃ barrier

layer [7] and 200% using MgO barrier layer [10-11] at room temperature. Recently, MTJ using MgO barrier with rf-sputtered CoFeB electrodes completely crystallized by annealing at 400 °C have shown TMR ratio exceeding 350% [12, 13]. And by adding synthetic ferromagnetic pin layer annealed at 425 °C, TMR can get further increases to 361% [14]. However, the TMR and SNR values are very sensitive to the microstructures caused during the head fabrication process.

3.3 Magnetic noise

In order to use GMR and TMR sensors as recording heads for even higher recording densities, higher MR as well as higher signal-to-noise (SNR) ratio are very important. Therefore, in order to realize the full potential of the GMR and TMR sensor, a detailed understanding of noise and magnetic stability characteristics of the sensor are essential for the design of high SNR heads.

From the discussions of the layer structures of GMR and TMR heads, there are many mechanisms that can cause resistance change and then increase the noise in a submicron scale MR read heads. Some are magnetic in nature and some are purely electrical in nature. Examples of those mechanisms include Johnson-Nyquist thermal resistance noise, shot noise, random telegraph noise (both can be due to magnetic fluctuation or purely nonmagnetoresistive resistance fluctuations), $1/f$ noise, *etc.*

Johnson-Nyquist noise, also called white noise, exists in all resistive devices [15]. It is due to thermal fluctuations in the electron density within the resistor itself. The noise is measured without applied external bias. For GMR, the thermal smearing of the distribution function of electrons near the Fermi-level will cause resistance change and

result in noise. And for MTJ, for those electrons with energy close to the barrier height, the thermal energy may assist these electrons tunnel through the barrier. This random transition of electrons between two electrodes through tunnel barrier results in current fluctuation. Usually this type of current fluctuation is small. By using the fluctuation-dissipation theorem (FDT) to thermal equilibrium resistance fluctuations (without external bias voltage), the Johnson-Nyquist noise can be expressed as

$$V_{noise}(rms) = \sqrt{4kTR\Delta f}$$

where the k is Boltzmann's constant (1.38×10^{-23} J/K), R is the total tunnel resistance in ohms, T is the absolute temperature in Kelvin, and Δf is the bandwidth in Hz.

Shot noise is due to the finite nature of the charge carriers. There is always some non-uniformity in the electron flow which will generate noise in the current. Also with a bias voltage applied across the barrier of MTJ, the probability of electrons tunneling through the barrier is increased. The number of electrons tunneling through the barrier per unit time fluctuates. The shot noise can be expressed as

$$I_{noise}(rms) = \sqrt{2qI\Delta f}$$

where q is electron charge (1.6×10^{-19} C), I is electrical current and Δf is the bandwidth [16].

A third noise source is 1/f noise, or flicker noise [14,15]. It usually dominates in the low frequency range. The power spectral density of this noise follows the well known

Hooke relation [17], $S_V = \frac{\alpha_H V^2}{N f^\gamma}$, where α_H is the "Hooge constant", N is the number of charge carriers in the sample, f is the frequency, and the exponent γ is usually close to 1. If we assume the charge carrier density is constant, then we can replace N by the sample

volume, V . So the $1/f$ noise is inversely proportional to the sensor size. Many models have been proposed to explain the root causes of $1/f$ noise. The most plausible and generally accepted model for $1/f$ noise is the two level fluctuation model conceived by Dutta and Horn [18]. This two level-fluctuation model can also describe most noises caused by magnetic fluctuations.

Thermal noise and shot noise are intrinsic properties of the sensor. We have very little control after the material and structures have been chosen. However, noise caused by magnetic instability in the sensor can be controlled by the magnetic properties of the relevant magnetic layers and stabilizing methods. Most of the magnetic instabilities are caused by the so-called Barkhausen jumps, which arise from sudden and irreversible domain wall motion. The magnetic instabilities are likely due to processing defects, edge defects or non uniformities in the magnetic layer.

From the principle of GMR and MTJ sensors, the output signal is closely related to the magnetization states in the free and pinned layer structures. Magnetic instabilities will show up as electrical noise on the output signal. The origins of these noise sources are different. However, they are all related to the microstructure of the heads. For example, the magnetic instabilities caused by the so-called Barkhausen jumps arise from sudden and irreversible domain wall motion pinned by the defects. Those defects can be formed during thin film deposition process, defects during the lithography process, interface intermixing, *etc.* As the size of the magnetic elements shrinks, the thickness of the ferromagnetic film and spacer decrease, the chance of having defects becomes higher. Therefore, in order to realize the full potential of the GMR and MTJ sensors, a detailed understanding of noise and magnetic stability characteristics of the sensor are essential

for the design of high signal-to-noise ratio (SNR) sensors. Recently, great efforts have been exerted in the study of GMR and MTJ noise and attempt to explain the noise mechanisms involved [19-24]. Most of these reports focus on the integrated noise behavior of MR heads, but a few concentrate on spatial characterization of the noise source. For submicron sized sensors, it is very hard to observe their microstructure.

In this study, a dynamic magnetic sensitivity mapping (MSM) system was designed to investigate the localized noise sources associated with magnetic instabilities in GMR and TMR recording heads, and then correlate the information to the microstructure of the recording heads.

3.4 MSM mapping

3.4.1 MSM mapping GMR sensor

Several selected GMR and MTJ recording heads with known magnetic instabilities are measured by the MSM system. For the tested magnetically unstable GMR recording heads, the study of the noise spectrum indicates that noise in the low-frequency regime is the dominant noise source. This is consistent with random telegraph noise [26, 27]. Fig. 3.3 shows noise MSM images in the range of 20 kHz to 60 kHz for one of the tested unstable GMR sensors under positive (negative z axis) and negative (positive z axis) tip magnetization. It is clear that under a positive excitation field, noise mainly originates from the right part of the sensor in a semicircular shaped area [Fig. 3.3 (a)]. However, under a negative excitation field, no detectable noise is present in the whole sensor, as shown in Fig. 3.3 (b). These results are reproducible for other MFM tips which have different magnetic stray fields. Therefore the stray field from the MFM tip only

exaggerates the instability in the head. The location of the instability is not related to the tip but intrinsic to the head.

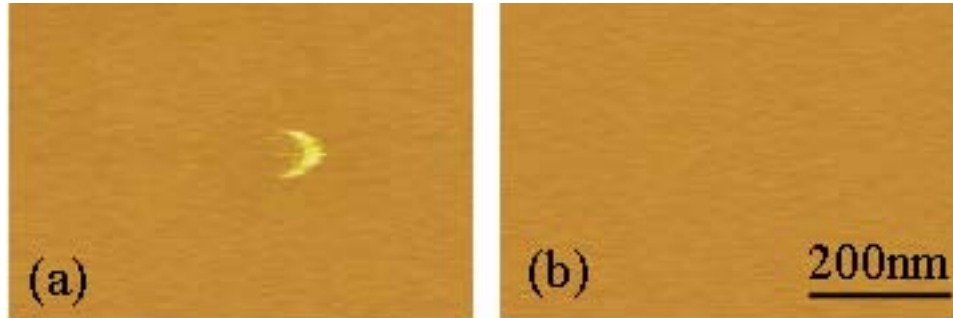


Fig. 3.3 MSM images (a) under a positive and (b) under a negative magnetic field for a magnetically unstable GMR read head.

3.4.2 MSM mapping for MTJ sensor

Fig. 3.4 (a) shows the dc noise measurement in the time domain for two MTJ recording heads under an external sweeping magnetic field. One of the heads is magnetically stable while the other has a known magnetic instability. For the stable head [head 1 in Fig. 3.4 (a)], the baseline noise is small and has no significant change with the applied dc magnetic field. For the unstable head [head 2 in Fig. 3.4 (a)] under a negative dc field, the baseline noise is about the same as the stable head. When the field increases to a bout 5 kA/m, baseline noise increases dramatically. As the field is further increased, the noise subsides. When the applied field decreases from a high positive field and then reverses back to 3 kA/m, noise again increases but then falls off with further field decrease. The MR transfer curve of the stable head is shown in Fig. 3.4 (b). When no

external field is applied, the resistance of the head 1 is about 92.8Ω . When magnetic field is applied, the resistance changes linearly with field changes and is symmetric about the positive and negative field. Head 2 has resistance about 154.7Ω with no applied field. However the MR transfers curve of head 2 (Fig. 3.4 (c)) is not linear but has a hysteresis loop. In addition, the MR curve is not symmetric about 154.7Ω for the same amplitude applied magnetic field with opposite directions. The transition between high and low resistance states both happened under positive fields. Also by comparing the MR curve to the time domain noise measurement, we find that the fields which cause increased noise correspond to the switching field of the sensor between high and low resistance states. Magnetic moment fluctuations in the free layer may cause this noise increase [20, 21].

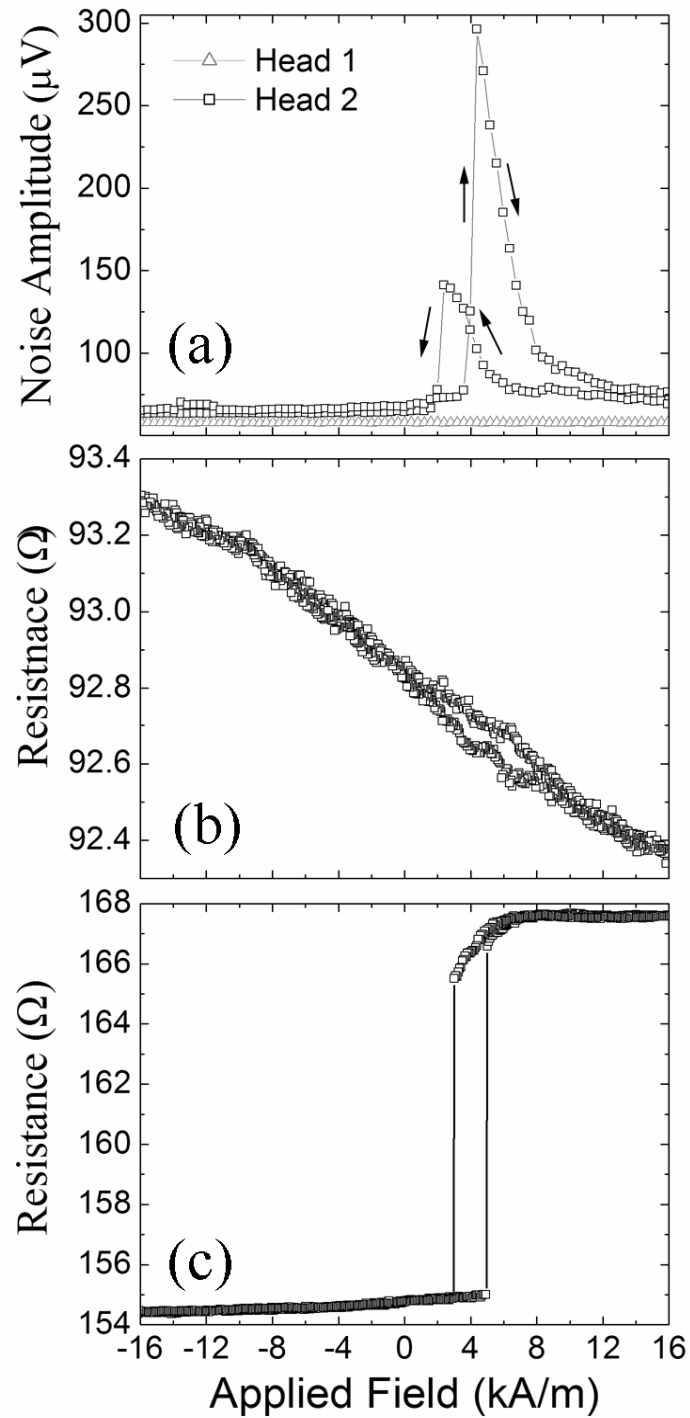


Fig. 3.4 (a) Time domain measurement of the noise amplitude under an external magnetic field for a stable MTJ head (Head 1) and an unstable MTJ head (Head 2); (b) MR loop for MTJ head 1 and (c) MR loop for MTJ head 2.

The noise mapping images of stable and unstable MTJ heads with positive and negative tip magnetization in the frequency range of 20 kHz to 60 kHz are shown in Fig. 3.5. For a stable head (head 1), the noise maps [Fig. 3.5 (a) and (b)] show that there is no additional noise due to magnetic tip excitation whether under a positive or a negative tip magnetization state. However, the noise map for an unstable head (head 2) [Fig. 3.5 (c)] shows that there is considerable noise having spatial variation. A magnetic noise increase is detected only during tip scanning over the left side of the sensor and a small amount of noise is observed in the right part of the sensor. Upon reversing the tip field direction, this localized magnetic noise disappears [Fig. 3.5 (d)]. These results agree with the time domain measurement results as shown in Fig. 3.4 (a).

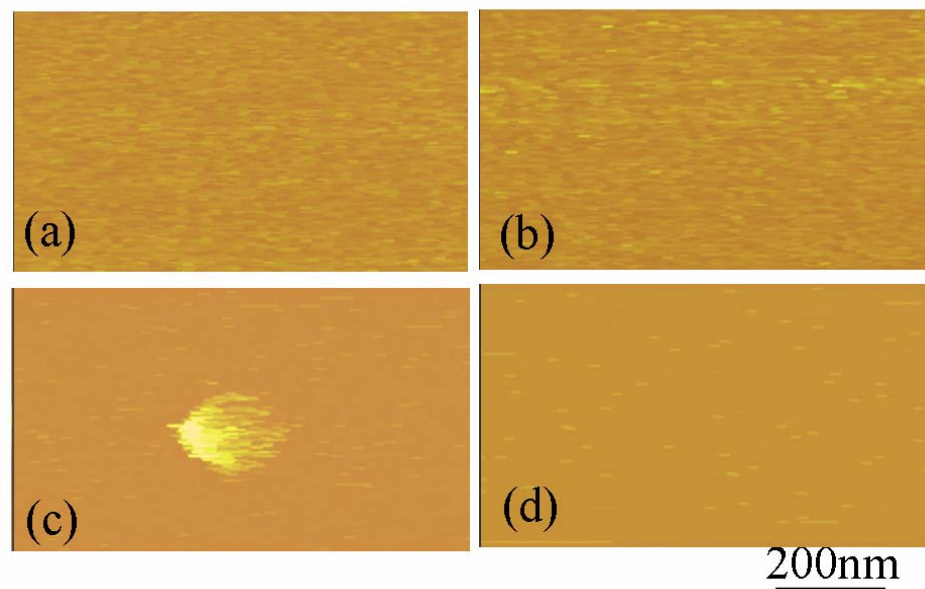


Fig. 3.5 MSM images for the MTJ head 1 (stable) (a) under a positive magnetic field and (b) under a negative field; and for magnetic MTJ head 2 (unstable) (c) under a positive magnetic field and (d) under a negative field.

One possible reason for the noise increase under positive tip field for measured recording heads is magnetic defects in some regions of the free layer, such as processing defects, edge defects, or non-uniformities in the layer structure. These defect regions may weakly couple to the rest of the free layer [22] and cause the magnetic instability. By the analysis of the MR loop of the MTJ recording head 2 (unstable), the magnetization of the defects in the free layer is not aligned by the CoCrPt hard magnets to the perpendicular direction (x axis in Fig. 2.3) to the magnetization direction of the pinned layer. The direction of that defect region favors the parallel alignment to the pinned layer. It may be caused by the exchange coupling from the pinned layer. A small field in the direction antiparallel to the magnetization direction of the pinned layer cannot rotate the magnetization of the free layer with it. Unless the field is high enough to overcome the pinning by the defects in the free layer, the free layer is magnetized with the applied field. It causes a sudden change in resistance. Also the magnetic instabilities caused by defects in the free layer result in hysteresis. This makes the loop shift to the positive field side. Therefore the resistance changes all happen under positive fields. When the tip magnetization is positive, the activation energies from tip, hard magnet, and current-induced field form a quasi-equilibrium state in the defect region of the sensor. Thermal energy then allows the domain walls to hop between pinning sites [20], causing increased noise. The defect region in the TMR sensor is likely located in the center of the circular area in the left part of the sensor. With a negative tip magnetization, the TMR sensor is in a stable low resistance state and no noise is observed. Similarly, from the semicircular shape of the noise MSM image of the GMR head, it is very likely that the location of the

fluctuating magnetic moment is located in the center of the semicircular shaped area of the head.

3.5 Summary

In this chapter, we have presented results of the imaging of the magnetic noise sources at low frequency in both GMR and MTJ recording heads. The developed MSM system can locate the magnetic noise sources for the sub-micron sized heads, which is hard to be observed by other methods. The agreement between the image of noise sources and other measurement results is good for the investigated magnetic origin noise in recording heads. The field dependent $1/f$ noise and Barkhausen noise may be the main reasons for the noise increase of the unstable recording heads we tested.

References:

1. L. Yuan, J. X. Shen, Bharat B. Pant and S. H. Liou, "Imaging magnetic noise sources in magnetic recording heads(invited)", Proceeding of SPIE- Fluctuations and Noise in Materials, **5843**, 1 (2005).
2. L. Yuan, J. X. Shen, and Bharat B. Pant, "Locating magnetic noise sources in TMR and GMR recording heads using scanning probe microscopy", IEEE Trans. Magn., **40**, 2233 (2004).
3. M. N. Baibich, J. M. Broto, A. Fert, F. Nguyen Van Dau, F. Petroff, P. Etienne, G. Creuzet, A. Friederich, and J. Chazelas, "Giant magnetoresistance of (001)Fe/(001)Cr magnetic superlattices", Phys. Rev. Lett., **61**, 2472 (1988).
4. G. Binasch, P.Grünberg, F. Saurenbach, and W. Zinn, "Enhanced magnetoresistance in layered magnetic structures with antiferromagnetic interlayer exchange", Phys. Rev. B, **39**, 4828 (1989).
5. B. Dieny, V. S. Speriosu, S. S. P. Parkin, B. A. Gurney, D. R. Wilhoit, and D. Mauri, "Giant magnetoresistance in soft ferromagnetic multilayers", Phys. Rev. B, **43**, 1297 (1991).
6. N. F. Mott, Proc. Royal Soc., **156**, 368 (1936).
7. J. S. Moodera, Lisa R. Kinder, Terrilyn M. Wong, and R. Meservey, "Large magnetoresistance at room temperature in ferromagnetic thin film tunnel junctions", Phys. Rev. Lett., **74**, 3273 (1995).
8. M. Julliere, "Tunneling between ferromagnetic films", Phys. Lett., **54A**, 225 (1975).

9. Dexin Wang, Cathy Nordman, James M. Daughton, Zhenghong Qian, and Jonathon Fink, "70% TMR at room temperature for SDT sandwich junctions with CoFeB as free and reference layers", *IEEE Trans. on Magn.*, **40**, 2269 (2004).
10. Stuart S.P. Parkin, Christian Kaiser, Alex Panchula, Philip M. Rice, Brian Hughes, Mahesh Smant, and See-Hun Yang, "Giant tunnelling magnetoresistance at room temperature with MgO (100) tunnel barriers", *Nature Materials*, **3**, 862 (2004).
11. Shinji Yuasa, T.N., Akio Fukushima, Yoshishige Suzuki and Koji Ando, "Giant room-temperature magnetoresistance in single-crystal Fe/MgO/Fe magnetic tunnel junctions", *Nature Materials*, **3**, 868 (2004).
12. J. Hayakawa, S. Ikeda, F. Matsukura, H. Takahashi, and H. Ohno, *J. Appl. Phys.*, **44**, L587 (2005).
13. S. Ikeda, J. Hayakawa, Y. M. Lee, R. Sasaki, T. Meguro, F. Matsukura, and H. Ohno, *Jpn. J. Appl. Phys.*, **44**, L1442 (2005).
14. Y. Lee, J. Hayakawa, S. Ikeda, F. Matsukura, and Ohno, "Giant tunneling magnetoresistance in CoFeB/MgO/CoFeB magnetic tunnel junction with a synthetic ferrimagnetic pin layer annealed at and above 400 °C", Presentation HA-02, IEEE International Magnetism Conference, San Diego, California 2006.
15. Sh. Kogan, "Electronic noise and fluctuations in solids", Cambridge university press, New York, 1996.
16. Ya. M. Blanter and M. Büttiker, "Shot noise in mesoscopic conductors", *Phys. Rep.*, **336**, 1 (2000).
17. F. N. Hooge, T. G. M. Kleinpenning, and L. K. J. Vandamme, "Experimental studies on $1/f$ noise", *Rep. Prog. Phys.*, **44**, 479 (1981).

18. P. Dutta and P. M. Horn, "Low-frequency fluctuations in solids", *Rev. Mod. Phys.*, **53**, 497 (1981).
19. A. S. Edelstein, G. A. Fischer, M. Pedersen, E. R. Nowak, Shu Fan Cheng, and C. A. Nordman, "Progress toward a thousandfold reduction in $1/f$ noise in magnetic sensors using an ac microelectromechanical system flux concentrator (invited)" *J. Appl. Phys.*, **99**, 08B317 (2006).
20. Aisha Gokce, E. R. Nowak, See Hun Yang, and S. S. P. Parkin , " $1/f$ noise in magnetic tunnel junctions with MgO tunnel barriers", *J. Appl. Phys.*, **99**, 08A906 (2006).
21. Nathan A. Stutzke, Stephen E. Russek, David P. Pappas, and Mark Tondra , "Low-frequency noise measurements on commercial magnetoresistive magnetic field sensors", *J. Appl. Phys.*, **97**, 10Q107 (2005).
22. S. E. Russek, S. Kaka, W. H. Rippard, M. R. Pufall, and T. J. Silva, "Finite-temperature modeling of nanoscale spin-transfer oscillators" *Phys. Rev. B*, **71**, 104425 (2005).
23. L. Jiang, E. R. Nowak, P. E. Scott, J. Johnson, J. M. Slaughter, J. J. Sun, and R. W. Dave, "Low-frequency magnetic and resistance noise in magnetic tunnel junctions" *Phys. Rev. B*, **69**, 054407 (2004).
24. N. Stutzke, S. L. Burkett, and S. E. Russek, "Temperature and field dependence of high-frequency magnetic noise in spin valve devices" *Appl. Phys. Lett.*, **82**, 91 (2003).
25. M. B. Weissman, " $1/f$ noise and other slow, nonexponential kinetics in condensed matter", *Rev. Mod. Phys.*, **60**, 537 (1988).

26. P. Dutta, P. Dimon, and P. M. Horn, "Energy scales for noise processes in metals", *Phys. Rev. Lett.*, **43**, 646 (1979).
27. R. J. M. van de Veerdonk, P. J. L. Beliën, K. M. Schep, J. C. S. Kools, M. C. de Nooijer, M. A. M. Gijs, R. Coehoorn and W. J. M. de Jonge, " $1/f$ noise in anisotropic and giant magnetoresistive elements", *J. Appl. Phys.*, **82**, 6152 (1997).
28. Min Xiao, Klaas B. Klaassen, Jack C. L. van Peppen, and Mark H. Kryder, "Extra-low-frequency noise in giant magnetoresistance recording heads", *J. Appl. Phys.*, **85**, 5855 (1999).
29. S. Ingvarsson, Gang Xiao, S. S. P. Parkin, W. J. Gallagher, G. Grinstein, and R. H. Koch, "Low-frequency magnetic noise in micron-scale magnetic tunnel junctions", *Phy. Rev. Lett.*, **85**, 3289 (2000).
30. Alexey V. Nazarov, Hae Seok Cho, Janusz Nowak, Scott Stokes, and Ned Tabat, "Tunable ferromagnetic resonance peak in tunneling magnetoresistive sensor structures", *Appl. Phys. Lett.*, **81**, 4559 (2002).
31. L. S. Kirschenbaum, C.T. Rogers, S. E. Russek, and Young K. Kim, "Low-frequency noise in NiFe/Cu spin-valves", *IEEE Trans. Magn.*, **33**, 3586 (1997).

Chapter 4

Magnetic microstructures of free and pinned layer in magnetic tunnel junctions

The temperature and bias voltage dependence of magnetoresistance and the resistance of two types of magnetic tunnel junction (MTJ) samples were studied [1]. These two types of MTJ samples have different free layer structures, while having the same pinned layer structures and with the same materials for the free and reference layers. The layer structure for type 1 MTJs [Fig. 4.1 (a)] is 80Ru-8CoFeB-15Al₂O₃-50CoFeB-9Ru-54FeCo-350CrMnPt (in Å). The layer structure for type 2 MTJs [Fig. 4.1 (b)] is 80Ru-40CoFeB-50RuTa-40CoFeB-15Al₂O₃-50CoFeB-9Ru-54FeCo-350CrMnPt (in Å). Because the material for the free layer is the same for both types, the spin polarization should be the same for these two types of samples. Also the barrier preparation process is the same; therefore the barrier quality should be quite similar. However, very different experimental tunneling magnetoresistance (TMR) ratios are found for these two types of samples. The TMR ratio is about 26% and 69% at room temperature for type 1 and type 2 MTJs, respectively. A TMR as high as 107% has been observed for type 2 MTJ samples at 13 K. By analysis of the voltage and temperature dependence of the resistance and magnetoresistance in these MTJs, we discuss the detailed effects of the magnetic microstructures in the free layers and/or the interface between the free layer and the barrier layer, barrier qualities, and barrier interfaces on TMR behaviors. We show that for different free layer structures, even the same material may have quite different magnetization behaviors, which result in quite different TMR

ratios. The results clearly indicate that the micro-magnetization orientation at the interface between the free layer and the barrier layer is one of the important factors that determine the TMR ratio.

Also, the effect of microstructure in the pinned layer on the TMR behavior is studied. We applied a magnetic saturation field to tune the magnetization states in the pinned layers (The pinned layers are 350CrMnPt-54FeCo-9Ru-50CoFeB, and 50CoFeB is the reference layer.) without change the physical structures of the MTJ samples under ambient conditions. After applying different saturation fields, the minor loops are measured. A saturation field larger than the coercivity of the free layer will not change the magnetization properties of the free layer and only affect the pinned layers. Then the change in the minor loops will reflect the magnetic microstructures in the reference layer.

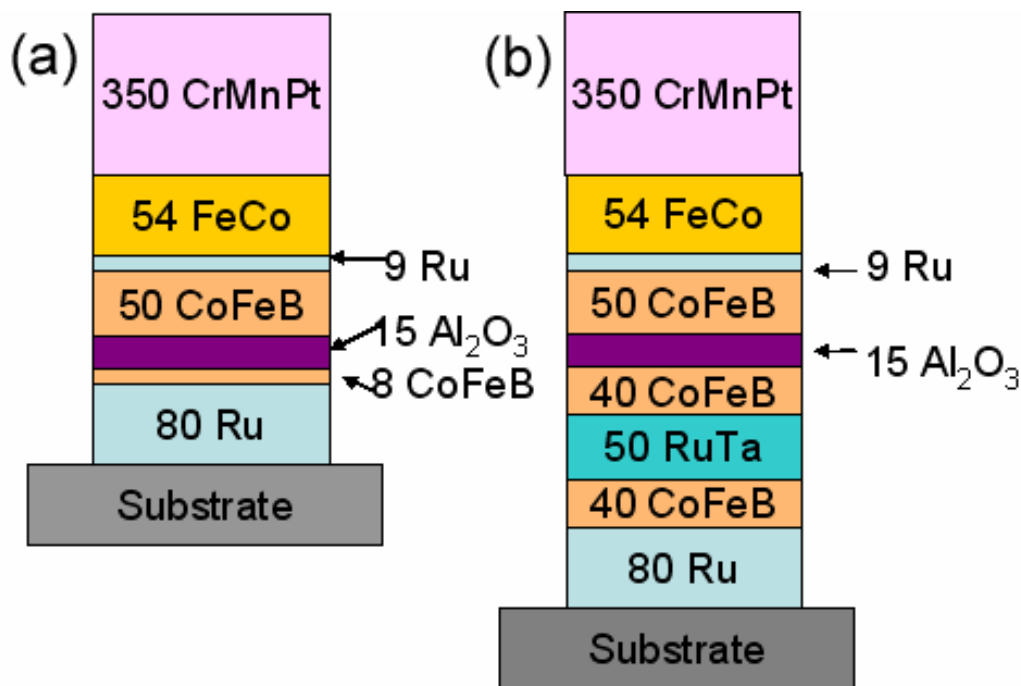


Fig. 4.1 The layer structures of (a) type 1 and (b) type 2 MTJ samples

4.1 Effect of magnetic state in free layer

4.1.1 Temperature dependence of magnetoresistance

The magneto-transport properties of the MTJs have been measured with a constant 10 mV bias voltage at various temperatures between 13 K and 300 K. For the MTJs, the minor loops are more interesting for practical applications, where only the magnetization of the free layer is switched while the pinned layer remains nearly unaffected. The minor loops were obtained by sweeping an external field of 20 kA/m (250 Oe) for type 1 and 8 kA/m (100 Oe) for type 2 devices in the direction along the easy axis of the magnetizations. Fig. 4.2 shows the MR minor loops for type 1 and type 2 MTJ samples at different temperatures. The RAP values at parallel (P) and antiparallel (AP) states both increase when the temperature decreases for both types of samples. At room temperature, the type 1 MTJ's RAP in the P state (R_P) is $120.1 \text{ M}\Omega\mu\text{m}^2$ and the RAP in AP state (R_{AP}) is $152.8 \text{ M}\Omega\mu\text{m}^2$; at 13 K, R_P and R_{AP} increase to $155.9 \text{ M}\Omega\mu\text{m}^2$ and $220.7 \text{ M}\Omega\mu\text{m}^2$, respectively. For type 2 MTJ, R_P and R_{AP} are $38.7 \text{ M}\Omega\mu\text{m}^2$ and $65.3 \text{ M}\Omega\mu\text{m}^2$ at 300 K and increase to $43.2 \text{ M}\Omega\mu\text{m}^2$ and $88.7 \text{ M}\Omega\mu\text{m}^2$ at 13K, respectively.

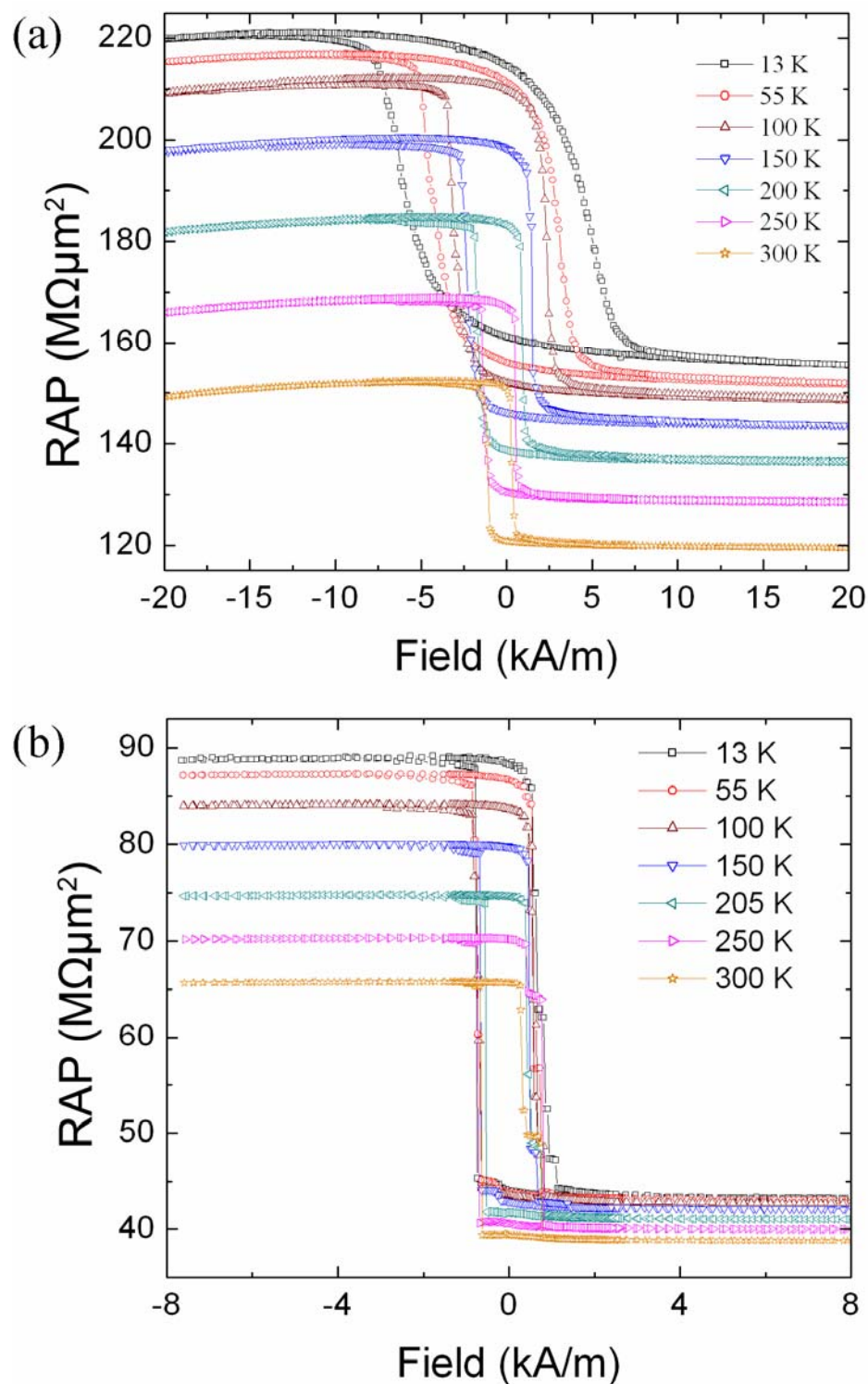


Fig. 4.2 Magnetoresistance transverse loops for (a) type 1 and (b) type 2 MTJs at temperatures between 13 K and 300 K.

For both type 1 and type 2, at room temperature the resistance transition between P and AP states happens at about 0.72 kA/m (9 Oe) and the transition is very sharp, but their transition behavior is quite different at lower temperatures. We define the squareness (S) of the MR loop as $S = (R_0 - R_m)/(R_{AP} - R_m)$, where $R_m = (R_{AP} + R_P)/2$ and R_0 is the resistance at zero fields after saturation in the AP state. From Fig. 4.3, we observe that the S values of type 1 MTJs does not have a significant change until the temperature decreases to under around 70K and that the S values of type 2 samples stay about the same. The low squareness of type 1 samples at lower temperature indicates that the magnetization of the free layer of type 1 is not switched with the field as homogeneously as that of the type 2.

The coercivity fields (H_c) of both types of samples increase as temperature decreases (Fig. 4.3). The H_c change with temperature for type 1 MTJ samples is much larger than that of the type 2 samples. At 300 K, the H_c is about 0.72 kA/m (9 Oe) for both types. However, the H_c of type 1 rises rapidly to 5.2 kA/m (65 Oe) at 13 K, while the H_c of type 2 exhibits no significant change.

The center of the MR loops shows a shift from zero fields. This field shift for both types of sample is small. For type 1 MTJ, it is 0.4 kA/m (5 Oe) and for type 2 MTJ, it is 0.14 kA/m (1.8 Oe). In both types of samples, a synthetic antiferromagnetic (SAF) structure, 54FeCo-9Ru-50CoFeB, has been applied to the pinned layer structures to reduce the shift field [2, 3]. However, as the temperature decreases, the coupling field for type 1 MTJs increases to about 0.64 kA/m (8 Oe), with no significant change for type 2. The small difference in the Néel coupling (or orange peel coupling) field in these two types of the samples is likely due to the different free layer structures. The additional

50Å RuTa and 40Å CoFeB layers in type 2 MTJs are designed to further control the CoFeB free layer next to the barrier so that a linear output can be obtained when patterned into certain shapes and processed accordingly.

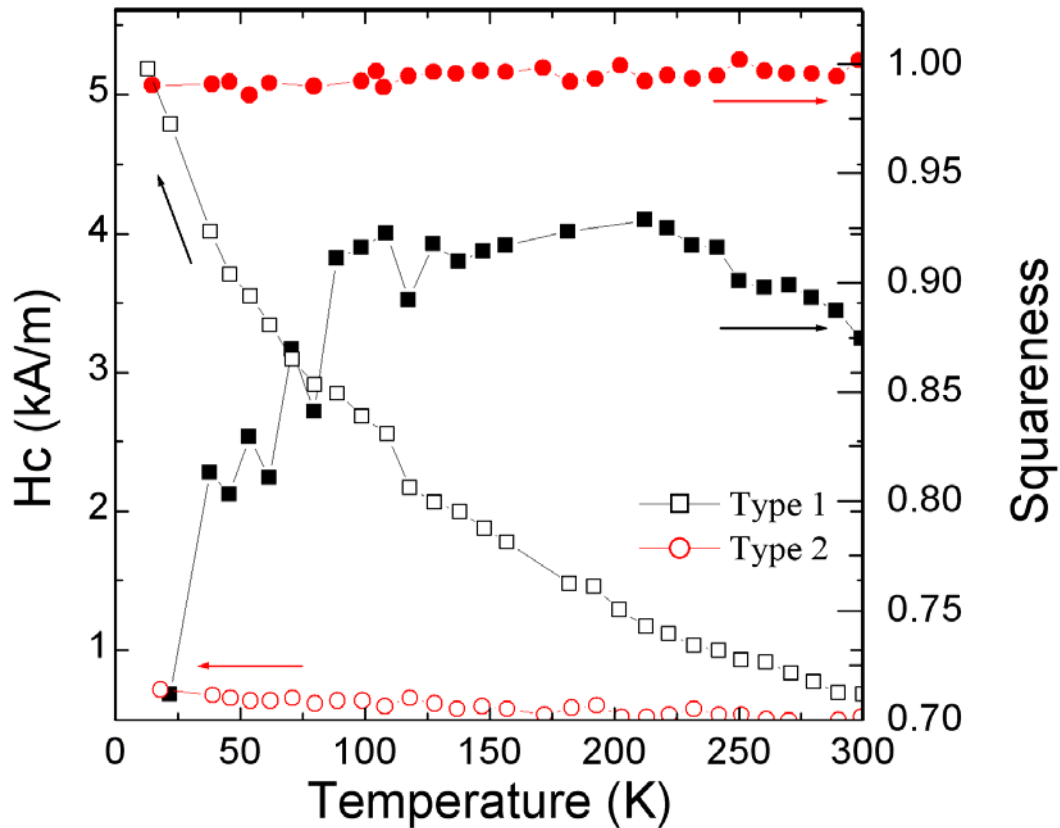


Fig. 4.3 The squareness (S) and hysteresis field (H_c) of type 1 and type 2 MTJs.

4.1.2. Voltage dependence of conductance

J-V curves were measured using a constant voltage source at 13 K (Fig. 4.4). The conductance G (V) curves were obtained by numerically dividing current by voltage. Both parallel and antiparallel configurations were measured at ± 20 kA/m for type 1 and ± 8 kA/m for type 2. Because the minimum of the G (V) curves has only a small offset

from zero bias, we choose the Brinkman-Dynes-Rowell model [4-6]. This model is given by

$$G(V) = \frac{I / Area_{junction}}{V} = G_0 \left[1 - \left(\frac{A_0 \Delta \phi}{16 \phi} \right)^{-3/2} (qV) + \left(\frac{9}{128} \frac{A_0^2}{\phi} \right) (qV)^2 \right],$$

where $\Delta \phi = \phi_2 - \phi_1$, $A_0 = \frac{4t\sqrt{2m}}{3\hbar}$ and $G_0 = \left(\frac{q^2}{t\hbar^2} \right) \sqrt{2qm\phi} \exp\left(-\frac{t\sqrt{8mq\phi}}{\hbar}\right)$ where t is the

barrier thickness in Å and ϕ is the potential in volts. By fitting the $G(V)$ curves measured at 13 K, we obtained the barrier parameters for two types of samples as shown in Table 4.1. The calculated barrier thickness of type 1 MTJ is larger than that of type 2 MTJ. The barrier height of type 2 MTJ is higher than that of the type 1 MTJ. The calculated barrier thickness of both types of samples is smaller than the starting Al layer thickness, 12 Å. These results indicate that both types of MTJ samples are likely to be either under-oxidized or dominated by thinner regions in the barrier that contribute most of the tunneling. The different values may relate to the different oxygen diffusion processes in these two types of MTJ samples when oxidizing the Al layer to the Al₂O₃ layer. And from the fitting, the barrier height indicates that the surface roughness in type 1 MTJ may be higher than that of type 2 MTJ samples.

Table 4.1 The fitting barrier parameters of type 1 and type 2 MTJ samples.

	t_P (Å)	ϕ_P (eV)	t_{AP} (Å)	ϕ_{AP} (eV)
Type 1	11.3	1.28	12.7	1.03
Type 2	6.7	3.46	7.2	3.28

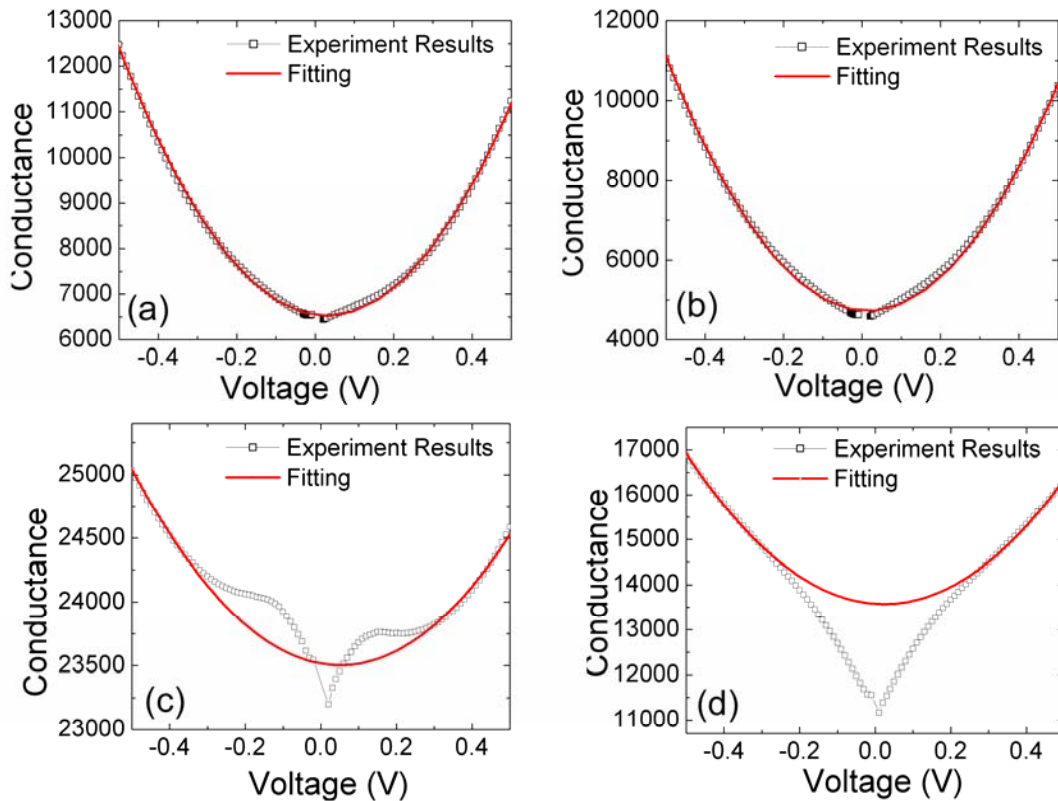


Fig. 4.4 Conductance versus bias voltage at 13 K for type 1 in the (a) P state and (b) AP state and for type 2 in the (c) P state and (d) AP state.

From the fitting curves, it can be seen that the model fits well for type 1 MTJ samples and only fits well in the range of -0.2 to -0.5 V and +0.2 to +0.5 V for type 2 MTJ samples. As the voltage increases, the conductance of type 2 MTJ samples has a rapid increase in the range of about 200 mV, and the increase is more pronounced for the AP alignment. The zero bias anomaly phenomena may be explained by hot electrons [7]. An electron with excess energy above the Fermi level is called a “hot electron”. With an applied bias voltage, those hot electrons will produce collective magnetic excitations of local interfaces between the insulating barrier and the ferromagnetic electrodes. The

emission of magnons at the interface accounts for the conductance increase as the applied voltage increases. However, we do not have experimental evidence that can clearly illustrate the above models. The observed zero bias anomaly in our type 2 MTJ samples is still not fully understood.

4.1.3 Temperature Dependence of Resistance

Fig. 4.5 shows the temperature dependence of RAP results for the two types of samples with a constant bias voltage of 10 mV. For type 1, from 300 K to 13 K, the resistance increases 45 % for the antiparallel state and increases 30 % for the parallel state. However, for type 2 it changes 31% for the antiparallel state, which is much more than the change of 10 % in the parallel state. The dependence of the resistance on temperature is usually explained by elastic and inelastic tunneling [8]. In this simple model, the temperature dependence of conductance for antiparallel and parallel states is

$$G_p = G_T [1 + P_1 P_2] + sT^{1.33}, \text{ and } G_{AP} = G_T [1 - P_1 P_2] + sT^{1.33}, \quad (4-1)$$

where $G_T = G_0 \frac{CT}{\sin(CT)}$, P_1 and P_2 are the effective tunneling electron spin polarizations of the two ferromagnetic electrodes, and $C = 1.387 \times 10^{-4} t / \sqrt{\phi}$, with the barrier thickness (t) in Å and the barrier height (ϕ) in eV. G_0 is the conductance of the MTJ at zero temperature. In equation (4-1), the first part

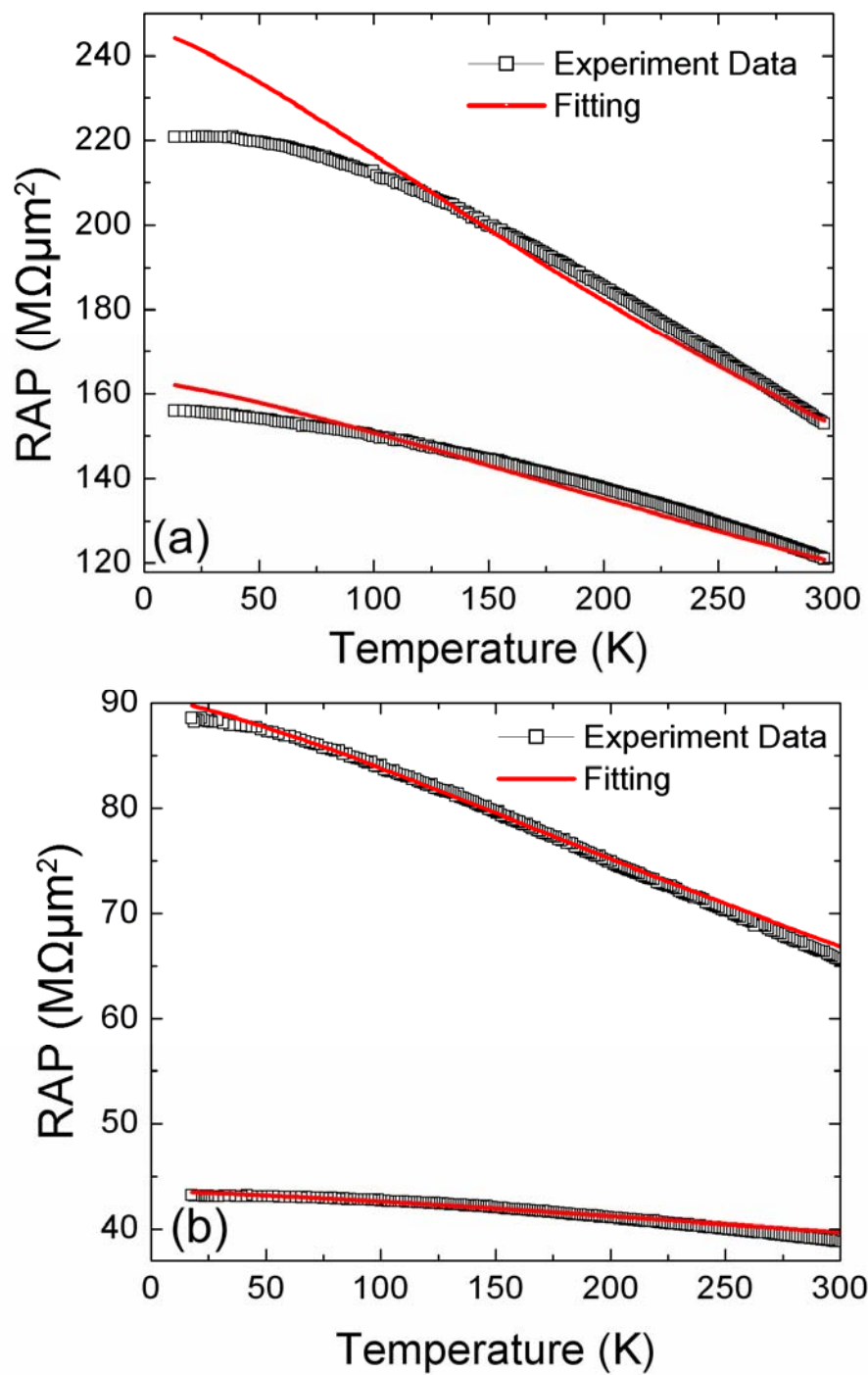


Fig. 4.5 Temperature dependence of the resistance-area product (RAP) in the P and AP states for (a) type 1 and (b) type 2 MTJs.

represents the elastic tunneling conductance, and the second part represents the inelastic one. It is assumed that the tunneling spin polarization follows the same temperature dependence as magnetization, Bloch $T^{3/2}$ law. This means the spin polarization at temperature T can be written as:

$$P(T) = P_0(1 - \alpha T^{3/2}) \quad (4-2).$$

The parameter P_0 is the polarization of the electrode at zero temperature. The constant α is a material-dependent constant. It describes the exchange coupling in the direction perpendicular to the surface. The parameter α is generally larger for the surface than the bulk due to surface exchange softening [9]. The parameter P_0 is sensitive to disorder and defects in the FM electrodes and FM/I interface. The disorder and defects could be due to interdiffusion at the interface, interface roughness, impurities, and grain boundaries, *etc.* And those nonmagnetic or paramagnetic disorders cause the total spin polarization in the free layer to decrease. Therefore with an increase in disorder, the spin polarization is reduced. From Eq. (4-1), as polarization increases, G_P increases, whereas G_{AP} decreases. Because the free layer and the pinned layer of type 2 MTJ samples are of the same material with similar thicknesses, and sputtered under similar conditions, we assumed they have same polarization P_0 and parameter α for fitting our experimental results. For the type 1 MTJ samples, the free layer and the pinned layers are of the same material, but have difference thicknesses, so we used different α and P_0 for the free layer and the pinned layer. In the fitting process for type 1 MTJ samples, we assumed that the polarization P_0 and parameter α of the pinned layer are the same as that of type 2 MTJ samples, since they are same material, same film thickness, and same fabrication conditions. In the Shang's model, the TMR increases only with decreasing temperature.

Our TMR data for type 1 MTJ samples show a maximum at about 70 K (Fig. 4.6), so we fit only the high temperature data using this model. The values of these parameters from the fitting are listed in Table 4.2.

Table 4.2. The fitting transport mechanisms and junction quality parameters.

	$G_0 (\Omega\mu\text{m}^2)^{-1}$	P_0	$\alpha (\text{K}^{-3/2})$	$s (\Omega\mu\text{m}^2)^{-1}\text{K}^{-4/3}$
Type 1	$5.1 * 10^{-9}$	34.5%,	$2.1 * 10^{-5}$	$1.1 * 10^{-12}$
Type 2	$1.7 * 10^{-8}$	59.1%,	$1.4 * 10^{-5}$	$1.5 * 10^{-12}$

By computing the TMR ratio by $((R_{AP} - R_P)/R_P)$, we obtained the temperature dependence of TMR ratio for type 1 and type 2 MTJs from 13 K to 300 K. Fig. 6 shows that the TMR ratio is around 26.3 % and 69.4% at room temperature for type 1 MTJ and type 2 MTJ, respectively. Before the temperature decreases to about 150 K, the TMR ratio of type 1 MTJ increases and follows the fitting curve well. As the temperature decreases more, the increase becomes much slower and gradually reaches a maximum of 42.7% at about 70 K before decreasing to 41.5 % at 13 K. This behavior of the TMR ratio decrease with decreasing temperature at low temperature was also reported by J. H. Lee *et. al.* on their over-oxidized MTJs [10]. The TMR ratio of the type 2 MTJ samples shows a monotonic increase with decreasing temperature. The highest TMR ratio for type 2 MTJ samples is 106.8% at 13 K.

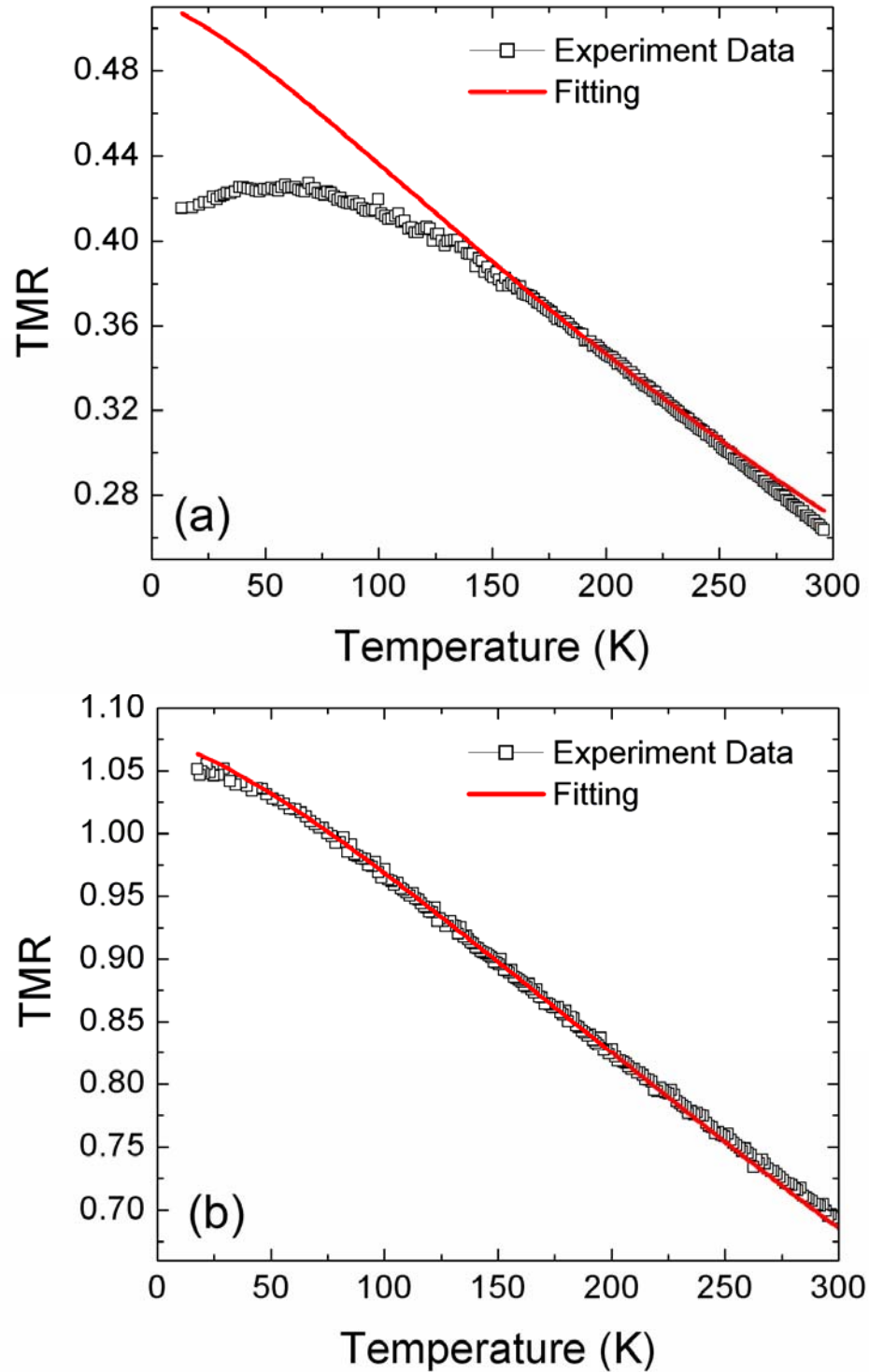


Fig. 4.6 Temperature dependence of TMR for (a) type 1 and (b) type 2 MTJs.

4.1.4. Temperature dependence of bias voltage dependence of magnetoresistance

Measurement of the voltage dependence of magnetoresistance at different temperatures is shown in Fig. 4.7. The figure shows a decreasing TMR ratio with increasing bias voltage for both types. This drop may be caused by inelastic scattering by magnon excitations at the ferromagnet/insulator interface which controls the voltage dependence [7]. $V_{1/2}$ (the bias voltage where the TMR ratio reaches half the zero-bias value) is 320 mV at room temperature and 300 mV at 13 K for type 1. For type 2 it is higher than 500 mV at room temperature and 450 mV at 13 K. V_{out} (defined as $V_{out} = V \times TMR$) is related to the highest signal output from a MTJ device, and it is an important parameter for device applications. The highest output which can be achieved, V_{max} , is 50 mV at 300 K and 70 mV at 13 K for type 1; while for type 2, V_{max} is higher than 205 mV at 300 K and higher than 256 mV at 18 K. From Table 1, we have shown that the barrier height of type 2 samples is much higher than that of type 1, while the barrier thickness of type 2 is much thinner than that of type 1. These results indicate that the samples with a higher barrier height have a higher $V_{1/2}$, while $V_{1/2}$ may not relate to the barrier thickness.

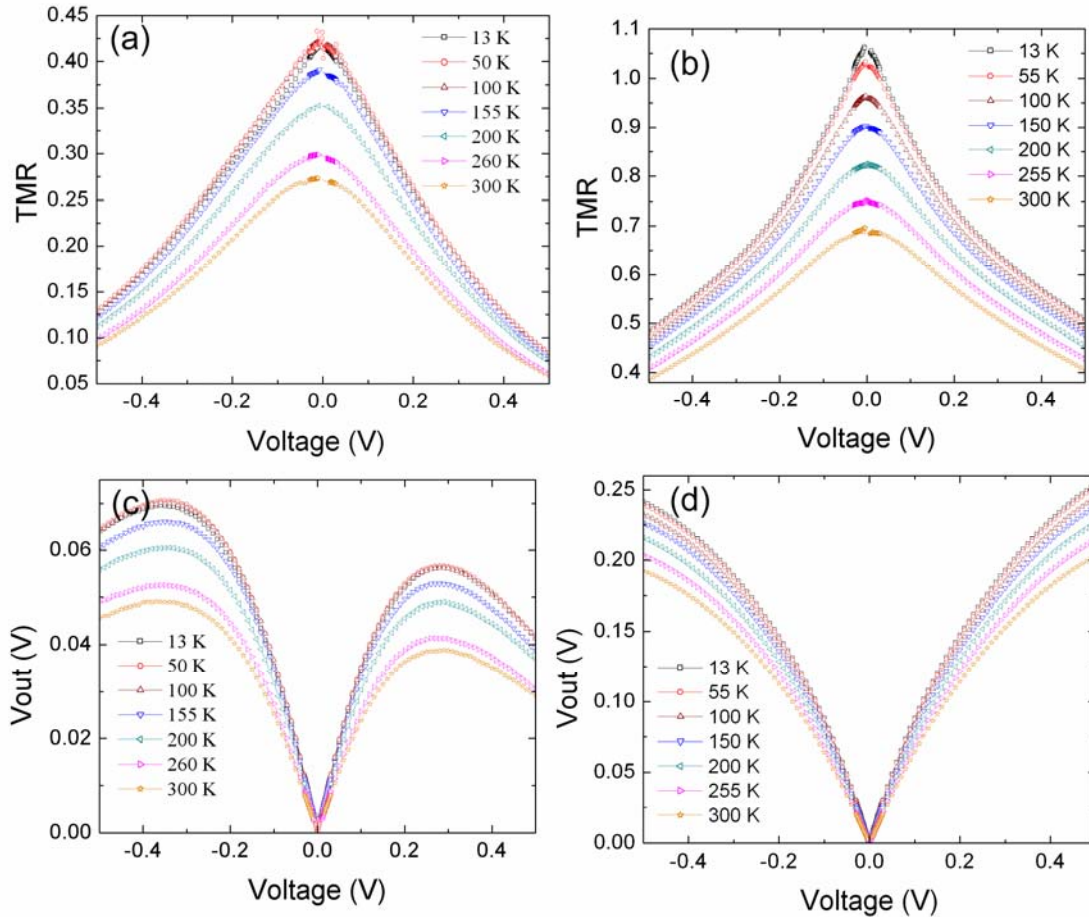


Fig. 4.7 Voltage dependence of TMR at different temperatures for (a) type 1 and (b) type 2 samples and voltage dependence of V_{out} (defined as $V \times TMR$) for (c) type 1 and (d) type 2 samples. The direction of bias voltage is defined with respect to upper electrode.

4.1.5 Discussion

From the MTJ layer structures, the main mechanisms that are responsible for the TMR behaviors should be related to the ferromagnetic layers, the barrier layer, and the two FM/I interface. We observed very different TMR ratios in the type 1 and type 2 MTJ samples. The TMR ratio is about 26% and 69% at room temperature for type 1 and type

2 MTJ, respectively. Since our two types of sample are different only in the free layer structures, the factors contributing to the magnetoresistance behavior changes should come mostly from the detailed magnetization orientation of free layer structures and/or the interface between the free layer and the insulating layer. From the analysis of our voltage and temperature dependence of resistance and magnetoresistance in these MTJs, we discuss the effects of magnetic behavior of the free layers, the interface between the free layer and the insulating layer, and barrier qualities.

The free layers of both types are made of the same material, but have different thicknesses. The thickness of the free layer is as thin as 8 Å for type 1, which corresponds to only a few monolayer. From previous studies, the films with thicknesses in this range may be superparamagnetic, nonmagnetic, or ferromagnetic [11-14]. The thin free layer of our type 1 MTJ samples is mostly ferromagnetic, which shows hysteresis. Since the free layer of type 1 is 5 times thinner than that of type 2. We would then expect there to be more defects in the free layer of type 1 than in that of type 2. The defects could cause incoherent nucleation, domain-wall pinning in the free layer and/or the interface between the free layer and the insulating layer. Evidence of the existence more magnetic inhomogeneous regions in the free magnetic layer and/or the interface between the free layer and the insulating layer of type 1 MTJ samples than in that of type2 can be illustrated by the temperature dependence of H_c , the squareness of the loop, the Néel coupling field, the temperature dependence of resistance in the P and AP states, the polarization of the electrode at the zero temperature P_0 , and the spin exchange stiffness constant α .

From Fig. 4.2, we observe the larger temperature variation of H_c and the lower S value in type 1 MTJ samples than that of type 2. This indicates that the magnetization of the free layer and/or the interface between the free layer and the insulating layer does not switch with the field as homogeneously as type 2 does. The Néel coupling field at 300 K for type 1 and type 2 MTJ are 5 Oe and 1.8 Oe, respectively. The small difference in Néel coupling field in these two types of samples is likely due to the different free layer structures, since the amplitude of the coupling field is related to the increase in magnetic roughness. The increase in the Néel coupling field in type 1 MTJ samples indicates the possibility that there is more magnetic roughness in type 1 MTJ samples than in that of type 2.

As shown in Fig. 4.5, the temperature dependence of resistance for type 1 MTJ samples in the AP state and in the P state increases 45 % and 30 %, respectively. The temperature dependence of resistance for type 2 MTJ samples in the AP state and in the P state increases 31 % and 10 %, respectively. The dependence of the resistance on temperature is usually explained by elastic and inelastic tunneling [9]. The increasing TMR ratio with decreasing temperature is caused by the fact that the increase in R_{AP} occurs more quickly than in R_P . This is because R_{AP} decreases while R_P increases with increasing temperature when there is magnetic disorder in the MTJ sample. Thermal assisted tunneling will decrease both R_{AP} and R_P with increasing temperature [15]. Due to a combination of these two effects, the increase of resistance in the AP state with decreasing temperature is more than that of the P state. The rate of decreasing TMR ratio is larger for type 1 MTJ samples than for type 2. The rate of decrease is calculated as follows: From Fig. 4.6, the TMR ratio is 26.3 % at room temperature and 42.7% at

about 70 K for type 1 MTJ samples (i.e. the TMR rate of change from 70 K to 300 K is 38%). The TMR ratio is 69.4% at room temperature and 98.7% at about 70 K for type 2 MTJ samples (i.e. the TMR ratio rate of change from 70 K to 300 K is 30%). The difference in the rate change of the TMR ratio implies that there are more spin disorders in the type 1 MTJ samples than in type 2.

The parameter P_0 is the spin polarization of the electrode at zero temperature. The fitting P_0 of type 1 MTJ samples is less than that of type 2 MTJ samples. The parameter P_0 is sensitive to disorder and defects in the FM electrodes and FM/I interface. A possible source of disorder and defects in the free layer is the interdiffusion between the bottom Ru and the CoFeB layer. The nonmagnetic Ru may cause a decrease in the spin polarization in the free layer. From Table 2, the P_0 of the type 2 MTJ samples is about 59.1 %, which is almost the maximum limit for the 3d magnetic material. This implies the spins in the free layer of type 2 MTJ samples are strongly coupled and well-aligned. Since the free layer thicknesses in the type 1 and type 2 MTJ samples are different, the type 2 MTJ samples may not be affected by this small interdiffusion at the bottom of the free layer. The constant α is a material-dependent constant which relates to the softening of the spin exchange coupling. The parameter α is generally larger for the surface than the bulk due to surface exchange softening [9]. From Table 4.2, the magnitude of α is $2.1 \cdot 10^{-5} \text{ K}^{-3/2}$ and $1.4 \cdot 10^{-5} \text{ K}^{-3/2}$ for type 1 and type 2 MTJ samples, respectively. The values have the same order of magnitude with most amorphous alloys. The fitting parameter α of type 1 MTJ samples is larger than that of type 2. This clearly indicates that the type 1 MTJ sample has more magnetic inhomogeneous regions than the type 2 MTJ sample. Those magnetic inhomogeneous distributions of local spins may be caused

by disorder or discontinuity as well as roughness in the thin free layer of type 1 MTJs. In addition, it may also be CoFeB isolated at the interface between the thin free layer of the type 1 sample and the Ru layer due to interdiffusion and/or Al₂O₃ layer due to partially oxidization.

From Fig. 4.3, we observe that the squareness (S) values of type 1 MTJ samples decrease rapidly at about 70 K while the S values of type 2 samples stay about the same. The reduction in S-value indicates that more magnetic pinning sites may exist in the type 1 MTJ at low temperature. This pinning may be due to additional magnetic components that occur at low temperatures or due to the temperature dependence of the magnetic anisotropy. This makes the whole CoFeB film difficult to align with the external field, especially at low temperatures. This may be explained by an existing spin-glass-like phase, which is hardly aligned below the spin freeze temperature. Incoherent spin rotations at low temperature increase the magnetic roughness in the free layer, which causes the H_c to increase and the Néel exchange coupling field of type 1 MTJ to increase with decreasing temperature.

Fig. 4.6 shows that there is a maximum at about 70 K in the TMR ratio versus temperature curve for type 1 MTJ samples. A possible reason for the maximum may be that spin-glass regions or inhomogeneous distribution of local spin in the free layer exhibits spin reorientation with changing temperature. When the temperature is higher than the spin freeze temperature, those regions act paramagnetically and the magnetization will decrease as temperature increases. If the sample is cooled below the spin freeze temperature, the magnetization will be frozen randomly and the average magnetization will be reduced with decreasing temperature. At low temperature, the total

effect of both the spin-glass-like regions and the ferromagnetic regions may result in increasing the spin polarization of the whole free layer, P_1 , with increasing temperature.

From equation (4-1), we can express the TMR as

$$TMR = \frac{1}{(1 + sT^{1.33}) / P_1 P_2 - 1}.$$

If the increase in P_1 is large enough to make the increase in the product $P_1 P_2$ larger than the increase in $1 + sT^{1.33}$, then the TMR will increase with a temperature increase. When the temperature is higher than the spin freeze temperature, both magnetic disorder and the spin glass cause the decrease in the spin polarization. This causes the resistance decrease in the AP state to be more than in the P state with a temperature increase, resulting in a TMR decrease.

The barrier quality can be revealed by the study of the temperature dependence of resistance of both types of samples. The fitting parameter s (in Eq. (4-1)) describes the temperature dependence of the spin-independent conductance. Some mechanisms may cause the spin-independent conductance. Among them, the most important two are hopping conductance due to imperfections in the barrier and pinholes in the barrier layer. The two types of samples have similar small value of s [6, 16], which indicates both types of samples have a clean interface between FM/I interface.

4.2 Effect of magnetic state in pinned layer

4.2.1 Major loop change with saturation field

To study the effect of microstructure in the pinned layer on the TMR behavior, we applied a magnetic field to tune the magnetization states in the pinned layer without changing the physical structure of the MTJ samples under ambient conditions. As shown

in Fig. 4.8, the magnetoresistance (MR) loops are measured with applied magnetic field from -605 kA/m (-7.6 kOe) to 119 kA/m (1.5 kOe) and back to -605 kA/m (-7.6 kOe). The measured major loops show similar behavior for the two types of MTJ samples. The MR results are analysed in three field ranges.

In the field range from -605 kA/m to -119 kA/m , the MR stays in the low resistance state. The large field overcomes the exchange coupling and causes the reference layer (50\AA CoFeB) in the SAF structures rotate to align with the applied field. Therefore the magnetization of the free layer and pinned layer are parallel aligned (as shown in inset I in Fig 4.8).

In the field range from -119 kA/m to 24 kA/m (300 Oe), the resistance increases to a maximum ($430 \text{ k}\Omega$) and then decrease sharply to $334 \text{ k}\Omega$ with field increases. These external fields is not large enough to overcome the antiparallel coupling in the SAF, so FeCo and CoFeB layers are antiparallel aligned. Then the change of MR in this range is mostly due to the magnetization of the free layer switching with the applied field (as shown in inset II in Fig 4.8).

In the field range from 24 kA/m to 119 kA/m , the resistance of the MTJ reaches a local maximum at 44.6 kA/m (560 Oe) and then decreases. In this field range, the magnetization of the free layer is already saturated, so the change in MR indicates that the magnetization of the pinned layer changes with applied field. That may be explained by the generated domains in the CoFe layer due to the competition between the external field and the coupling with the AFM layer. Because of the strong coupling with CoFe layer, the reference layer has correlated domains. The change of the total magnetization of all these domains with applied field causes the MR changes (as shown in inset III in

Fig 4.8).

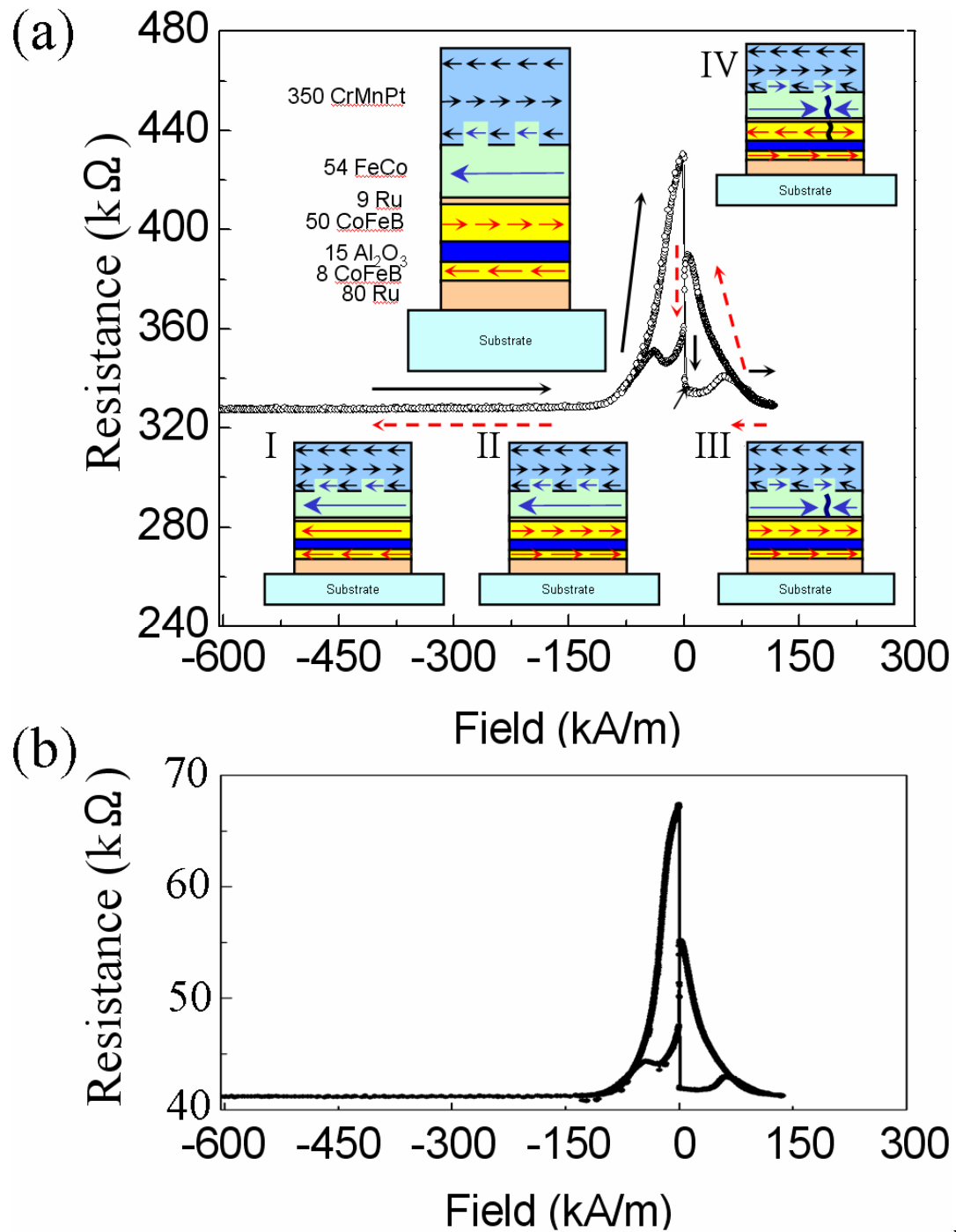


Fig. 4.8 The magnetoresistance (MR) loops for (a) type 1 and (b) type 2 MTJ samples. The insets of Fig. 4.8 (a) show the layer structure and magnetization of each layer of the MTJ at various magnetic fields.

As field is swept down from 119 kA/m, the resistance monotonically increases and reaches a maximum (389 k Ω). But it is smaller than the 430 k Ω obtained at 6.2 kA/m (78 Oe). That may be explained by the some regions in the interface of the CrMnPt/CoFe being weakly coupled with the bulk AFM layer. When the field decreases from the maximum reversed field, the magnetization of these regions does not totally switch back ((as shown in inset IV in Fig 4.8).). That may causes domain walls in the CoFe layer due to the exchange coupling with these defect regions. And then, the exchange coupling between the CoFe and CoFeB layer make the reference forms domain walls. Because the resistance of the junction depends on the relative magnetization orientation between the free layer and the reference layer. These domains in the reference layer will decrease the R_{AP} .

4.2.2 Minor loop change with reversal field

Minor loop measures the resistance change under a small magnetic field that only changes the magnetization of the free layer. The magnetization of the reference layer is not changed much under such small magnetic field. Also the magnetoresistance of the MTJs is related to the relative magnetization orientation between the free and the reference layer. Then with the same free layer, the minor loop indicates the magnetization in the reference layer. The minor loops of the MTJs are measured after swept the field from -605 kA/m to a reversal field and back to zero fields (Fig. 4.9). The reversal field is defined as the large positive field applied. For example, in Fig. 4.8, the reversal field is 119 kA/m. For type 1 samples, with applied the reversal field as 62 kA/m (780 Oe), the R_{AP} is 419 k Ω and R_P is 337 k Ω . With the reversal field increases to 119 kA/m, the minor loop of the type 1 MTJs changes directions from the previous case and

the center of the MR loop shift to positive field. Also the R_{AP} decreases to 391 k Ω and R_P increases to 348 k Ω . As the reversal field is further increases to 605 kA/m, the R_{AP} increases to 412 k Ω and R_P decreases to 339 k Ω . For type 2, with applied the same reversal fields as type 1, the R_{AP} and R_P show same trend. As the reversal field increases from 62 kA/m to 119 kA/m, R_{AP} decreases and R_P increases. And R_{AP} increases and R_P decreases when the saturation field goes up to 605 kA/m.

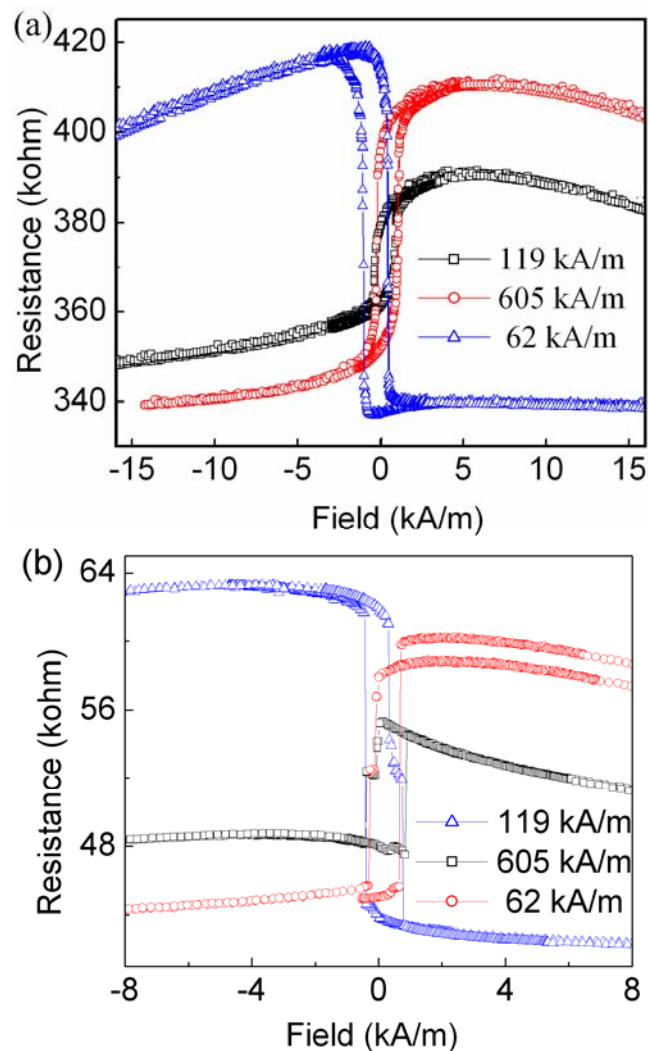


Fig. 4.9 Minor magnetoresistance loops for (a) type 1 and (b) type 2 MTJs for different applied reversal fields.

Fig. 4.10 shows the R_{AP} and R_P of the minor loops as the applied reversal field

ranges from 0 kA/m to 605 kA/m. For type 1 MTJs, R_P increases with saturation field, reaches a maximum at a reversal field of 98 kA/m (1.23 kOe) and then decreases; R_{AP} decreases with increasing reversal field and reaches a minimum at a saturation field of 98 kA/m and then increases. For type 2 MTJs, the R_{AP} (R_P) get maximum (minimum) also at 98 kA/m.

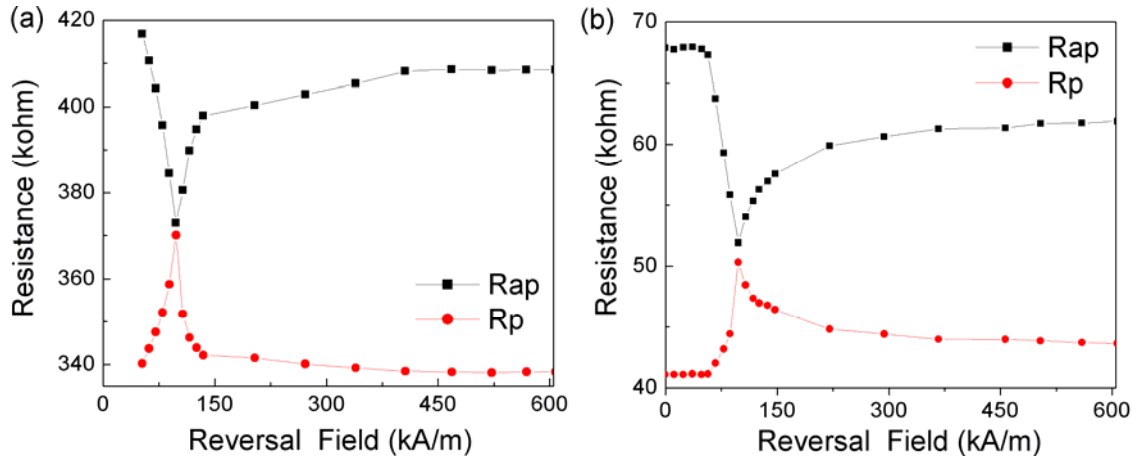


Fig. 4.10 R_{AP} and R_P of the minor loops for (a) type 1 and (b) type 2 MTJs for different applied reversal fields.

Fig. 4.11 shows the TMR of the minor loop calculated from R_{AP} and R_P in Fig. 4.10. The TMR of both types of MTJs gets minimum at 98 kA/m. While the TMR of type 1 at 56 kA/m (700 Oe) reversal field is 20% and at 605 kA/m (7.6 kOe) reversal field is 19.1%, the difference is 0.9%. While for type 2 MTJs, the TMR at 56 kA/m is 65% and at 605 kA/m is 39.7%. The difference is 25.3%, which is much higher than type 1 MTJs.

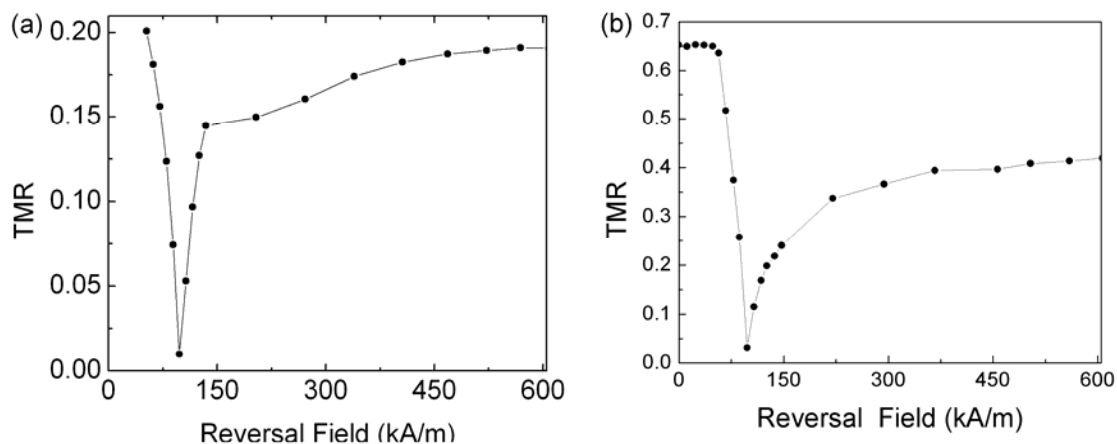


Fig. 4.11 TMR of the minor loops for (a) type 1 and (b) type 2 MTJs for different applied reversal fields.

H_E of the minor loop after applying a reversal large magnetic field as shown in Fig. 4.12. The H_E changes from negative field to positive field and reaches zero at about 98 kA/m. The coercivity field of the minor loop after applying a reversal magnetic field as shown in Fig. 4.13. The H_C shows small variation after applying different reversal fields.

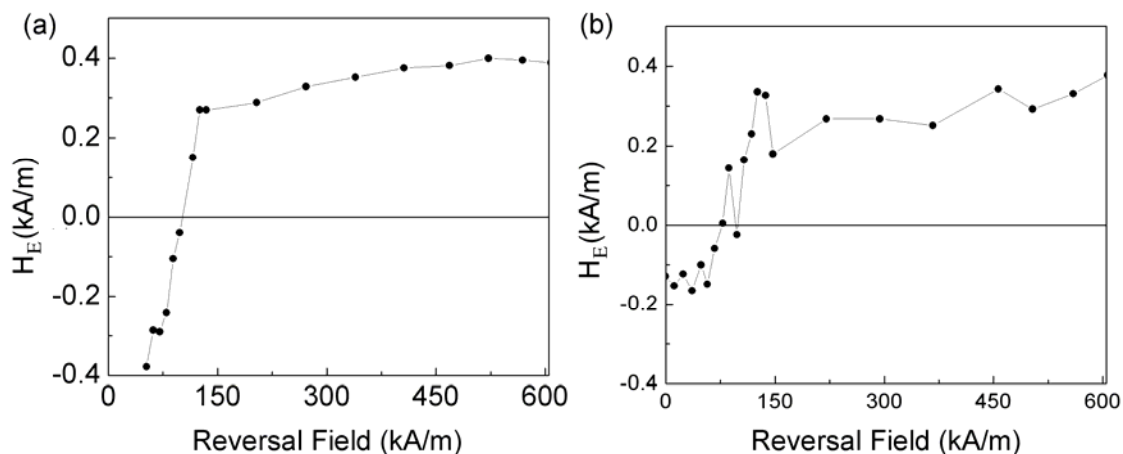


Fig. 4.12 H_E of the minor loops for (a) type 1 and (b) type 2 MTJs for different applied reversal fields.

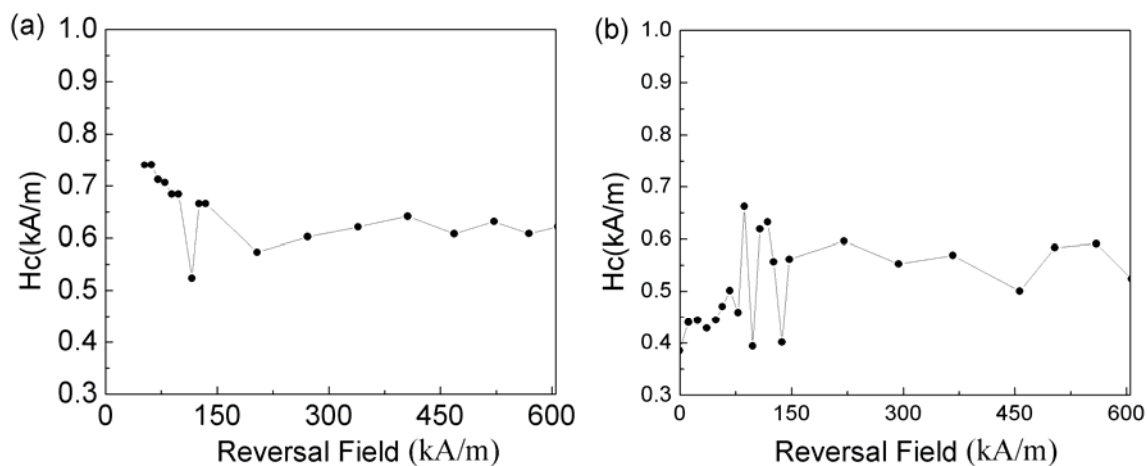


Fig. 4.13 H_c of the minor loops for (a) type 1 and (b) type 2 MTJs for different applied reversal fields.

4.2.3 Discussion

For type 1 MTJs, both the TMR and H_E have minimum absolute values after applying about 98 kA/m reversal field. At the point, the two ferromagnetic layers of the artificial antiferromagnetic layers may form a lot of domains due to the competence between the exchange coupling and the applied field. The magnetization of these domains may be canceled out, which causes the TMR to drop to about zero. Also, H_E is usually caused by Neel coupling and/or the stray field that comes out from the pinned layer. Neel coupling is also called “orange peel“ coupling, which is caused by the magnetostatic interactions between the free poles at the two ferromagnetic interface next to the nonmagnetic barrier in a MTJ [1, 16]. The Neel coupling is related to the roughness of the interface between the two ferromagnetic interface adjacent to the barrier layer. It is larger for the rougher interface. The MTJ we measured has a well defined and smooth layer interface, so the change in H_E is likely due to the decreasing stray field at

the edges. If the two ferromagnetic layers in the SAF layer structure are perfectly coupled, no stray field comes out from the SAF layer structure to affect the free layer. However, there is always some small amount of stray field comes out from the SAF layer structures due to the imbalanced coupling between the two ferromagnetic layers. The stray field at the edge will be reduced due to the multi-domain formation in the ferromagnetic (FM) layers of the SAF structures.

Under the same applied reversal field, the major loops of the type 2 MTJs show minimum and maximum resistance at about same field as type 1 MTJ. Under large magnetic field, magnetization microstructures are generated in the pinned layer structure, while the behavior of the free layer is not changed. Since the pinned layer structures are same for type 1 and type 2 samples, similar magnetic state behavior in the pinned layers is expected for type 2.

4.3. Summary

The voltage and temperature dependence of resistance and magnetoresistance of two types of MTJs are studied. These two types of MTJ samples have different free layer structures but the same pinned structures and the same material for free and reference layers. We observed quite different TMR ratios for these two types of samples. For type 2 MTJs, a TMR ratio as high as 107% is detected at 13 K. To our knowledge, this is the highest value that has been reported in the MTJ with an Al_2O_3 barrier. We discuss the effects of magnetic behavior of the free layers, barrier qualities, and barrier interfaces.

From the analysis of our results, we conclude that: (1) There are more magnetic inhomogeneous regions in the free magnetic layer and/or at the interface between the free layer and the insulating layer of type 1 MTJ samples than in of type 2 MTJ samples;

(2) There are possible additional spin-glass-like states that occur at the interface between the free layer and the insulating layer in the type 1 MTJ sample at low temperature; (3) Type 2 MTJ samples have thinner barrier thickness, higher barrier potentials and higher output V_{\max} than the type 1 MTJ samples. These results clearly indicate that the micro-magnetization orientation in the free layer and the FM/I interface play an important role in determining the TMR ratio in these two types of MTJ samples.

The magnetization of the SAF pinned layer structures is changed by applied field. For both types of samples, the TMR and H_E of the minor loops versus applied reversal field have a minimum. The reversal magnetic field corresponding to the minimum is about the same for both types of samples. The change in R_P , R_{AP} , TMR, and H_E of the minor loops after applied different applied reversal fields may be explained by the domains formation in the reference layer. The magnetic inhomogeneity may originate at the interface between AFM/FM layers. Due to the exchange coupling, domains are formed in the FM layer adjacent to the AFM layer. And the exchange coupling between the SAF structures cause the domain formation in the reference layer.

References:

1. Dexin Wang, Dames M. Daughton, Zhenghong Qian, Cathy Nordman, Mark Tondra and Art Phom, "Spin dependent tunneling junctions with reduced Neel coupling", *J. Appl. Phys.*, **93**, 8558 (2003).
2. B. D. Schrag, A. Anguelouch, S. Ingvarsson, Gang Xiao, Yu Lu, P. L. Trouilloud, A. Gupta, R. A. Wanner, W. J. Gallagher, P. M. Rice, and S. S. P. Parkin, "Neel "orange-peel" coupling in magnetic tunneling junction devices", *Appl. Phys. Lett.*, **77** 2373 (2000).
3. John G. Simmons, "Generalized thermal J-V characteristic for electric tunnel effect", *J. Appl. Phys.*, **35**, 2655 (1964).
4. W. F. Brinkman, R. C. Dynes, and J. M. Rowell, *J. Appl. Phys.*, **41**, 1915 (1970).
5. Bryan Oliver and Janusz Nowak, "Tunneling conductance of asymmetrical barriers", "Temperature and bias dependence of dynamic conductance-low resistive magnetic tunnel junctions", *J. Appl. Phys.*, **95**, 546 (2004).
6. S. Zhang, P. M. Levy, A. C. Marley, and S. S. P. Parkin, "Quenching of magnetoresistance by hot electrons in magnetic tunnel junctions", *Phys. Rev. Lett.*, **79**, 3744 (1997).
7. Chang He Shang, Janusz Nowak, Ronnie Jansen, and Jagadeesh S. Moodera, "Temperature dependence of magnetoresistance and surface magnetization in ferromagnetic tunnel junctions", *Phys. Rev. B.*, **58**, R2917 (1998).
8. D. Mauri, D. Scholl, H. C. Siegmann, and E. Kay, "Observation of the exchange interaction at the surface of a ferromagnet", *Phys. Rev. Lett.* **61**, 758 (1998).
9. J. H. Lee, K. I. Lee., W. L. Lee, K. H. Shin, J. S. Lee, K. Phie, and B. C. Lee,

- “Temperature dependence of tunneling magnetoresistance: Double-barrier versus single-barrier junctions”, *J. Appl. Phys.*, **91**, 7956 (2002); K. I. Lee, J. H. Lee, W. L. Lee, K. H. Shin, Y. B. Sung, J. G. Ha, K. Rhie, and B. C. Lee, “Temperature dependence of magnetoresistance for tunnel junctions with high-power plasma-oxidized barriers: Effects of annealing”, *J. Appl. Phys.*, **91**, 7959 (2002).
10. D. Wang, J. M. Daughton, K. Bussmann, and G. A. Prinz, “Magnetic properties of very thin single and multilayer NiFeCo and CoFe films deposited by sputtering”, *J. Appl. Phys.* **83**, 7034 (1998).
 11. R. Schad, H. Alouach, J. W. Harrell, M. Shamsuzzoha, and D. Wang, “Superparamagnetic NiFeCo layers as free layers in magnetic tunnel junctions”, *J. Appl. Phys.* **93**, 8561 (2003).
 12. C. -Y. Hung, M. Mao, S. Funada, T. Schneider, L. Miloslavsky, M. Miller, C. Qian, and H. C. Tong, “Magnetic properties of ultrathin NiFe and CoFe films”, *J. Appl. Phys.* **87**, 6618 (2000).
 13. Y. Luo, M. Esseling, A. Käufler, K. Samwer, T. Dimopoulos, G. Gieres, M. Vieth, M. Rührig, J. Wecker, C. Rudolf, T. Niermann, and M. Seibt, “Co-rich magnetic amorphous films and their application in magnetoelectronics”, *Phys. Rev. B* **72**, 14426 (2005).
 14. Stuart S. P. Parkin, Christian Kaiser, Alex Panchula, Philip M. Rice, Brian Hughes, Mahesh Smant, and See-Hun Yang, “Giant tunneling magnetoresistance at room temperature with MgO (100) tunnel barriers”, *Nature* **3**, 862 (2004).
 15. T. Hagler, R. Kinder, and G. Bayreuther, “Temperature dependence of tunnel magnetoresistance”, *J. Appl. Phys.*, **89**, 7570 (2001).

16. L. Neel, *Comptes Rendus Acad. Sci., Paris*, **255**, 1676 (1962).

Chapter 5

Variable temperature and ultra-high vacuum microcantilever torque magnetometry (MTM) for studying magnetic nanostructures

As the size of the magnetic sensors shrinks to sub-micrometer size, the study of small, defined magnetic structures has attracted much attention due to interest in both technological applications and fundamental research in micromagnetism [1-3]. Microcantilever torque magnetometry (MTM) is a promising new experimental technique for measuring such small magnetic features due to its high sensitivity [4-11]. In this work, we develop a variable temperature MTM system that can be operated under an ultra-high vacuum for the study of magnetic nanostructures.

5.1 Microcantilever torque magnetometry (MTM)

The characterization of thin magnetic films, patterned recording media, and nanometer-scale magnetic sensors is challenge for conventional magnetometers. Conventional magnetometers are designed for measuring specimens with millimeter dimensions. Therefore they have low signal-to-noise ratio (SNR) for small specimens. This is often solved by measuring a collection of small samples, but then the measurement gives number of average of a large amount of similar structures. The ultra-high sensitive MTM can be good candidate for characterizing *single* micrometer sized element.

Torque measurements require a magnetic torque on a sample to active the cantilever vibration. The amplitude of this vibration is proportional to the magnetization in the sample. The force resolution achievable for a freely vibration cantilever is limited

by the thermomechanical noise in the mechanical system. The minimum detectable force can be described as

$$\Delta F_{\min} = \sqrt{\frac{4kk_B TB}{\omega_0 Q}} \quad (5-1)$$

where k is the spring constant, k_B is the Boltzmann constant, T is the temperature, B is the bandwidth, ω_0 is the resonance frequency, and Q is the quality factor [12]. So the force sensitivity of the MTM can be improved by lowering the spring constant k , increasing the resonance frequency ω_0 , and increasing quality factor. For a rectangular cantilever the resonance frequency ω_0 and spring constant k can be expressed as

$$\omega_0 \propto \sqrt{\frac{E}{\rho}} \frac{t}{l^2} \quad \text{and} \quad k \propto \frac{Et^3 w}{4l^3}$$

where E is Young's module, t , w , and l are thickness, width and length of the cantilever, and ρ is the mass density. So the easy way to reduce the spring constant is to decrease the cantilever thickness. However, due to the practical limitations, the cantilever must be of a certain thickness to provide sufficiently sturdy design. Also the quality factor Q decreases proportionally to the cantilever thickness. As the thickness decreases, the surface-to-volume ratio increases, and the surface loss becomes dominant in a thinner cantilever. Then to achieve small k , large ω_0 , and keep Q , we can decrease all the dimensions of the cantilever. Also the quality factor can be improved by cleaning the cantilever and modifying the surface stress by annealing at 1000 °C [13].

The sensitivity of the MTM is not only dependent on the cantilever itself but also dependent on the measurement environment. From equation (5-1), the minimum detectable force is proportional to the temperature. So the resolution increases as the temperature decreases. Also the measurement done under higher vacuum can help

eliminate contaminated adsorption such as water molecules [14-17].

In this work, we develop a MTM system, which can be operated in the temperature range from 10 K to 300K and in vacuums up to 10^{-8} torr. Fig. 5.1 shows the measurement of the resonance frequency for a cantilever with 95 A/m (1.2 Oe) torque field and no applied magnetic field in the sample plane. The signal amplitude at ambient conditions is 0.79 mV. With temperature decreases to 136 K under vacuum of 1×10^{-6} torr, the signal amplitude further increase to 8.3 mV. The signal increases about 1 order with temperature decreases. At room temperature, with the vacuum to 5×10^{-7} torr, the signal amplitude at the resonance frequency increases to 28.1mV. The signal amplitude increases about 2 orders. We expect the signal amplitude increase at least 3 orders under both low temperature at 10 K and high vacuum of 10^{-8} torr.

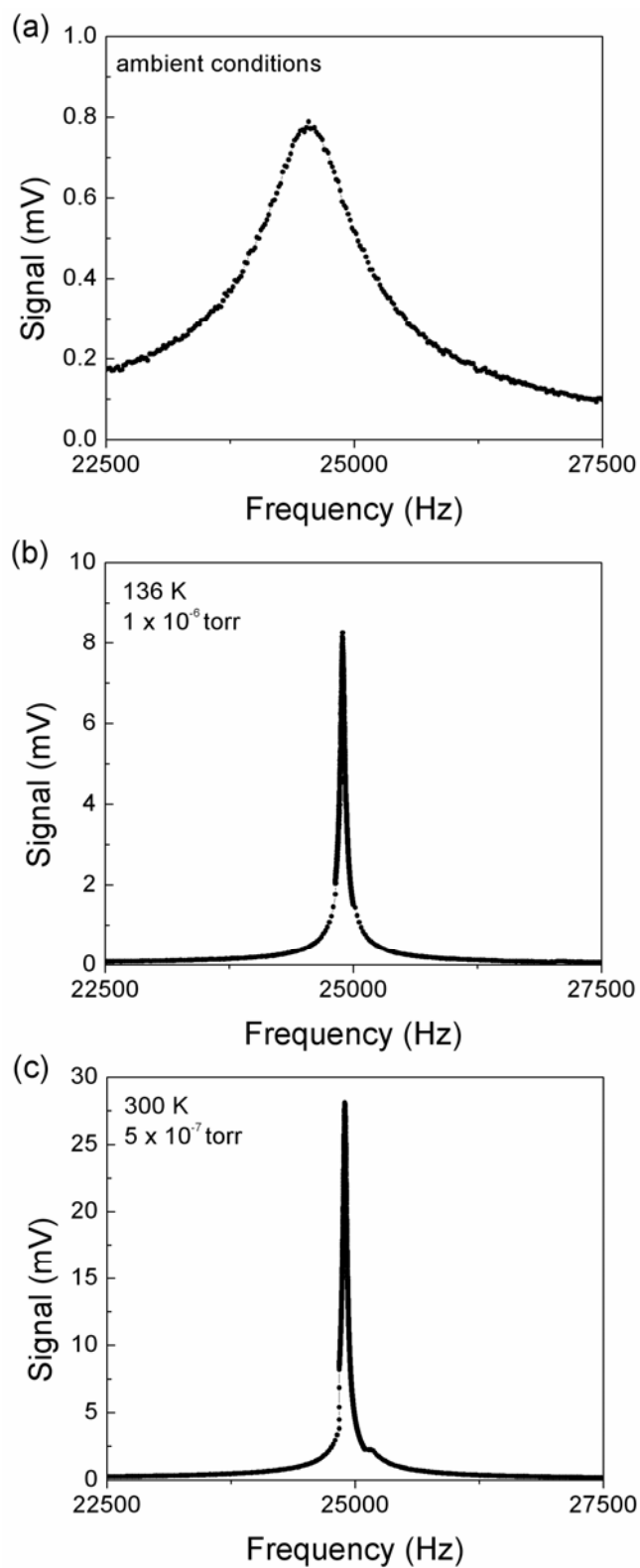


Fig. 5.1 The resonance frequency measurement of the same cantilever under (a) ambient conditions, (b) 136 K and 1×10^{-6} torr and (c) 300 K and 5×10^{-7} torr.

5.2 Fabrication of the magnetic patterned films on cantilevers

A new fabrication process is developed to put magnetic patterned films on cantilevers as shown in Fig. 5.2. First, a thick gold layer (about 200 nm) has been deposited on clean Si substrates or Si cantilevers. Then we use the focused ion beam (FIB) to pattern the nanostructures on the sample. The magnetic film is deposited on the cantilever samples with a well aligned collimator and a slow depositing rate. Finally, a lift-out process that uses a gold etchant is used to remove the gold layer and deposited film layers. Only the pattern is left on the substrate or the cantilever. The advantage of this nanofabrication is that any kinds of patterns can be easily patterned by using FIB milling. This new process avoids the PMMA spin coating step. That prevents to damage cantilevers during the patterning process.

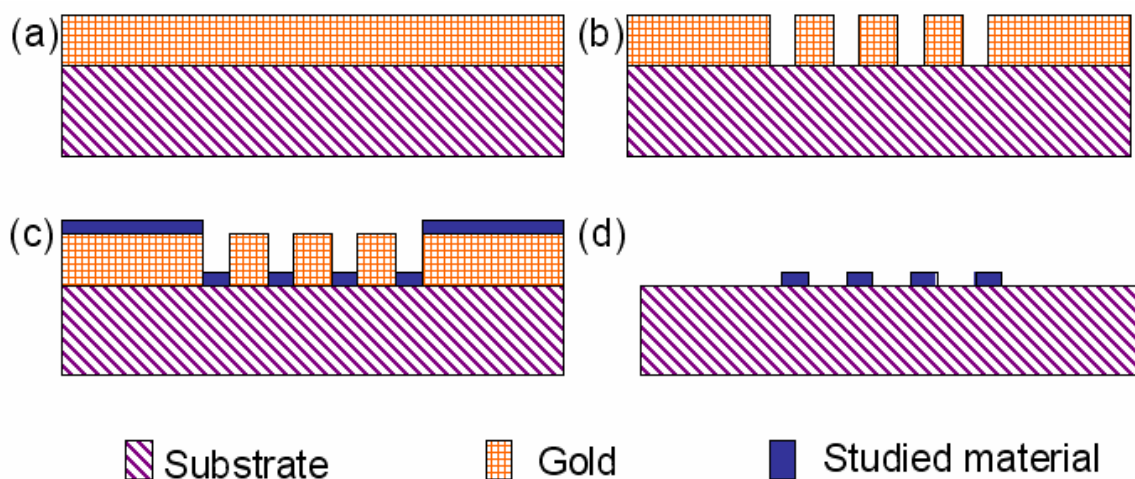


Fig. 5.2 Schematic diagram of the fabrication process of sample on the microcantilever.

Fig. 5.3 shows some examples of a patterned cantilever with 100 $\text{Ni}_{80}\text{Fe}_{20}$ dots using the newly developed process. Fig. 5.3 (b) shows the dots with 1 μm diameter and a

center-to-center distance of 4 μm . Fig. 5.3 (c) shows enlarged patterned dots with diameter of 500 nm and a center-to-center distance of 2 μm .

The magnetic hysteresis loops of the patterned dots arrays are measured by MTM at ambient conditions. Fig. 5.4 (a) shows the measured hysteresis loop for dot array with diameter of 1 μm and center-to-center distance of 4 μm . The magnetization of the dots is first saturated to form a single domain state at a magnetic field of + 100 kA/m. When the magnetic field decreases to +26 kA/m, the magnetization shows a sharp decrease. This jump corresponds to an irreversible transition to a vortex state. With decreasing field, the magnetization gradually decreases, that relates to the vortex being smoothly pushed out until it forms single domain state again at - 43 kA/m. Fig. 5.4 (b) shows the measured hysteresis loop for dot array with diameter of 500 nm and center-to-center distance of 2 μm . The vortex state is formed at 26 kA/m, and the single domain state happens at -49 kA/m.

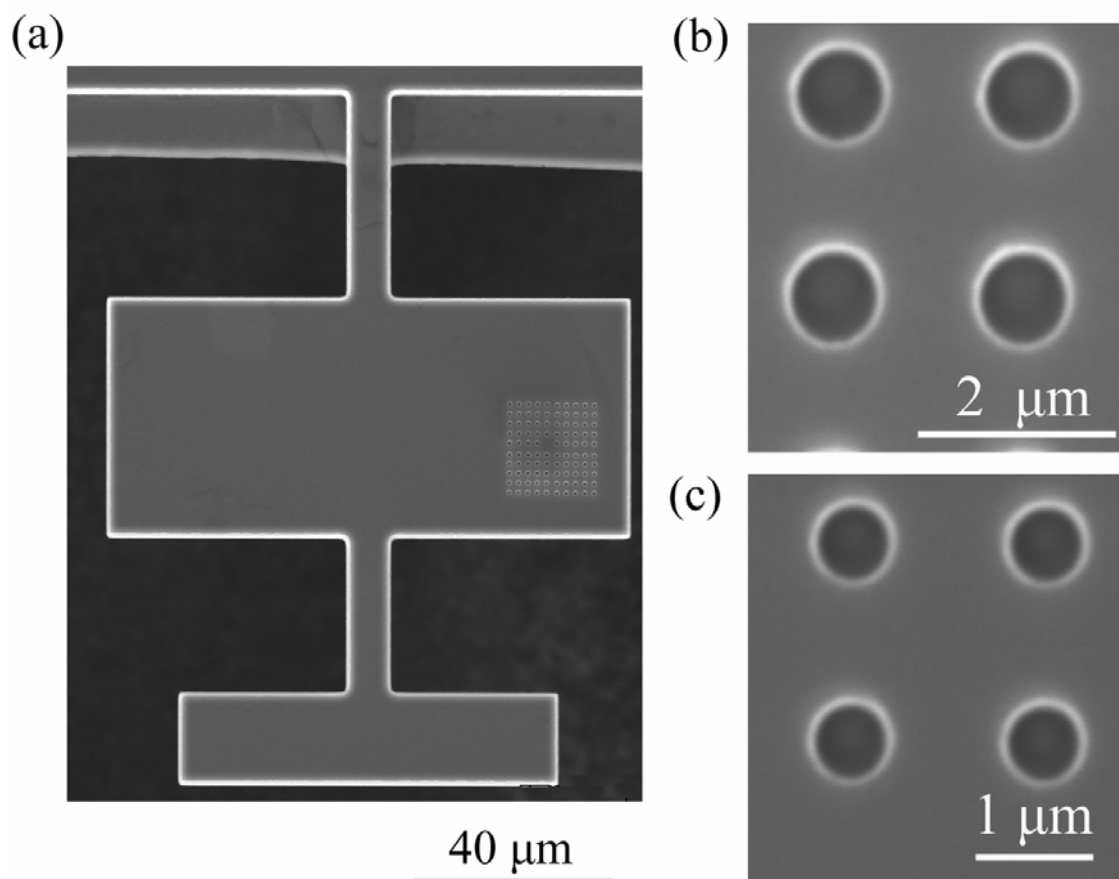


Fig.5.3 SEM image of the cantilever (a) with 100 50nm-thick $\text{Ni}_{80}\text{Fe}_{20}$ dots array; (b) enlarged patterned dots with a diameter of 500 nm and center-to-center distance of 2 μm ; and (c) enlarged patterned dots with a diameter of 1 μm and the center-to-center distance is 4 μm .

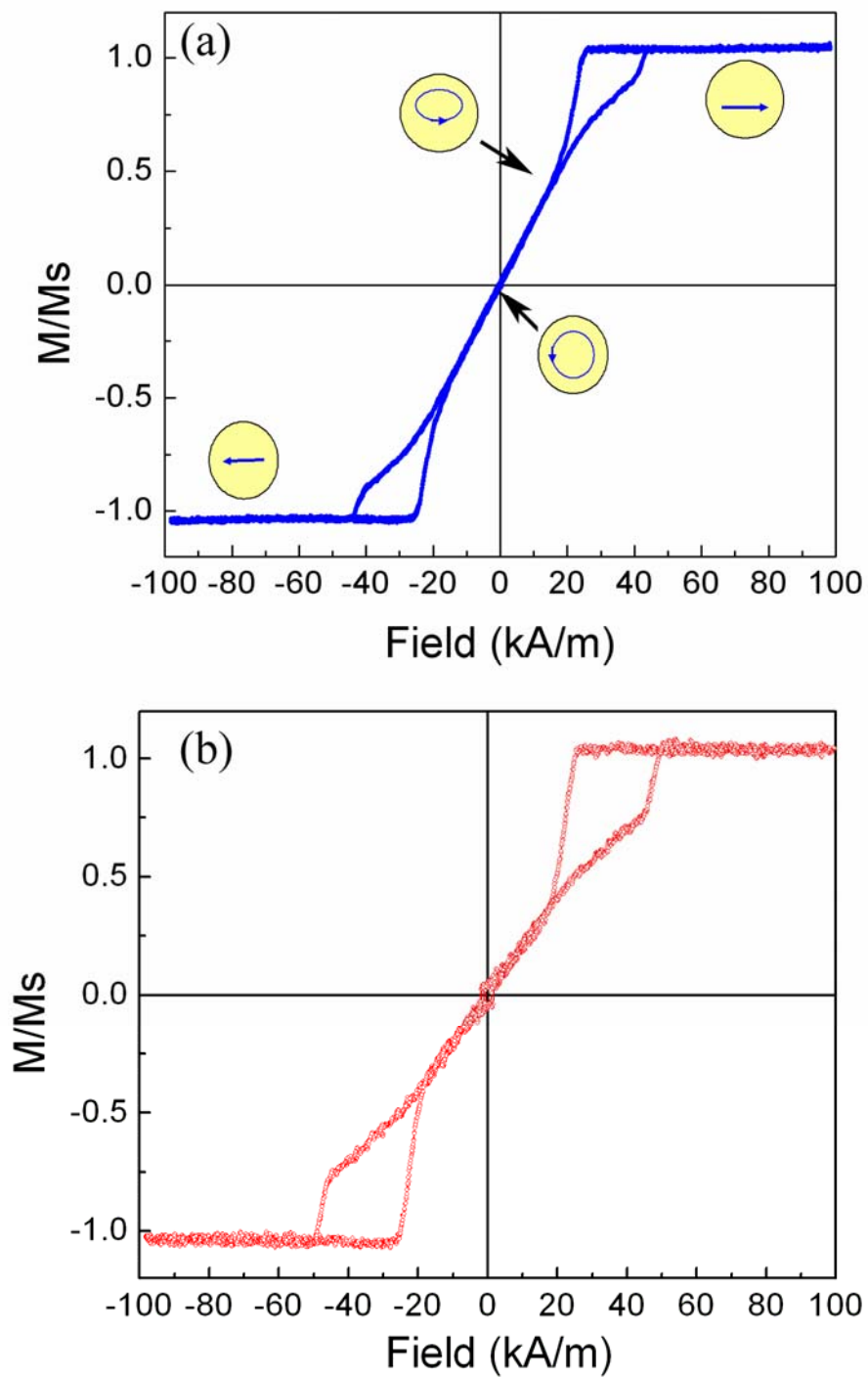


Fig. 5.4 The hysteresis loops for 100 50nm-thick $\text{Ni}_{80}\text{Fe}_{20}$ dots array with (a) with a diameter of 1 μm and the center-to-center distance is 4 μm ; and (b) a diameter of 500 nm and center-to-center distance of 2 μm .

5.3 Single and paired bar measured at ambient conditions

In order to investigate the magnetic interaction between a pair of bars, a $7\ \mu\text{m} \times 7\ \mu\text{m} \times 30\ \text{nm}$ $\text{Ni}_{80}\text{Fe}_{20}$ film was put on the top left corner of the cantilever [Fig. 5.5 (a)] [18]. A 30 nm thick Al layer was deposited on the top of the $\text{Ni}_{80}\text{Fe}_{20}$ film that prevents the possible poisoning of the magnetization with the Gallium ions. An enlarged picture of the patterned $\text{Ni}_{80}\text{Fe}_{20}$ film is shown in Fig. 5.5 (b). The $\text{Ni}_{80}\text{Fe}_{20}$ film was then patterned into two single $7\ \mu\text{m} \times 3.5\ \mu\text{m} \times 30\ \text{nm}$ bars by cutting a 60 nm gap in the center of the film using a FIB [Fig. 5.5 (c)]. The cut is made about 200 nm deep to ensure the two bars are unconnected.

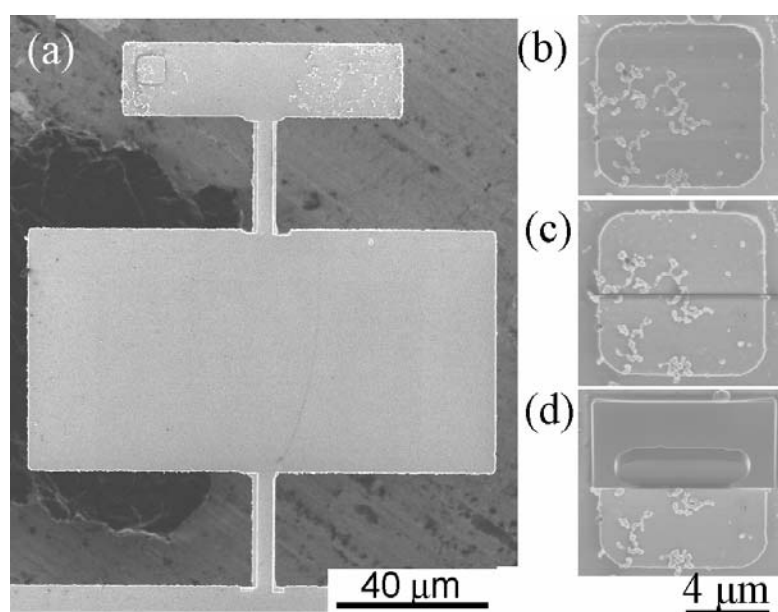


Fig. 5.5 (a) Microcantilever with a $7\ \mu\text{m} \times 7\ \mu\text{m} \times 30\ \text{nm}$ $\text{Ni}_{80}\text{Fe}_{20}$ film deposited on the top left corner. (b) Magnified $7\ \mu\text{m} \times 7\ \mu\text{m} \times 30\ \text{nm}$ $\text{Ni}_{80}\text{Fe}_{20}$ film. (c) Double $7\ \mu\text{m} \times 3.5\ \mu\text{m} \times 30\ \text{nm}$ bars patterned with focused ion beam on the $7\ \mu\text{m} \times 7\ \mu\text{m} \times 30\ \text{nm}$ $\text{Ni}_{80}\text{Fe}_{20}$ film with gap of 50 nm between adjacent bars. (d) Single $7\ \mu\text{m} \times 3.5\ \mu\text{m} \times 30\ \text{nm}$ bar after removing the top bar with focused ion beam.

The magnetic hysteresis loop is obtained by sweeping the external field from - 40 kA/m to + 40 kA/m and back. Fig. 5.6 shows the results in field range of ± 6 kA/m for paired bars (the loop with open circles). The magnetization reversal occurs at -0.75 kA/m and -1.7 kA/m. The first jump at a field of -0.75 kA/m corresponds to the reversal of one of the paired bars. The second jump at a field of -1.7 kA/m corresponds to the reversal of the other one.

After the MTM measurement of the paired bar, the top bar of the same sample was removed with FIB. To make sure that the top bar is completely removed, the depth of the cut is about 500 nm which also removes some of the Si substrate. Fig.5.5 (d) shows only a single $7 \mu\text{m} \times 3.5 \mu\text{m} \times 30 \text{ nm}$ bar is left on the cantilever. Fig. 5.6 shows the results in field range of ± 6 kA/m for the single bar (solid squares). The magnetization reversal occurs around the coercive field of -1.23 kA/m. It is correlated to the domain wall propagating quickly through the bar. The smaller jump in magnetization at - 4 kA/m may be caused by the annihilation of the small domain structure at the edge of the film.

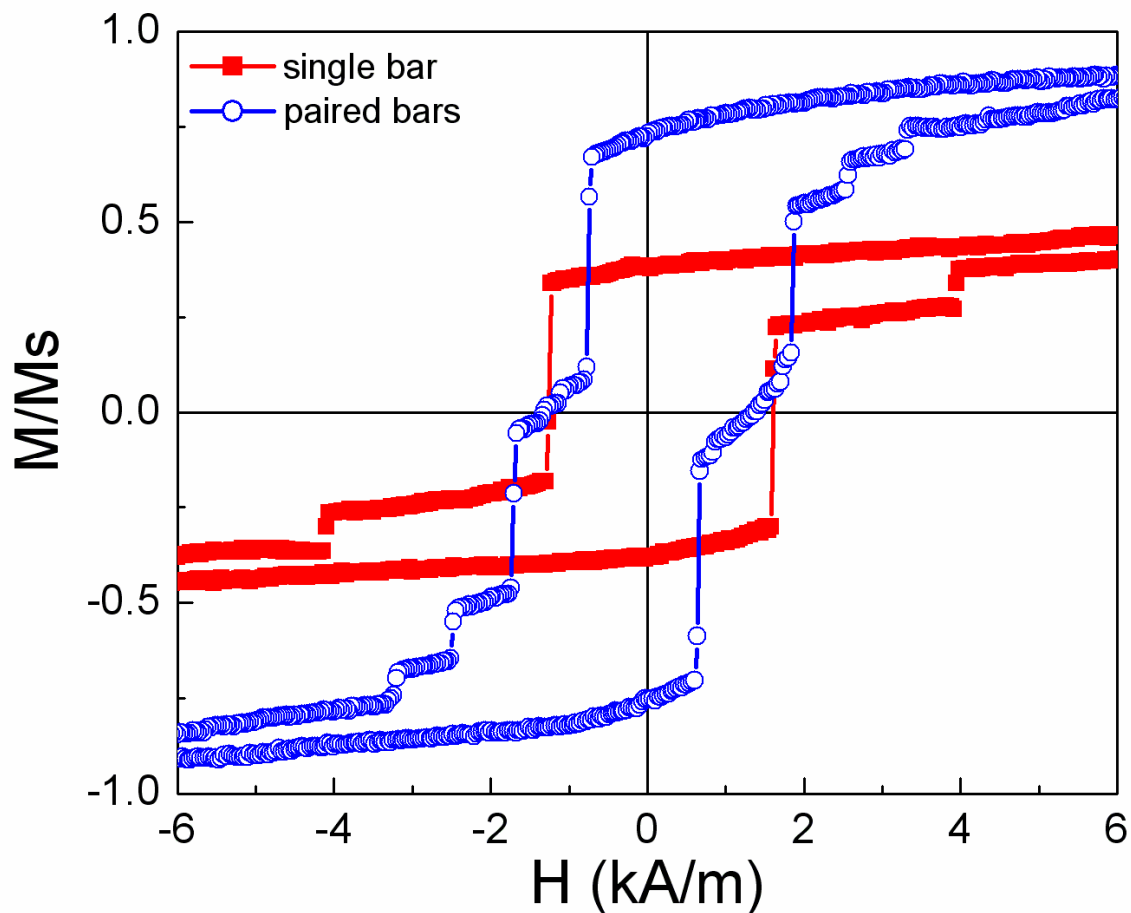


Fig. 5.6 Magnetic hysteresis loops of the single $7 \mu\text{m} \times 3.5 \mu\text{m} \times 30 \text{ nm}$ $\text{Ni}_{80}\text{Fe}_{20}$ bar (solid squares) and same size double bars (open dots) with a gap of 60 nm obtained with a microcantilever torque magnetometer (MTM).

Comparison of the magnetic hysteresis loops of the single and paired bars shows that the switching field of single bars is larger than the reversing field of only one of the paired bars and less than that of both paired bars. This indicates that magnetostatic interaction exists between the closely paired bars.

It has been shown by a micromagnetic simulation that the hysteresis loop for one set of paired $\text{Ni}_{80}\text{Fe}_{20}$ bars ($300 \text{ nm} \times 1.5 \mu\text{m} \times 32 \text{ nm}$) with a gap of 40 nm has two steps

during the reversal [11]. The two steps observed in the hysteresis loop are caused by the magnetostatic interaction between the paired bars. In this study, the size of $\text{Ni}_{80}\text{Fe}_{20}$ bars is much larger than the size of $300 \text{ nm} \times 1.5 \text{ }\mu\text{m} \times 32 \text{ nm}$. The reversal process of larger size bar may involve more domain wall motion than the small size sample.

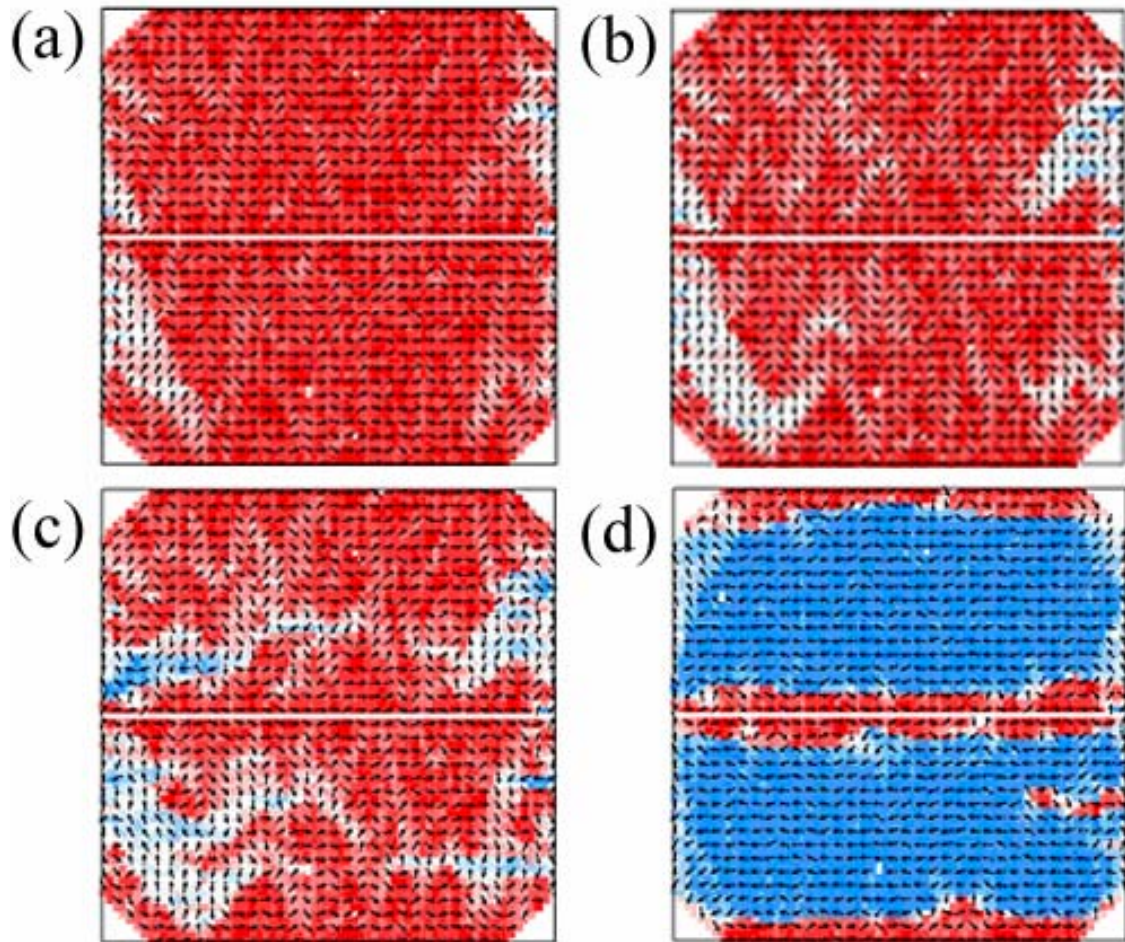


Fig. 5.7 Micromagnetic simulations were performed on the paired $\text{Ni}_{80}\text{Fe}_{20}$ bars ($7 \text{ }\mu\text{m} \times 3.5 \text{ }\mu\text{m} \times 30 \text{ nm}$) with a gap of 50 nm . The sample was saturated along the long axis of the bars and then decreases to (a) -4.77 kA/m ; (b) -20.69 kA/m ; (c) -26.26 kA/m ; (d) -31.83 kA/m .

Micromagnetic simulations were performed by Professor Renat Sabiryanov to study the magnetization reversal of $7 \mu\text{m} \times 7 \mu\text{m} \times 30 \text{ nm}$ $\text{Ni}_{80}\text{Fe}_{20}$ bars using the Landau-Lifshitz-Gilbert solver software package developed by NIST [12]. The distance between the edges of two bars was taken to be 50 nm. The magnetization of $\text{Ni}_{80}\text{Fe}_{20}$ is $8 \times 10^5 \text{ A/m}$, and the exchange stiffness constant is $1.3 \times 10^{-13} \text{ J/m}^3$. The anisotropy of ideal $\text{Ni}_{80}\text{Fe}_{20}$ alloy is extremely small; however the measured film may have a substantial amount of inhomogeneity. Therefore, the following models of anisotropy are considered: (i) no anisotropy $K = 0$, (ii) random anisotropy with $K = 10 \times 10^3 \text{ J/m}^3$, and (iii) random anisotropy with distribution of anisotropy constants between $10 \times 10^3 \text{ J/m}^3$ and $100 \times 10^3 \text{ J/m}^3$. The random anisotropy is chosen to mimic the real thin film medium.

For the single square Permalloy film ($K = 0$, and no defects) with side length of $6 \mu\text{m}$, the simulation results show zero remanent magnetization. The film initially magnetized along one side of the element relaxes to the vortex state at zero field. The reversal starts from the corners by creating vortices and consecutive motion of them. Experimental results show small coercivity with some features in the magnetization reversal curve. In order to introduce the coercivity, anisotropy should be introduced. Uniaxial anisotropy produces a square-like loop.

Non-uniform switching is characteristic of elements with large sizes and containing defects as shown in our experimental results. In order to model these films, we used a random anisotropy model with distribution of uniaxial anisotropies in magnitude, as well as easy axis. At moderate anisotropies there is still strong reduction of remanence magnetization with complex domain structure at zero magnetic fields. A stronger anisotropy constant gives a picture similar to the experiment, i.e. there is large remanent

magnetization and multiple steps in the hysteresis curve caused by pinning. For the paired bars system, the simulation results show that the switching is not independent for the ideal Permalloy film. After saturation, two bars form a symmetrically inversed C-state at the remanent state (no applied magnetic field). With a negative field applied the magnetization reversal proceeds through the formation of two vortices (end domains). Due to the broken symmetry (random anisotropy) the reversal of one of the bar happens first. Although the general picture of the reversal of this bar is similar to a single bar case, there are some deviations because of the interactions with the second bar. Due to the magnetostatic interactions, the system creates a closure for the magnetic field (magnetization of two bars is aligned in opposite directions). It is a metastable state for the system of two bars. Then at somewhat larger applied field the system is forced out of this potential well and the second bar switches as well.

This picture is substantially different if we assume anisotropy random both in magnitude and in direction in the film. The two bars of Permalloy with disorder both in the direction of anisotropy and its magnitude are simulated as shown in Fig. 5.7. The average magnitude of K is taken to be $50 \times 10^3 \text{ J/m}^3$. In this case, the magnetization reversal is quasi-independent for two bars. Both of them form a number of domains with edge domains to be switched the last. Because of the two additional edges (due to the cut) the number of domains near edges is twice the number as in case of one square element. This results in somewhat smaller remanent magnetization. There are multiple steps in the hysteresis loop. In the two-bar case it is more pronounced. It can be probably attributed to the magnetostatic interaction between bars because it forms a domain structure which reduces the stray fields in the free space around the sample. Simulations show that a

large number of domains near the edges of the feature are hard to push out. This energy barrier comes because of the closure of stray fields due to these domains. The formation of these domains is sensitive to the details of the reversal and should be strongly affected by the temperature. As a result, the reversal is not symmetric, especially if complete saturation was not achieved.

The above analysis shows that the reversal of the films in Fig. 5.6 can be understood, if a random anisotropy model with distribution of uniaxial anisotropies in magnitude, as well as easy axis is assumed.

5. 4 The magnetization reversal behavior of two bars with magnetostatic interactions

There are a few methods that reduce magnetic noise and improve reversibility. The key is to have a better control of the magnetic domain structure of the magnetic layer in the magnetic sensors. It has been shown by incorporating a synthetic antiferromagnetic (SAF) structure for a pinned layer reduces stray field from the pinned layer by a factor of >10 and enhances the pinning effect of the pinning layer. The effects of demagnetizing fields within the soft layer can be reduced by thinning the layer itself, and by increasing the distance from the edge of the tunnel junction for a few micrometers. Figure 5.8 shows several different hysteresis loops measured under the same conditions for two $30\ \mu\text{m} \times 15\ \mu\text{m} \times 50\ \text{nm}$ $\text{Ni}_{80}\text{Fe}_{20}$ bars with a gap about $60\ \text{nm}$. When sweeping from an initially large applied magnetic field, the first jump happens at about $0.64\ \text{kA/m}$. The field corresponding to the first jump is different for each loop. As the applied field increases, the second jump happens at about $1.11\ \text{kA/m}$. This field is also different for each measured loop. By comparison the distributions of the first jump and second jump, it is

clearly seen that the thermal magnetic switching distribution is much smaller for the first jump. . That is, the magnetic interactions between paired bars results in a reduced thermal magnetic switching distribution when the first bar reverses its magnetization. This more reversible behavior in the magnetic behavior will allow us to design a better magnetic sensor.

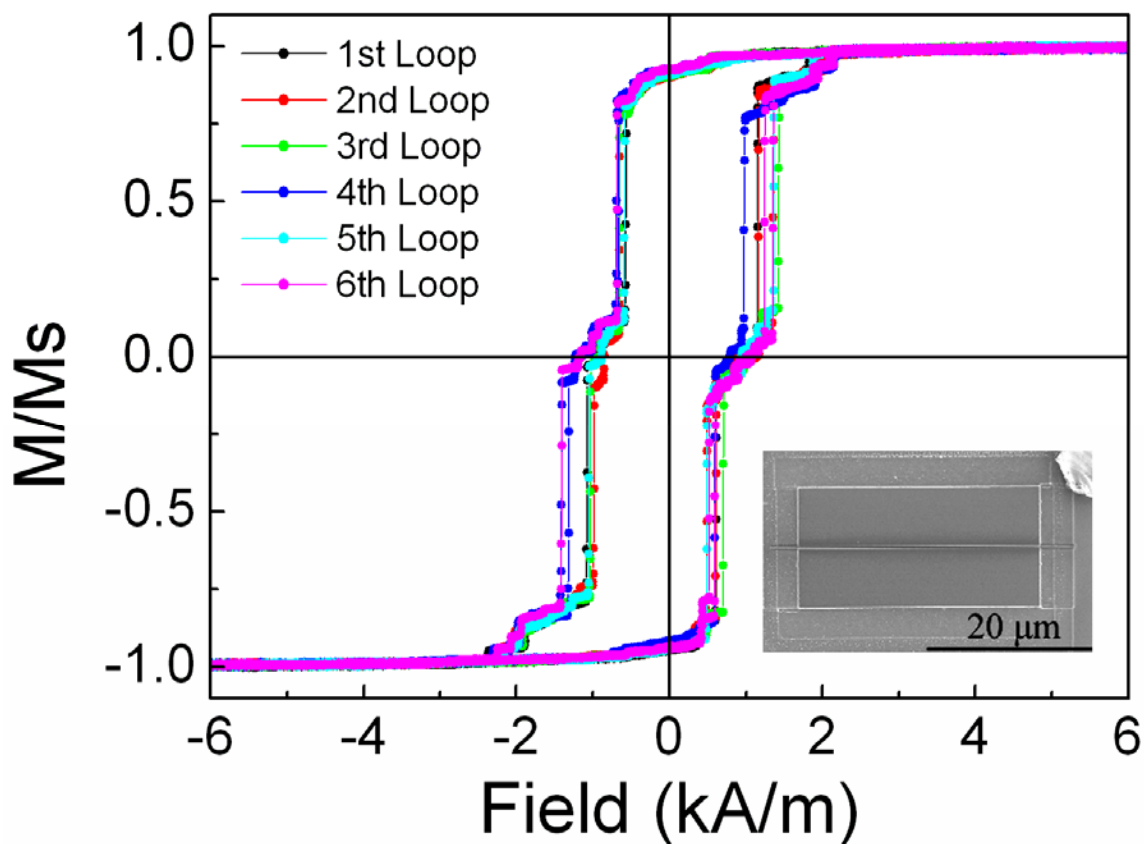


Fig. 5.8 Magnetic interaction in a single paired bars and its magnetic switching behavior shows a reduced thermal magnetic switching distribution when the first bar reverses its magnetization. (The six hysteresis curves are obtained by continuous measurement of the single paired bars using ultra-sensitive microcantilever torque magnetometer.) The inset shows the SEM picture of a microcantilever with single paired bars.

5.5 The magnetization reversal behavior of two bars at various temperatures

We have investigated the magnetic reversal behavior of a pair of bars at various temperatures. Fig. 5.9 shows the hysteresis loop in the field range of ± 10 kA/m a paired bar with dimension of $30 \mu\text{m} \times 10 \mu\text{m} \times 30 \text{nm}$ bars and the gap is 60 nm [inset of Fig. 5.9(a)] measured at 300 K and 5×10^{-7} torr, and 136 K and 1×10^{-6} torr.

When measured at 300K, the magnetization reversal occurs at -1.34 kA/m and -1.79 kA/m. The first jump at a field of -1.34 kA/m corresponds to the reversal of one of the paired bars. The second jump at a field of -1.79 kA/m corresponds to the reversal of the other one. When measured at 136 K, the magnetization reversal occurs at -1.85 kA/m and -2.2 kA/m.

From the comparison of the magnetic hysteresis loops measure at 300 K and 136 K, the field corresponding to the magnetization reversal is larger for the 136 K measurement than the room temperature measurement. Also, the magnetization change between the first jump and second jump at 300K is not as flat as that at 136 K. The domain wall may be pinned by defects in the film. At higher temperature, the thermal energy may push the domain wall through the pinning sites, and shows as a gradually change in magnetization.

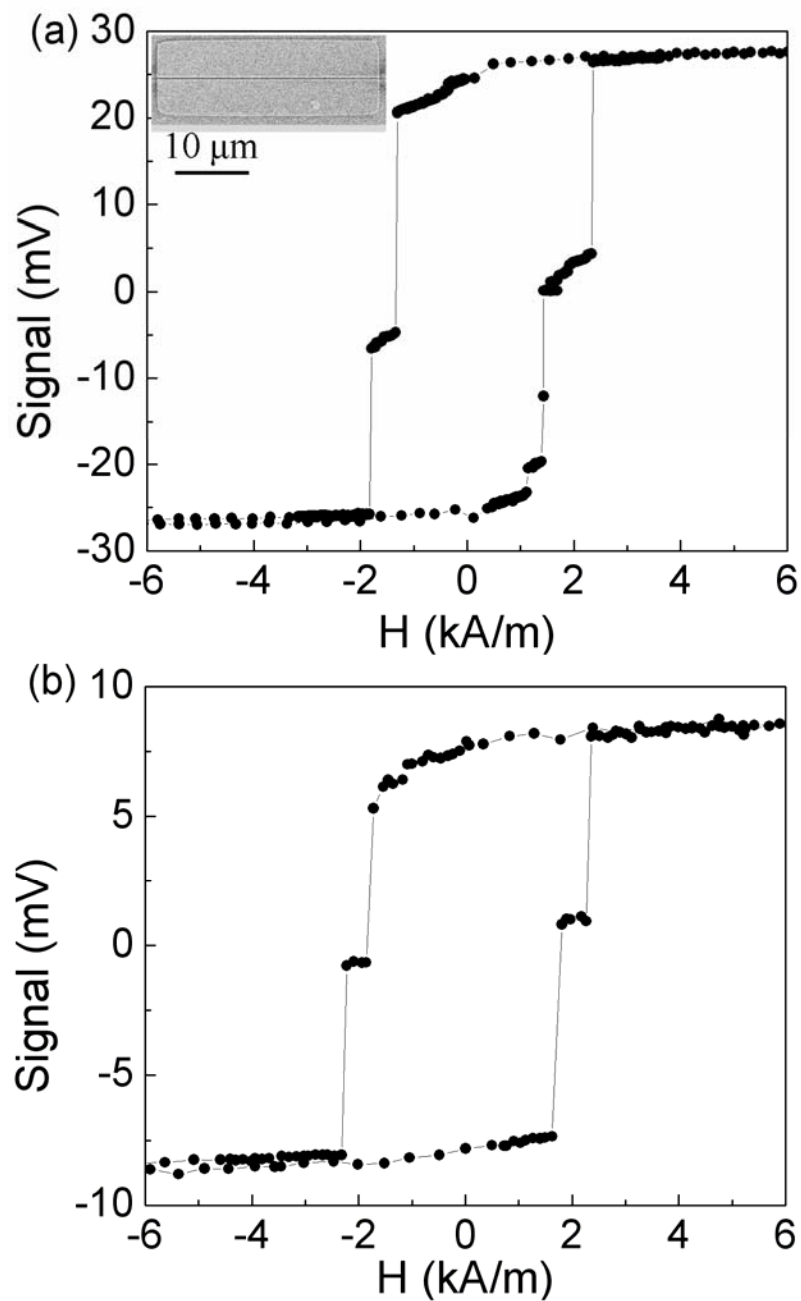


Fig. 5.9 The hysteresis loop of single paired bar with dimension of $30 \mu\text{m} \times 10 \mu\text{m} \times 30 \text{nm}$ and the gap is 60nm [inset of (a)] measured at (a) 300 K and 5×10^{-7} torr and (b) 136 K and 1×10^{-6} torr by MTM.

5.6 Summary

A new process is developed to pattern magnetic films on MTM cantilevers. By using MTM, the magnetic interaction in a single pair of micrometer-sized magnetic samples is studied at various temperatures. The switching field of a single bar is larger than the reversing field of only one of the paired bars and less than that of both paired bars, which indicates that there exists magnetostatic interactions between the closely paired bars. This is correlated to a metastable state where the magnetization directions of the two bars are antiparallel to each other. The experimental results are consistent with micromagnetic simulations, if a random anisotropy model with a distribution of uniaxial anisotropies in magnitude, as well as of the easy axis is assumed. We show that MTM is a highly sensitive method that can be used for the study of magnetic nanostructures with high resolution.

References:

1. D. A. Allwood, G. Xiong, C. C. Faulkner, D. Atkinson, D. Petit, R. P. Cowburn, "Magnetic Domain-Wall Logic," *Science*, **309**, 1688, (2005).
2. Zhi-Pan Li, O. Petracic, J. Eisenmenger, I. K. Schuller, "Reversal behavior of exchange-biased submicron dots," *Appl. Phys. Lett.*, **86**, 72501-1, (2005).
3. V. Novosad, M. Grimsditch, J. Darrouzet, J. Pearson, S. D. Bader, V. Metlushko, K. Guslienko, Y. Otani, H. Shima, and K. Fukamichi, "Shape effect on magnetization reversal in chains of interacting ferromagnetic elements," *Appl. Phys. Lett.*, **82**, 3716, (2003).
4. B. Llic, Y. Yang, and H. G. Craighead, "Virus detection using nanoelectromechanical devices", *Appl. Phys. Lett.*, **85**, 2604 (2004).
5. B. C. Stipe, H. J. Mamin, T. D. Stowe, T. W. Kenny, and D. Rugar, "Magnetic dissipation and fluctuations in individual nanomagnets measured by ultrasensitive cantilever magnetometry," *Phys. Rev. Lett.*, **86**, 2874, (2001).
6. C. Rossel, P. Bauer, D. Zech, J. Hofer, M. Willemin, and H. Keller, "Active microlevers as miniature torque magnetometers", *J. Appl. Phys.*, **79**, 8166, (1996).
7. M. D. Chabot, J. M. Moreland, L. Gao, S. H. Liou and C. W. Miller, "Novel fabrication of micromechanical oscillators with nanoscale sensitivity at room temperature," *Journal of Microelectromechanical Systems*, **14**, 1118, (2005).
8. M. D. Chabot and J. Moreland, "Micrometer-scale magnetometry of thin $\text{Ni}_{80}\text{Fe}_{20}$ films using ultrasensitive microcantilevers," *J. Appl. Phys.*, **93**, 7897, (2003).
9. J. Moreland, "Micromechanical instruments for ferromagnetic measurements," *J. Phys. D: Appl. Phys.*, **36**, R39, (2003).

10. M. Löhndorf, J. Moreland, P. Kabos, and N. Rizzo, "Microcantilever torque magnetometry of thin magnetic films," *J. Appl. Phys.*, **87**, 5995, (2000).
11. M. D. Chabot and J. T. Markert, "Microfabrication of single-crystal silicon multiple torsional oscillators," *Proc. SPIE*, **3875**, 104, (1999).
12. T. R. Albrech, P. Grutter, D. Horne, and D. Rugar, "Frequency modulation detection using high- Q cantilevers for enhanced force microscope sensitivity", *J. Appl. Phys.* **69**, 668 (1991).
13. Jinling Yang, Takahito Ono, and Masayoshi Esashi, "Surface effects and high quality factors in ultrathin single-crystal silicon cantilevers", *Appl. Phys. Lett.*, **77**, 3860 (2000).
14. Dong Hoon Min, "Sub monolayer in-situ magnetometry: magnetic coupling in thin film multilayer system", Ph. D dissertation, Colorado School of Mines (CSM), 2004.
15. Takeshi Fukuma, Masayuki Kimura, Kei Kobayashi, Kazumi Matsushige and Hirofumi Yamada, "Development of low noise cantilever deflection sensor for multienvironment frequency-modulation atomic force microscopy", *Rev. Sci. Instrum.*, **76**, 053704 (2005).
16. M. Liebmann, A. Schwarz, S. M. Langkat, and R. Wiesendanger, "A low-temperature ultrahigh vacuum scanning force microscope with a split-coil magnet", *Rev. Sci. Instrum.*, **73**, 3508 (2002).
17. Takahito Ono, Xinxin Li, Hidetoshi Miyashita, and Masayoshi Esashi, "Mass sensing of adsorbed molecules in sub-picogram sample with ultrathin silicon resonator", *Rev. Sci. Instrum.*, **74**, 1240 (2003).

18. L. Gao, D. Q. Feng, L. Yuan, T. Yokota, R. Sabirianov, S. H. Liou, M. D. Chabot, D. Porpora, and J. Moreland, "A study of magnetic interactions of $\text{Ni}_{80}\text{Fe}_{20}$ arrays using ultrasensitive microcantilever torque magnetometry," *J. Appl. Phys.*, **95**, 7010, (2004).

Chapter 6

Conclusions and the future

In this thesis, the magnetic inhomogeneities in the thin and small magnetic films of magnetic sensors are characterized and studied. The magnetic inhomogeneities are located by using our newly developed sensitivity mapping (MSM) system. The effect of magnetic microstructures in the free layer and the pinned layers of MTJs are studied by the analysis of the temperature and voltage dependence of magnetoresistance of MTJs. An ultra-sensitive microcantilever torque magnetometer (MTM) system is developed to characterize of magnetic nanostructures.

We have presented results of the imaging of the magnetic noise sources at low frequency in both GMR and TMR recording heads. The developed MSM system can locate the magnetic noise sources for the sub-micron sized heads, which is hard to be observed by other methods. The agreement between the image of noise sources and other measurement results is good for the investigated the origin of magnetic noise in recording heads. The field dependent $1/f$ noise and Barkhausen noise may be the main reasons for the noise increase of the unstable recording heads we tested. Future improvements of the system should include reducing the tip end dimension and increasing the tip's magnetic field by using magnetic particles with high magnetic moment, thus increasing the resolution of the image. Better correlation to microstructures should provide more information about the reason to cause the noise increase.

We studied the voltage and temperature dependence of resistance and MR of two types of MTJs. These two types of MTJ samples have different free layer structures but the same pinned structures and the same material for free and reference layers. For type 2 MTJs, a TMR ratio was detected as high as 107% at 13 K. From the analysis of the minor MR loops, we learned that: (1) There are more magnetic inhomogeneous regions in the free magnetic layer and/or at the interface between the free layer and the insulating layer of type 1 MTJ samples than in that of type 2 MTJ samples; (2) There are possible additional spin-glass-like states that occurs at the interface between the free layer and the insulating layer in the type 1 MTJ sample at low temperature. These results clearly indicate that the micro-magnetization orientation in the free layer and the FM/I interface play an important role in determining the TMR ratio in these two types of MTJ samples.

We also investigate the magnetization of the SAF structures on the MR behavior by applying field. It is demonstrated that exchange coupling field are affected by domain structures in the free and pinned layers. The domain may be caused by the inhomogeneity in the interface between AFM/FM layer.

An ultra-sensitive MTM system is developed to characterize the magnetic properties of one or few magnetic structure with single or multi-layer in sub-micron sized in the temperature range from 10 K to 300K and under vacuum up to 1×10^{-8} torr. Sensitivity of the developed variable temperature and vacuum MTM system is improved than that at ambient conditions. We also develop a new process to fabricate the submicron sized single or array patterns on the cantilever for studying their magnetic behavior.

By using MTM, the magnetic interaction in a single pair of micrometer-sized

magnetic samples is studied. The switching field of a single bar is larger than the reversing field of only one of the paired bars and less than that of both paired bars, which indicates that there exists magnetostatic interactions between the closely paired bars. This is correlated to a metastable state where the magnetization direction of the two bars is antiparallel to each other. The experimental results are consistent with micromagnetic simulations, if a random anisotropy model with distribution of uniaxial anisotropies in magnitude, as well as of the easy axis is assumed.

The MTM measurement of single paired bar clearly show that magnetic interactions in a paired bar and its magnetic switching behavior shows a reduced thermal magnetic switching distribution when the first bar reverse its magnetization. This indicates that the magnetic behavior can be better controlled by the magnetic interactions that may allow us to design a better magnetic sensor in the future.

Publication lists:

Patent:

Bernard Doudin, Cheol-Soo Yang, Andrei Sokolov, Sy-Hwang Liou, **Lu Yuan**, "A new type of magnetic memory using chromium oxide junctions", Pattern # 6657888, 12/2/2003.

Invited Talk:

1. **L. Yuan**, S. H. Liou, J. X. Shen, B. B. Pant, "Imaging of magnetic noise sources in recording heads", SPIE Conferences on Fluctuations and Noise in Materials II, Austin, Texas, May 24-25, 2005.
2. Chih-Haung Lai, Sheng-Huang Huang, C. C. Chiang, S. H. Liou, D. J. Sellmyer M. L. Yan, **L. Yuan** and T. Yokata, "Effects of ion-beam irradiation on the $L1_0$ phase transformation and their magnetic properties of FePt and PtMn films" 2005 MRS Fall Meeting at Boston MA, Symposium Q : Degradation Processes in Nanostructured Materials, Nov. 28-Dec. 1, 2005

Publications:

1. A. Baruth, **L. Yuan**, J.D. Burton, K. Janicka, E.Y. Tsymbal, S.H. Liou, S. Adenwalla, "Domain overlap in exchange-coupled [Co/Pt]/NiO/[Co/Pt] multilayers" submitted to Appl. Phys. Lett., (2006)
2. A. Baruth, D.J. Keavney*, J.D. Burton, K. Janicka, E.Y. Tsymbal, S.S. Jaswal, **L. Yuan**, S.H. Liou, S. Adenwalla, "Coupling mechanism in oscillatory coupled [Co/Pt]/NiO/[Co/Pt] multilayers", Phys. Rev. B, (2006).
3. Brett Barwich, Glen Gronniger, **L. Yuan**, Sy-Hwang Liou, and Herman Batelaan, "A measurement of electron-wall interactions using transmission diffraction from nano-fabricated gratings", J. Appl. Phys., (2006).
4. **L. Yuan**, L. Gao, R. Sabirianov, S. H. Liou, M. D. Chabot, D. H. Min, J. Moreland, and Bao Shan Han, "Microcantilever torque magnetometry study of patterned magnetic films", accepted by IEEE Trans. Magn. (2006).
5. **L. Yuan**, S. H. Liou, Dexin Wang, "Temperature dependence of magnetoresistance in magnetic tunnel junctions with different free layer structures", Phys. Rev. B, **73**, 134403 (2006).
6. **L. Yuan**, J. X. Shen, Bharat B. Pant and S. H. Liou, "Imaging magnetic noise sources in magnetic recording heads(invited)", Proceeding of SPIE- Fluctuations and Noise in Materials, **5843**, 1 (2005).
7. T. Yokota, M. Yan, Y. Xu, L. Gao, R. Zhang, L. Nicholl, **L. Yuan**, R. Skomski, D. J. Sellmyer, S. H. Liou, C. Lai, and C. Yang, "Magnetic properties and $L1_0$ phase formation of FePt films prepared by high current-density ion-beam irradiation and rapid-thermal annealing methods", J. Appl. Phys., **97**, 10H306 (2005).
8. **L. Yuan**, J. X. Shen, and Bharat B. Pant, "Locating magnetic noise sources in TMR and GMR recording heads using scanning probe microscopy", IEEE Trans. Magn., **40**, 2233, (2004).

9. L. Gao, D. Q. Feng, **L. Yuan**, T. Yokota, R. Sabirianov, and S. H. Liou, "A study of magnetic interactions of Ni₈₀Fe₂₀ arrays using ultra-sensitive microcantilever torque magnetometry", *J. Appl. Phys.*, **95**, 7010, (2004).
10. L. Gao, **L. Yuan**, L. Nicholl, R. Sabirianov, Z. Y. Liu, S. Adenwalla and S. H. Liou, "Domain structure and magnetoresistance in Ni₈₁Fe₁₉ zigzag wires" *J. Magn. Magn. Mater.* **272-276**, e1301-e1303 (2004).
11. **L. Yuan**, Y. Ovchencov, A. Sokolov, C. -S. Yang, B. Doudin and S. H. Liou, "Magnetotransport properties of CrO₂ films down to single grain sizes", *J. Appl. Phys.* **93**, 6850 (2003).
12. Ruihua Cheng, A.N. Caruso, **L. Yuan**, S. H. Liou, and P.A. Dowben, "Magnetic coupling in Co/Cr₂O₃/CrO₂ "trilayer" films", *Appl. Phys. Lett.*, **82**, 1443 (2003).
13. S. H. Liou, **L. Yuan**, L. Gao, C.D.Chen, S. F. Lee, and Y. D. Yao, "Switching behavior of patterned Ni₈₀Fe₂₀ islands", *Trans. Magn. Soc. Japan*, **3**, 51(2003)
14. Sokolov, C.-S. Yang, **L. Yuan**, S.H. Liou, Ruihua Cheng, B. Xu, C.N. Borca, P.A. Dowben, B.Doudin, " Spin blockade effects in chromium oxide intergrain magnetoresistance", *J. Appl. Phys.* **91**, 8801 (2002).
15. Sokolov, C.-S. Yang, **L. Yuan**, S.H. Liou, R.Cheng, H. -K, Jeong, T. Komesu, B. Xu, C.N. Borca, P.A. Dowben, B.Doudin, " Zero bias anomaly magnetoresistance of CrO₂ junctions", *Europhys. Lett.* **58**, 448 (2002).
16. Ruihua Cheng, C. N. Borca, N. Pilet, Bo Xu, **L. Yuan**, B. Doudin, S. H. Liou, and P. A. Dowben, " Oxidation of metals at the chromium oxide interface", *Appl. Phys. Lett.* **81**, 2109 (2002).
17. Ruihua Cheng, Takashi Komesu, Hae-Kyung Jeong, **L. Yuan**, S. H. Liou, B. Doudin, P. A. Dowben and Ya. B. Losovyj, "Temperature dependent induced spin polarization in Cr₂O₃ overlayers on epitaxial CrO₂ films", *Phys. Lett. A* **302**, 211 (2002).
18. Ruihua Cheng, Z. Y. Liu, Xu Bo, S. Adenwalla, **L. Yuan**, S. H. Liou and P. A. Dowben, " Magnetic anisotropy in epitaxial CrO₂ (100) thin films", *Matt. Lett.* **56**, 295 (2002).
19. Ruihua Cheng, B.Xu, C. N. Borca, A. Sokolov, C.-S. Yang, **L. Yuan**, S. H. Liou, B. Doudin, and P.A. Dowben, "Characterization of the native Cr₂O₃ oxide surface of CrO₂", *Appl. Phys. Lett.* **79**, 3122 (2001).
20. **L. Yuan**, Wen-xia Yang, "The real-time CVSD implementation on one TMS320C31 chip", *Audio Engineering (China)*, **12**, 30 (2000).
21. **L. Yuan**, Wen-xia Yang, "Measurement of sub-circuit's S parameters at microwave frequencies", *Acta Scientiarum Naturalium Universitatis Nankaiensis (China)*, **33**, No. 2, 119 (2000).

Presentation:

1. **L. Yuan**, L. Gao, L. Nicholl, S.H. H. Liou, M. Zheng, E. N. Abarra, B. R. Acharya, G. Choe, and Bao Shan Han, "Magnetic Force Microscopy Study of CoPtCrO Perpendicular Media with Superparamagnetic and Permanent Magnet Tips", Intermag conference, San Diego, May 8-12, 2006.
2. **L. Yuan**, L. Gao, R. Sabirianov, S. H. Liou, M. D. Chabot, D. H. Min, J. Moreland and Bao Shan Han, "Microcantilever Torque Magnetometry Study of Patterned Magnetic Films", Intermag conference, San Diego, May 8-12, 2006.

3. Lan Gao, **L. Yuan**, K. H. P. Kim, S. H. Liou, M. D. Chabot, D. H. Min, and J. Moreland, "A study of the Magnetic Hysteresis of a Single Magnetic Elements using a Sensitive Microcantilever magnetometer" Bull.of American Physical Society, Vol. 50, 1492, 2005.
4. T. Yokota, M. Yan, Y. Xu, L. Gao, R. Zhang, L. Nicholl, **L. Yuan**, R. Skomski, D. J. Sellmyer, S. H. Liou, C. Lai, and C. Yang, "Magnetic Properties and $L1_0$ Phase formation of FePt films prepared by high current-density ion-beam irradiation and rapid-thermal annealing methods", Presented at 49th Annual Conference on Magnetism and Magnetic Materials, Jacksonville, Florida, November 7-11, 2004.
5. **L. Yuan**, J. X. Shen, "Locating Magnetic Noise Sources in TMR and GMR Recording Heads Using Scanning Probe Microscopy", 9th Joint MMM/Intermag Conference, Anaheim, California, 2004.
6. L. Gao, D. Q. Feng, **L. Yuan**, T. Yokota, R. Sabirianov, and S. H. Liou, "A Study of Magnetic Interactions of $Ni_{80}Fe_{20}$ Arrays Using Ultra-sensitive Microcantilever Torque Magnetometry", 9th Joint MMM/Intermag Conference, Anaheim, California, 2004.
7. L. Gao, **L. Yuan**, L. Nicholl, Z. Y. Liu, S. Adenwalla and S. H. Liou, "Domain Structure and Magnetoresistance in $Ni_{81}Fe_{19}$ Zigzag Wires" Bull.of American Physical Society, Vol. 48, 1108 (2003).
8. S. H. Liou, L. Gao, **L. Yuan**, L. Nicholl, Z. Y. Liu, S. Adenwalla and R. Sabiryanov, "Domain Structure and Magnetoresistance in $Ni_{81}Fe_{19}$ Zigzag Wires", ICM '03, Rome.
9. R. Cheng A. N. Caruso, **L. Yuan**, S. H. Liou, P.A. Dowben, "MOKE Studies of Magnetic Coping in $Co/Cr_2O_3/CrO_2$ " Presented at American Vacuum Societies 49th International Symposium , November 3-8, 2002 Denver, Colorado.
10. C. S. Yang, A. Sokolov, **L. Yuan**, S. H. Liou, and B. Doudin; "Chromium Oxide Bistable Memory Device" MRS Fall, 2002
11. **L. Yuan**, Y. Ovchenkov, A. Sokolov, C. -S. Yang, B. Doudin and S. H. Liou; "Magnetotransport Properties of CrO_2 films down to single grain sizes" Presented at 47th Annual Conference on Magnetism and Magnetic Materials, Tampa, Florida, November 11-15, 2002.
12. **L. Yuan**, L. Gao, S. H. Liou, C. D. Chen, S. F. Lee, and Y. D. Yao; "Magnetic Domain Structure in Patterned $Ni_{80}Fe_{20}$ Islands", Bull.of American Physical Society, Vol. 47, 260 (2002).
13. **L. Yuan**, Y. Liu, P. A. Dowben, and S. H. Liou, "TEM study of epitaxial growth of $La_{0.65}Pb_{0.35}MnO_3$ on $LaAlO_3$ and its relation to electronic structure and spin polarization", Microscopy and Microanalysis, Quebec city, Canada, August 2002.
14. A. Sokolov, C. S. Yang, **L. Yuan**, S. H. Liou, Ruihua Cheng, B. Xu, C. N. Borca, P. A. Dowben, and B. Doudin; " Spin Blockade Effects in Chromium Oxide Intergrain Magnetoresistance", Presented at 46th Annual Conference on Magnetism and Magnetic Materials, Seattle, Washington, November 12-16, 2001.
15. R. Cheng, B. Xu, , A. Sokolov, C. Yang, **L. Yuan**, S. H. Liou, B. Doudin, and P. A. Dowben; " Characterization of the Native Cr_2O_3 Oxide Surface of CrO_2 ",

Presented at 46th Annual Conference on Magnetism and Magnetic Materials, Seattle, Washington, November 12-16, 2001.

16. A. Sokolov, C. S. Yang, **L. Yuan**, S. H. Liou, Ruihua Cheng, B. Xu, C. N. Borca, P. A. Dowben, and B. Doudin; “ Spin Blockade Effects in Chromium Oxide Intergrain Magnetoresistance”, Presented at 46th Annual Conference on Magnetism and Magnetic Materials, Seattle, Washington, November 12-16, 2001.